A MEMS-based Microtensile Testing Method for Si Nanowires

by

Berkay Gümüş

A Thesis Submitted to the
Graduate School of Engineering
in Partial Fulfillment of the Requirements for
the Degree of

Master of Science
in
Mechanical Engineering

Koç University

August 2012

Koç University

Graduate School of Sciences and Engineering

This is to certify that I have examined this copy of a master's thesis by

Berkay Gümüş

and have found that it is complete and satisfactory in all respects,
and that any and all revisions required by the final
examining committee have been made.

Committee Members:

B. Erdem Alaca, Ph. D.

Demircan Canadinç, Ph. D.

Arda D. Yalçınkaya , Ph. D.

Date: 29.08.2012

To my dear grandmother

ABSTRACT

As an important building block of various industries, silicon have been gaining more importance day by day. Moreover, as the today's technology is going forward for smaller designs, nano-scale silicon objects such as silicon thin films and silicon nanowires (Si NWs) are of such interest nowadays. Hence for reliable Si-based applications, knowing the materials' behavior is crucial. Although there have been a bunch of experiments in literature on determination of the mechanical properties of Si NWs, they are all based on nanomanipulated samples, which are first fabricated, then gripped on their ends before tensile loading. In addition to gripping, there are also challenges in creation of nN forces and detection of nm displacements for accurate mechanical tests. These critical issues require different methodologies using devices designed for micro-scale mechanical tests. The micro electromechanical systems (MEMS)-based devices are suitable for micro-nano integration, *i.e.* testing platform-sample.

This work consists of two parts: MEMS design alongwith fabrication and Si NW fabrication. The strategy involves the fabrication and characterization of MEMS design for later NW integration and the optimization of Si NW fabrication. As the first objective, the design of a unique MEMS-based tensile testing method, which is specialized for Si NWs, was completed. The uniqueness of the designed device is stemming from its ability to test Si NWs without any grips. This is because the NW is fabricated at the same time with the device through an monolithic top-down method. This method enables the elimination of the interface effects between the nanowire and the device. The device is composed of a comb-drive actuator to apply uniaxial force on Si NW and a triplate differential capacitive force/displacement sensor to detect the force applied and the elongation of Si NW. The finite element analyses of the devices were carried out using COMSOL Multiphysics. After the comparison of the analytical and simulation results for certain designs, the first batch microfabrication of the MEMS part was realized through various SOI micromachining processes in Center of Micro and Nanotechnology (CMi) at EPFL with a CD of 2 μm. The critical dimension is the minimum linewidth in the design. These processes includes defining the structrues and, preparing the devices for characterization. The electrical characterization of the fabricated devices were conducted using semiconductor parameter analyzer. The capacitance characteristics of the devices under an applied voltage of 5 V were determined. The values for the changes in the total capacitances were in the order of femtofarads(fF). The results were also compared with finite element simulations. The comparison shows the small effect of measurement

environment on the change in total capacitance of the devices. Other than this effect, the experimental results show promising consistency with the simulations. These concludes the verification of the MEMS design.

As the second objective of this thesis, a process route was proposed and a few trials have been carried out for the fabrication of Si NWs. The route includes the definition of NW with e-beam lithography. The formation of the NW is realized with a two-step etching process which includes two subsequent Bosch processes with different scallop dimensions. The first step forms the Si NW and the second step etches around 1 μm Si layer under the NW. After the NW is protected with envelope-like structure, Si device layer is etched through buried oxide (BOX) layer. The moment of this flow is to protect NW after formation within an envelope-like structure for the latter steps of microfabrication. This envelope-like structure will be alumina and formed using atomic layer deposition technique. The Si NW was well-formed after etching steps. The formation of alumina envelope remains as a matter of future work. A fabrication process flow is proposed in this thesis which can be used for the formation of single Si NW.

ÖZET

Çeşitli endüstri kollarının önemli bir yapı taşı olmasından ötürü silisyum, her geçen gün daha büyük önem kazanmaktadır. Buna ek olarak, günün teknolojisinin daha küçük tasarımları hedef almasından dolayı, son zamanlarda silisyum ince filmler ve ya silisyum nanoteller (Si NT) gibi nano-ölçekli silisyum nesneler daha büyük ilgi çekmektedirler. Güvenilir Si temelli uygulamalar için malzeme özelliklerinin bilinmesi gereklidir. Literatürde silisyumun mekanik özelliklerini belirlemeye yönelik bir çok deney bulunmasına karşın, bunlar tümüyle öncelikle üretilip daha sonar uçlarından tutturulan, nano ölçekte müdahale edilmiş numuneler üzerinde yapılmıştır. Tutturmaya ek olarak, nN mertebesinde kuvveterin oluşturulması ve nm mertebesinde yer değiştirmelerin saptanması konularında da zorluklarla karşılaşılmaktadır. Bu kritik hususlar mikro-ölçek mekanik testler için değişik cihazların kullanılacağı farklı yöntemler gerektirmektedir. Mikro elektromekanik sistem temelli cihazlar mikro-nano (*test platformu-numune*) birleşimi, için uygun bir seçenek oluşturmaktadırlar.

İşbu çalışma MEMS tasarımı ve üretimi ile birlikte Si NT üretiminden oluşmaktadır. Uygulanan strateji, MEMS tasarımının sonradan NT ile birleşimi için üretimi ve karakterize edilmesi ile Si NT üretiminin optimize edilmesini içermektedir. İlk amaç olarak, Si NT'ler için özelleştirilmiş, benzersiz bir MEMS temelli germe cihazının tasarımı tamamlanmıştır. Bu cihazın benzersizliği, Si NT'ler üzerinde tutturmaya gerek duymaksızın germe testi yapabilecek olmasından kaynaklanmaktadır. Bunun sebebi Si NT'in cihaz ile aynı anda, yekpare bir *yukarıdan aşağıya* yöntemle üretilecek olmasıdır. Bu yöntem ile cihaz ve tel arasında oluşacak arayüzlerin etkileri yok edilmiş olacaktır. Cihaz, Si NT üzerine tek eksenli kuvvet uygulayacak bir elektrostatik tarak tahrik mekanizması ve Si NT üzerine uygulanan kuvveti ve telin uzamasını ölçecek bir üçlü plakalı diferansiyel sığa sensöründen oluşmaktadır. Cihazların sonlu eleman analizleri COMSOL Multipyhsics kullanılarak yapılmıştır. Analitik sonuçlar ile benzetim sonuçlarının karşılaştırılmasından sonra, bazı tasarımlar için ilk yığın MEMS kısımlarının mikroüretim çalışmaları çeşitli *SOI* mikroişleme yöntemleri vasıtasıyla İsviçre Federal Teknoloji Enstitüsü (EPFL) Mikro ve Nanoteknoloji Merkezi'nde (CMi), 2 μm kritik boyut ile gerçekleştirilmiştir. Bu yöntemler cihazların belirlenmesini ve karakterizasyon sürecine hazırlanmasını içermektedir. Cihazların elektriksel karakterizasyonu *yarıiletken parametre çözümleyici* kullanılarak yürütülmüştür. 5 V'a kadar uygulanan potansiyel fark

altında, cihazların sığa belirginlikleri saptanmıştır. Toplam sığa değişim değerleri femtofarad mertebesindedir. Bu sonuçlar ayrıca sonlu eleman benzetimleri ile de karşılaştırılmıştır. Bu karşılaştırma, ölçüm ortamının cihazların toplam sığası üzerindeki küçük etkisini göstermiştir. Bu etkinin haricinde deneysel sonuçlar benzetimler ile umut verici bir tutarlılık göstermektedir. Bu, MEMS tasarımının doğrulamasını sonuçlandırmaktadır.

İşbu tez çalışmasının ikinci amacı olarak, Si NT'lerin üretimi için bir süreç hattı önerilmiş ve bir kaç deneme yapılmıştır. Bu hat NT'lerin *e-ışın litografi* ile belirlenmesini içermektedir. NT'in oluşması, arka arkaya uygulanan ve farklı *elma ısırığı* ölçülerine sahip Bosch yöntemlerini içeren iki adımlı bir aşındırma süreciyle gerçekletirilecektir. İlk adım Si NT'in oluşmasunı sağlarken ikinci adım NT'in altından 1 μm Si katman aşındıracaktır. NT'in zarf benzeri yapı ile korunmasının ardından *Si cihaz katmanı*, *oksit katmanına* kadar aşındırılacaktır. Bu akışın önemi NT'in oluşturulduktan sonra zarf benzeri bir yapı ile sonraki mikroüretim adımlarında korunmasıdır. Bu zarf benzeri yapı alumina olup atomsal katman bırakım yöntemi ile oluşturulacaktır. Si NT, aşındırma adımları sonrası başarıyla oluşturulmuştur. Alumina zarfin oluşturulması gelecek çalışma konusu olarak kalmıştır. Bu tez çalışmasında tek bir Si NT üretiminde kullanılabilecek bir üretim akışı önerilmiştir.

ACKNOWLEDGEMENTS

I would like to thank Dr. Erdem Alaca for welcoming me to work in this very delightful group and for his guidance throughout all these two years. Alongside these, I am grateful to him for giving me the chance of being at Koç University and the opportunity to work at one of the largest facilities in MEMS research, CMi-EPFL. I would like to thank Dr. Arda D. Yalcinkaya and to BETA Lab. members at Boğaziçi University for all their help and time during chacaterization of the devices. I would also like to thank Prof. Yusuf Leblebici for his generous invitation to LSM-EPFL. I am deeply thankful to Dr. Demircan Canadinc for not just being in my committee but also for his heartfelt advices and understanding.

I am indebted to Davide Sacchetto for all his assistance through cleanroom processes and helpful discussions throughout my stay in EPFL.

I would like to thank CMi staff: Cyrille Hibert, Joffrey Pernollet, Boris Lunardi, Zdenek Benes, Georges-Andre Racine for all their patient supervision and collegiality during microfabrication.

I am and I will be thankful eternally to my family for their support on me and my decisions all the time. Not different from them, I am grateful to my dear Nazik for all her assistance and contribution to my life.

Lastly, I owe a lot to my friends İsmail Yorulmaz, Evren F. Arkan, Zuhal Taşdemir, Gökhan Nadar, Yasin Kılınç, S. Mine Toker, Orkun Önal, Ayşen Sarıoğlu, M. Akif Yalçınkaya, Barış Çağlar, Bekir Yenilmez, Talha Akyol, Mustafa R. Haboğlu, R. Burak Erarslan for being with and helping me during hard times.

This thesis was supported in part by TÜBA-GEBİP and Koç University-İstanbul Rotary Club Fundamental Research Seed Fund Program.

TABLE OF CONTENTS

LIST OF TABLES

LIST OF FIGURES

Chapter 1

INTRODUCTION

Nano-scale materials are gaining more importance day by day due to their different material properties than their bulk counterparts. Silicon, as the raw material of electronics industry, has different material properties at nano-scale. These differences are mainly caused by the surface effects dominating below a critical size. The surface effect alters some of the mechanical, thermal, electrical properties of silicon. This critical size has been reported as 30 nm for mechanical properties by Zhu *et. al.* [1]. Bending strength of Si ,for example, can be even about 23-28 times higher for nano-scale structures than milli-scale structures [2]. Thermal conductivity, on the other hand, can be 20 times lower for nano-scale than that of micro-scale [3]. In addition, electrical resistivity is lower for the Si nanowire than that of original Si wafer and it decreases with decreasing wire diameter [4]. Interconnected with these different electrical properties, nano-scale silicon structures have another promising property called giant piezoresistance which is the very high change in electrical resistivity under applied mechanical stress. The piezoresistance of the nano-scale components can be up to 40 times of the bulk Si ones [5]. On the contrary, Milne *et. al.* claimed that this giant piezoresistivity is caused by the charge trapping and detrapping characteristics of Si nanowires and microwires [6]. Hence, the material properties of a nano-scale material have to be investigated in detail prior to any reliable application.

At macro- and micro-scale, a set of mechanical testing platforms are used, for example tensile test, bending test and fatigue test. Although the basic principles and analytical expressions may be used at the nano-scale, testing devices and strategies must be different. This is because the nano-scale material is difficult to handle and it is difficult to detect displacements and forces at nm and nN scales, respectively.

The microelectromechanical systems (MEMS) may be the best choice for mechanical testing of the nano-scale materials due to their smaller sizes that are suitable for in-situ mechanical testing in high resolution microscopes such as atomic force microscope (AFM), scanning electron microscope (SEM) and transmission electron microscope

(TEM). The high optical resolution of SEM and TEM can measure the nano-scale displacements with continuous imaging of the specimen.

In this work, a novel MEMS device is proposed. It is designed specifically for tensile testing of silicon nanowires. The uniqueness of the design comes from the idea of eliminating interfaces between the sample and the MEMS with the help of a monolithic process flow. The contribution of this thesis is the realization of design and modeling and the first generation microfabrication of the proposed microtensile device.

Microfabrication of various device designs was carried out and they were characterized. The ultimate result of this project will be the determination of mechanical properties of silicon nanowire samples of different volumes ranging from 10^4 to 10^9 nm^3 more accuretly than the previous works without the effect of interfaces and grips. Moreover, within this range, down to about 10^6 nm^3, strength of silicon nanowires increases steadily with decreasing volume reaching an ultimate strength of 17.53 GPa [2]. However, the data below 10^6 nm^3 limit is scattered due to inconsistencies in measurement technology. Ultimate goal is to define this transition through 10^6 nm^3 line.

In Chapter 2, literature review on both mechanical testing of nano-scale silicon samples and micro-tensile testing of nano-scale materials will be given.

In Chapter 3, analytical modeling and finite element analyses of the proposed device using MATLAB and COMSOL Multiphysics, respectively, will be discussed in detail.

In Chapter 4, microfabrication effort of the designed devices carried out in cleanroom facilities of Center of Micro and Nanotechnology (CMi) at Swiss Federal Institute of Technology Lausanne (EPFL) will be discussed. The process consists of various micromachining techniques which will be discussed in detail alongwith the results as SEM images.

In Chapter 5, electrical characterization of the fabricated devices including the determination of voltage-capacitance characteristics will be discussed and compared with COMSOL results.

A vision of this work along with future work will be drawn in Chapter 6.

Chapter 2

MECHANICAL TESTING AT SMALL SCALE

2.1 Overview

In literature there are mainly two different mechanical testing methods for nano-scale materials: bending test and tensile test. For bending tests generally an AFM probe is used to apply a load on the specimen that is clamped on at least one of its ends. On the other hand, similar to a macro-scale tensile test machine, a MEMS tensile testing platform has an actuator mechanism that mainly exerts a tensile force on the specimen and a sensor that reads the applied force on the specimen and/or displacement of it. In this chapter, previous work on both of these two types of mechanical tests will be shown. Then, examples of tensile testing, will be discussed in detail.

2.2 Nano-scale Mechanical Tests

Mechanical tests on nano-scale samples, *i.e.* nanowires (NWs), nanotubes (NTs), nanorods (NRs), nanofibers (NFs) etc., can be listed under two major groups, bending and tensile tests. For the bending tests of nano-scale materials, first the specimen to be tested is fabricated either through top-down or bottom-up approaches and clamped at least on one of its ends and simply bent with an applied force by a sharp tip which is generally an AFM cantilever as illustrated in Figure 2.1. Sample studies on bending tests of nano-scale materials are listed in Table 2.1.

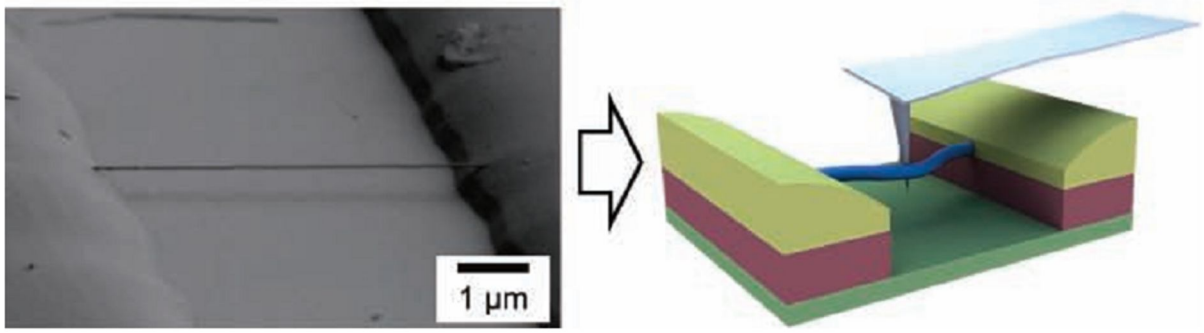

Figure 2.1: Nano-scale bending test using an AFM tip [7]

Material	Results Reported (E:Young's Modulus, σ_y: yield strength, σ_f: fracture strength, N/M:not mentioned)	Reference
Si NW	E=100-275 GPa, σ_y=3-10 GPa	[7]
Si NW	E=assumed as bulk Si, σ_f=~12GPa	[8]
Amorphous SiO_2 NW	E=76.6±7.2 GPa, σ=N/M	[9]
ZnO NW	E=29±8 GPa, σ=N/M	[10]
ZnO nanobelt	E=38.2±1.8 GPa, σ=N/M	[11]
ZnO NW	E=97±18 GPa(tensile), σ_f=6-9 GPa	[12]
ZnO NW	E=~40 GPa, σ=N/M	[13]
ZnS nanobridge	E=52±7 GPa, σ=N/M	[14]
GaN NW	E=33-62 GPa, σ=N/M	[15]
$TiSi_2$ NW	$E_{average}$=194.5 GPa, σ_f=~9 GPa	[16]
Ni NW	E=262±29 GPa, σ_f=3.88±0.9 GPa	[17]

Table 2.1: Sample bending tests at nano-scale

There are issues related to bending tests which make them less reliable than tensile tests [18, 19]:

(1) The displacements are higher in bending tests which make the detection of deformation easier. On the other hand, force required to create same stress levels on the specimen is much smaller for bending tests which calls for higher force resolution values for force detection.

(2) Bending tests are more sensitive to any changes in geometry or alignment of the specimen.

(3) Bending tests are more complicated due to large-deformation-behavior and stress concentration phenomenon at the loading point. Hence, complete modeling of the bending tests is required for reliable characterization.

The second testing method, microtensile testing, is similar to conventional tensile testing by which the specimen is stretched along its longitudinal axis and the elongation is measured. A microtensile testing device, on the other hand, is simply composed of three main parts, an actuator, the sample to be tested, and the force/displacement sensor. There are different types of actuation and detection mechanisms used in MEMS-based devices [20]. The actuation and detection mechanisms of tensile testing machines are given in Table 2.2 with reported results of the corresponding works.

Material	Actuator/ Sensor	Specimen Attachment	Results Reported (E:Young's Modulus, σ_y: yield strength, σ_f: fracture strength, N/M:not mentioned)	Reference
Si NW	Electrostatic/ Capacitive	In situ SEM nanomanipulation	E=170±2.4 GPa, σ_f=5.4 GPa	[21]
Single Crystal Si Nanobeam	Electrostatic/Clamped Beam	Cofabricated with the device	E=161-167 GPa, σ=N/M	[22, 23]
Poly-Si Thin Film	Thermal/ Capacitive	Cofabricated with the device	E=156±17 GPa, σ_f=1417±3 MPa	[24]
Poly-Si Thin Film	Electrostatic/ Capacitive	Cofabricated with the device	E=154.5±12.5 GPa, σ_f=1.42±0.02 GPa	[25]
Co NW	Electrostatic/Clamped Beam	Nanomanipulation and nanosoldering with FEBID/FIBID	E=75.3±14.6 GPa, σ_f=1.6±0.4 GPa	[26]
Polyacrylonitrile NF	Capacitive/ Optical	Nanomanipulation	E=~0.5-6 GPa, σ_f=~50-350 MPa	[27]
C NW	Electrostatic/ Cantilever	FIB-CVD	E=42.6-80.7 GPa, σ_f=4.3 GPa	[28]
MWCNT	Electrostatic/ Capacitive	CVD on Si wafer	E=315±11 GPa, σ_f=12-20 GPa	[25]
Ni nanobeam	Thermal/ Capacitive	Pt clamping	E=208 GPa, σ_f=2.3±0.2 GPa	[29]
GaN NW	Thermal/ Optical	C-Pt clamping	E=N/M, σ_f=4.0±1.7 to 7.5±3.4 GPa	[30]

Table 2.2: Sample tensile tests at nano-scale

In thermal actuation, v-shaped structural beams are subjected to heating which drives the testing machine due to thermal expansion of these beams as illustrated in Figure 2.2 on the left [25]. The main problem with thermal actuators is that during actuation, *i.e.* heating of the beams, the specimen to be tested is also heated which may alter the mechanical properties of the material.

The other major actuation mechanism relies on generated electrostatic forces. There are two designs for electrostatic actuation, parallel plate actuators and comb drive actuators. An example of electrostatic comb drive actuator is given in Figure 2.3 on the left [25]. A comb drive actuator is composed of two set of fingers that are fixed on an anchor interdigitated with one set of fingers that are connected to a moving shuttle. The tensile

force is generated by electrostatic interaction caused by electrical potential difference between fixed and movable fingers and the shuttle moves as it pulls the sample.

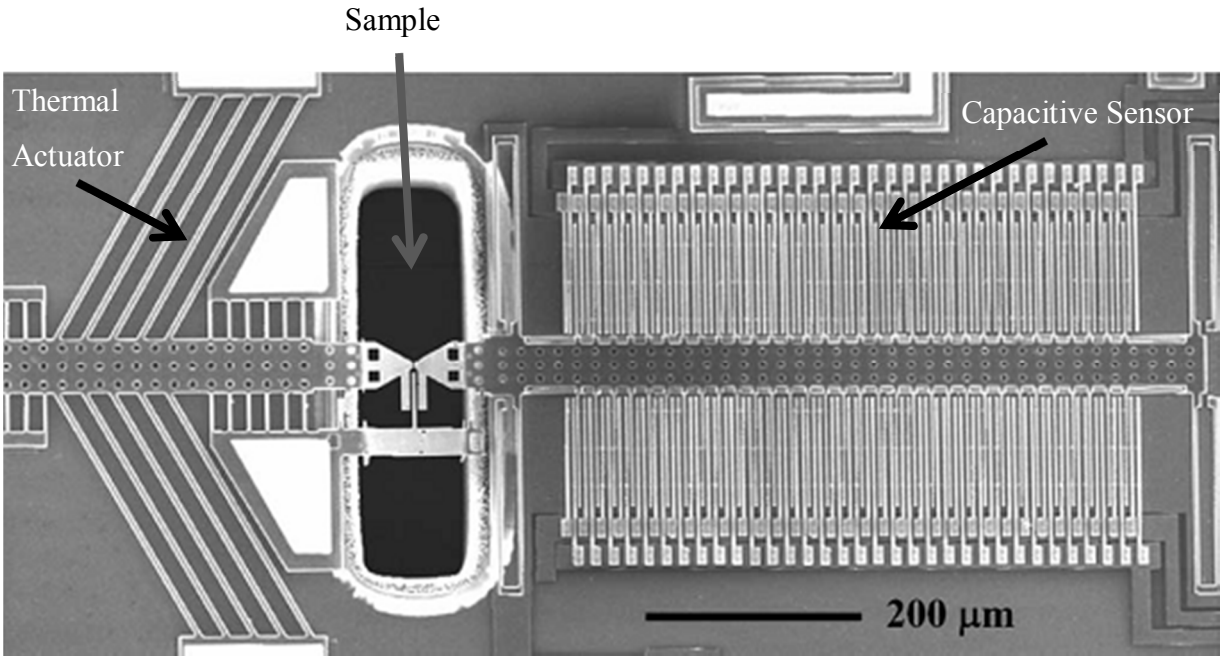

Figure 2.2: A tensile testing machine with thermal actuator [25]

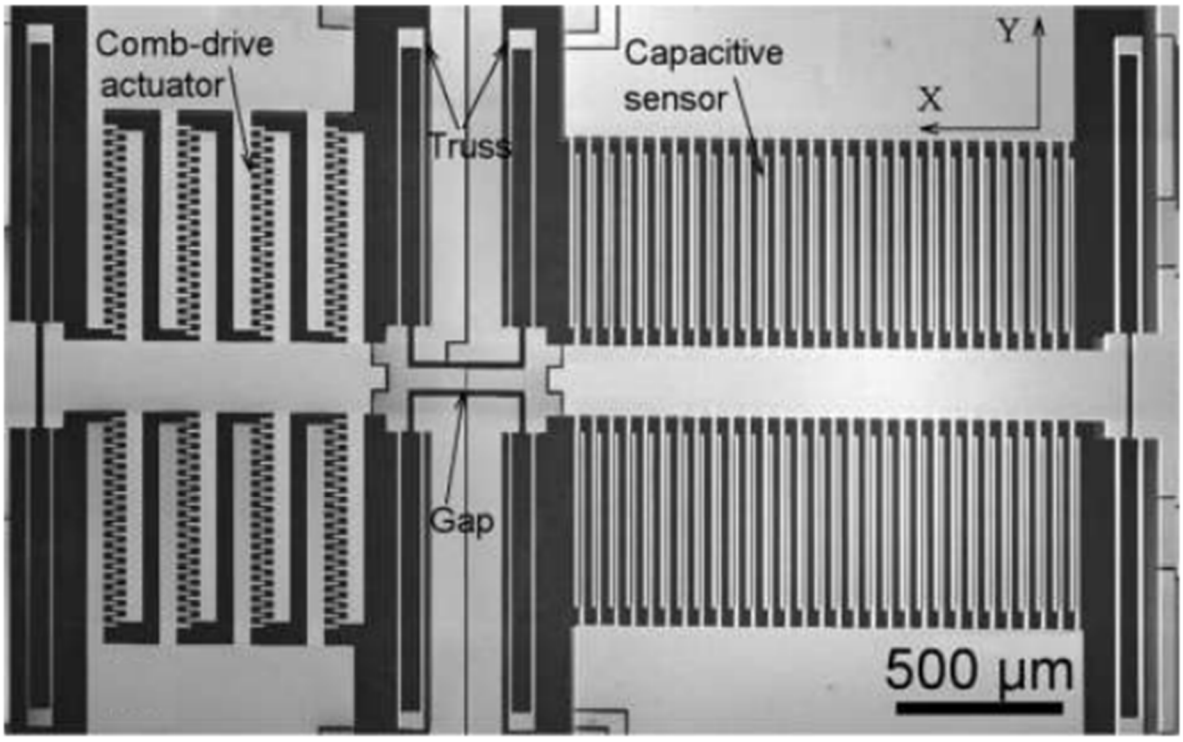

Figure 2.3: A tensile testing machine with electrostatic comb drive actuator [25]

The different types of actuators in MEMS technology are compared in Figure 2.4 [20]. The bubble chart is showing the maximum displacement and maximum force ranges of various actuators. The comb drive actuators have comparibly high force and displacement ranges among micro-scale actuators. The thermal actuators are indicated as solid expansion on the chart and they have higher force values than comb drive actuators for the same displacement values. However, as stated before, thermal actuators are not reliable as the sample is heated at the same time with expansion beams.

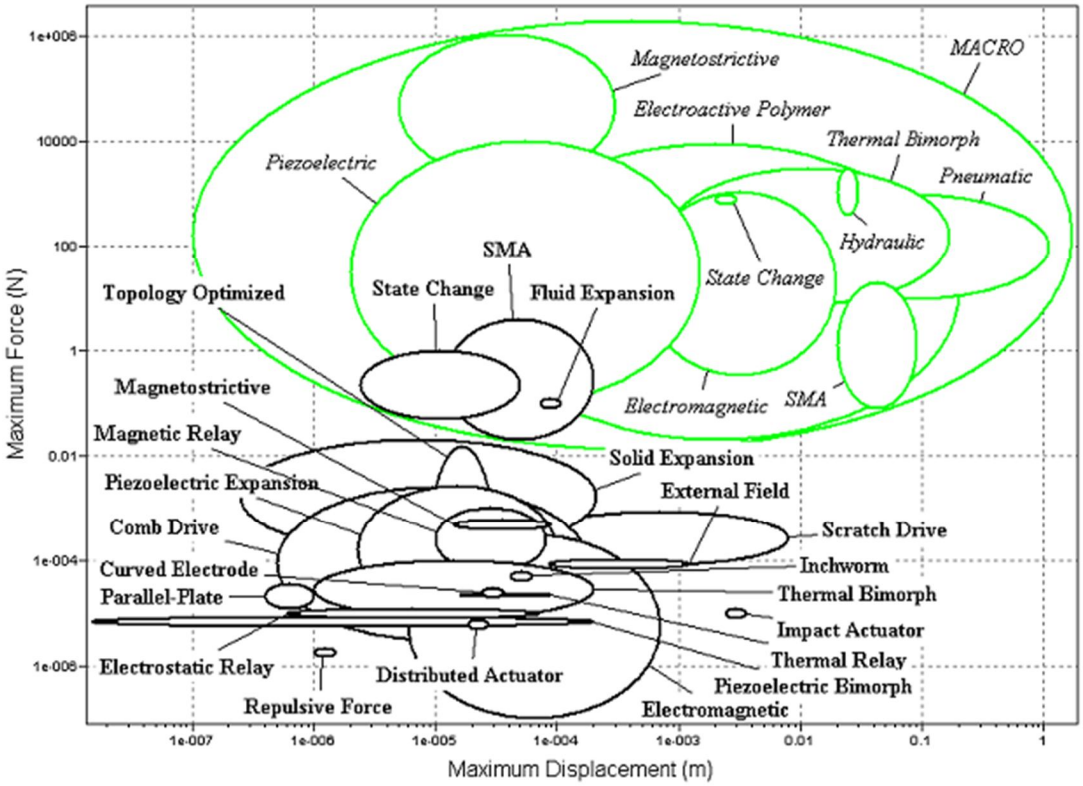

Figure 2.4: The comparison of MEMS and macro actuators [20]

In this work, comb drive electrostatic actuators are selected since they,

(1) are less dependent on fabrication processes, since the actuation is not due to structural aspects, *i.e.* thermal expansion of beams, as it is for thermal actuators,

(2) enable large displacement ranges (up to 100 μm),

(3) do not require heating,

(4) make generation of highly in-plane forces easier [19].

The other part of the tensile testing systems is a sensor that basically reads the force/displacement on/of the sample under test. The methods for the readout of a general microtensile testing can be optical or capacitive.

In optical detection, displacement of the sample is amplified by mechanical means using clamped beams or cantilever as illustrated in Figure 2.5(a) and 2.5(b), respectively [26, 28]. In 2.5(a), the position of the horizontal beam with respect to other two vertical beams is detected under SEM which is an indication of specimen elongation. On the other hand, in 2.5(b), the elongation of the specimen, δ, is amplified with the indicated cantilever in the measurement part and converted to the deflection of the cantilever, δ_{amp}. Then, this amplified displacement is detected by charge coupled device (CCD) camera or SEM.

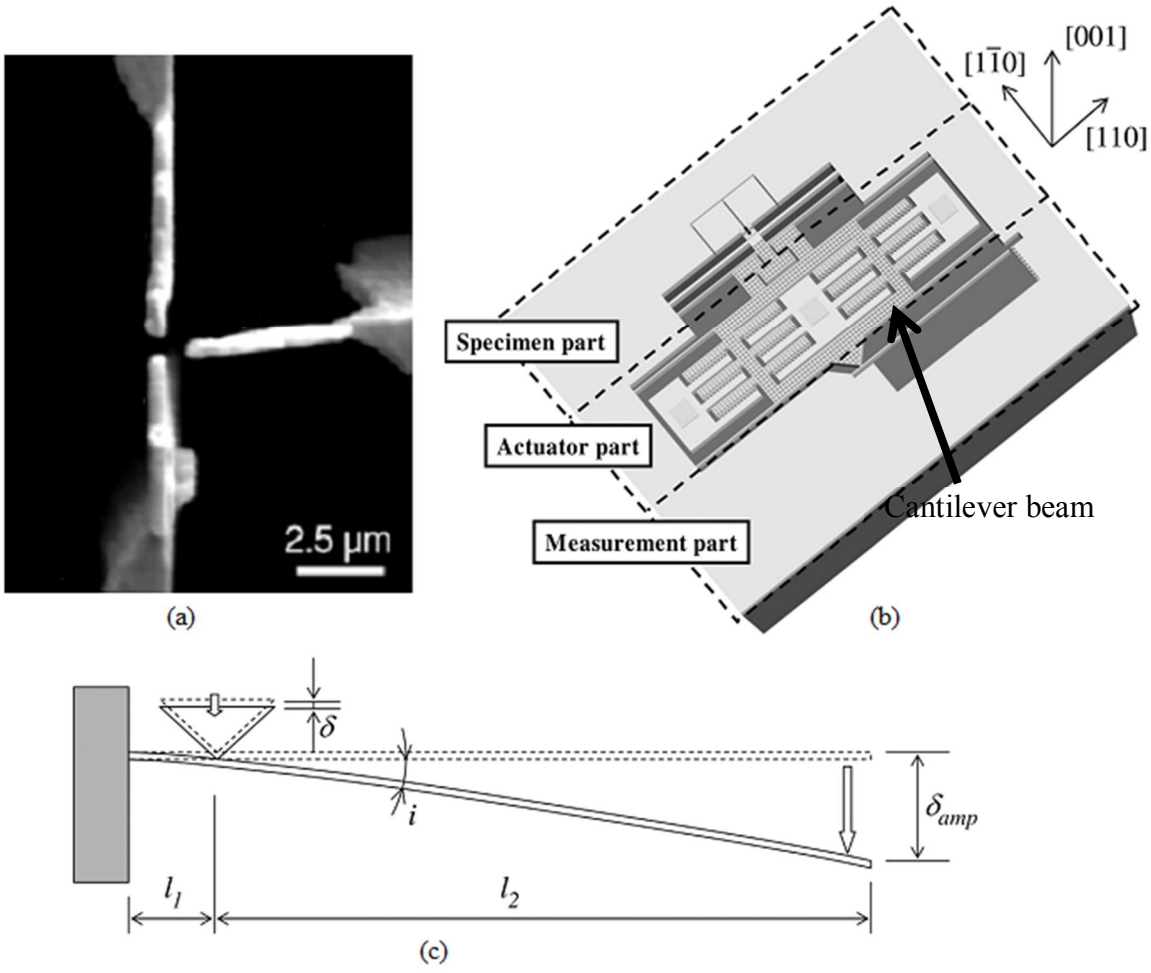

Figure 2.5: Optical detection of sample elongation by (a) clamped beams [26] and (b) free-end cantilevers and (c) the amplification of elongation with cantilevers [28]

The detection mechanism used in this work is based on capacitive detection of the motion of interdigitated fingers of the sensor as illustrated in Figure 2.6. Examples of a capacitive sensor are seen on the right in Figure 2.2 and Figure 2.3. The choice of capacitive sensing is based on the low power, low noise, high sensitivity nature of it [31]. A simple capacitive sensor consists of two sets of fingers fixed on an anchor and one set of

fingers placed on a moving shuttle. As the specimen is pulled by the actuator, x_A, and elongated during the test, ΔU_s, the shuttle of the force/displacement sensor moves as well, x_{FS}, which creates a capacitive change. This capacitive change is converted into the displacement of the fingers, hence with the known stiffness of the sensor, converted into the force exerted on the specimen.

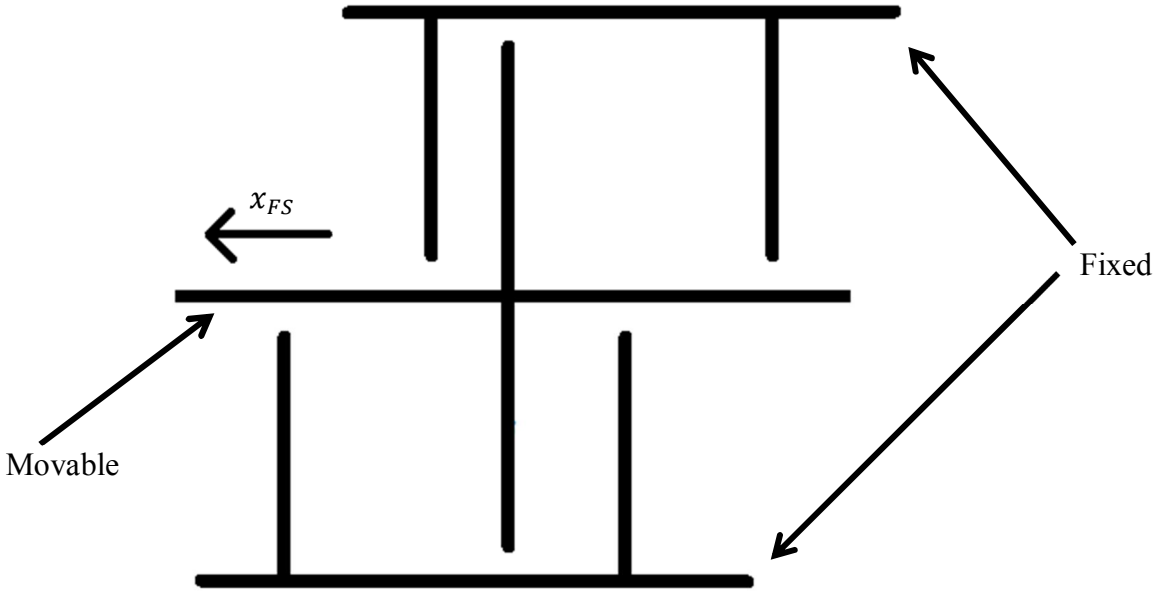

Figure 2.6: The mechanism of a tri-plate capacitive sensor

Different types of MEMS and macro force/displacement sensors are compared in Figure 2.7 [20]. The bubble chart is showing the maximum force ranges and the force detection resolution values of various types of macro- and micro-scale sensors. Among all micro-scale force sensors, capacitive force sensors are the ones which can measure higher forces with comparibly higher resolutions.

There are some issues to be considered related to tensile tests at the nano-scale as discussed by Bell *et. al.* [20] as listed below.

(1) Integration of the sample with the testing device.

(2) Creation of small forces and detection of small displacements at nN and nm scales, respectively.

(3) The effect of friction and machine compliance.

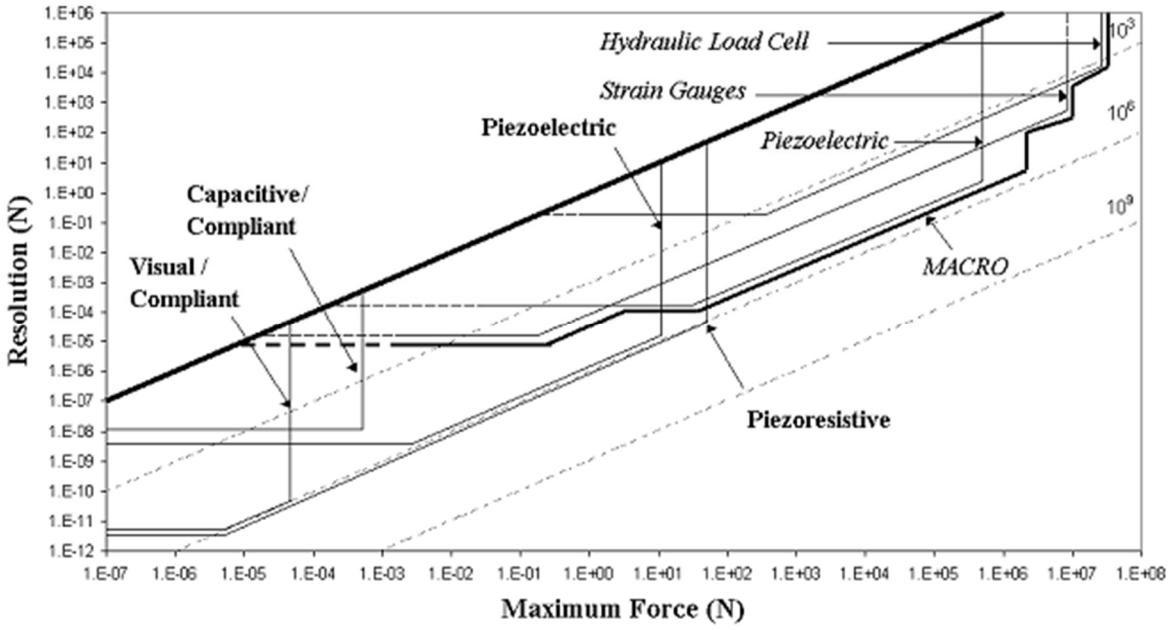

Figure 2.7: The comparison of MEMS and macro sensors

The first problem is the integration of the sample with the testing device. In previous works, sample to be tested was synthesized or fabricated individually and then placed in the sample gap of the design with the help of nanomanipulators or probes. However, this post-integration comes with its problems such as interfaces between the testing device and the sample or misalignment of the sample. The misalignment of the sample may cause the deviation of the force from unaxiality which is assumed for all calculations. This problem is to be solved by this work since the Si NW sample is designed to be fabricated on the same chip with the device. By this design superiority, no interfaces will be formed between the NW and the device. By the help of lithography NW will be aligned exactly on the same axis with the generated force.

The second issue is the creation and detection of the nano-scale forces and displacements which is possible by the utilization of comb drive electrostatic actuators and capacitive sensors [20].

The last problem is the effect of friction and machine compliance which is caused by the reaction forces, R, within testing system as illustrated in Figure 2.8 where the initial length of sample is l_s. This reaction force creates a displacement, Δl_M, in addition to the sample elongation, ΔU_s, since the actuator and the force sensor can be considered as springs. This compliance effect can be neglected during calculations since the stiffness of the testing device is much larger than the specimen's. Moreover, as there is no interface between the sample and the device, there will not be a friction effect during stretching.

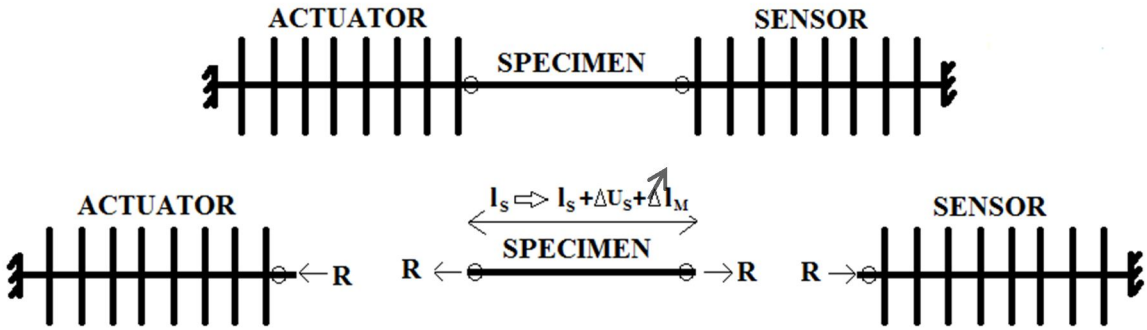

Figure 2.8: The effect of machine compliance

In addition to the microtensile device, there is another design conducted within this work, a pre-stress indicator. This indicator is designed to measure the pre-stress in Si NW before mechanical testing which may be caused by various microfabrication processes. There are several methods proposed in literature to measure the fabrication-induced stress in micromachined structures [32-34]. Among these, microstrain gauge used by Ericson *et. al.* was selected as shown in Figure 2.9. However, in this work, the structures are thicker than the work done by Ericson *et. al*. Hence, it requires further modeling with respect to this altered moment of inertia.

According to this pre-stress indicator design, due to initial compressive or tensile strain the test beam in Figure 2.9 is rather extended or shorten, respectively. This change in the length of the test beam is converted to the rotation of the indicator beam by the help of the slope beam by the equations listed in Table 2.3. The deflection of the indicator beam in radians is defined as θ_{ib} while the deflection in µm is defined as x_{ib}. The elongation and pre-stress in the test beam is defined as x_{tb} and σ_{tb}, respectively and E is the elastic modulus of Si. Please see Table 3.3 for the definition of other geometric parameters. At the end, the pre-strain within the wafer is measured by the movement of vernier gauge fingers.

$$\sin\theta_{ib} = \frac{x_{ib}}{l_{ib}}$$

$$x_{tb} = \frac{2\,\theta_{ib}\,l_{sb}}{3\,C},$$

$$\text{where } C = \left(\frac{1}{d^2} - \frac{1}{d^3}\right),$$

$$\text{where } d = \frac{w_{ib}}{l_{sb}}$$

$$\sigma_{tb} = E\,\frac{x_{tb}}{L_{tb}}$$

Table 2.3: Equations related to pre-stress indicator

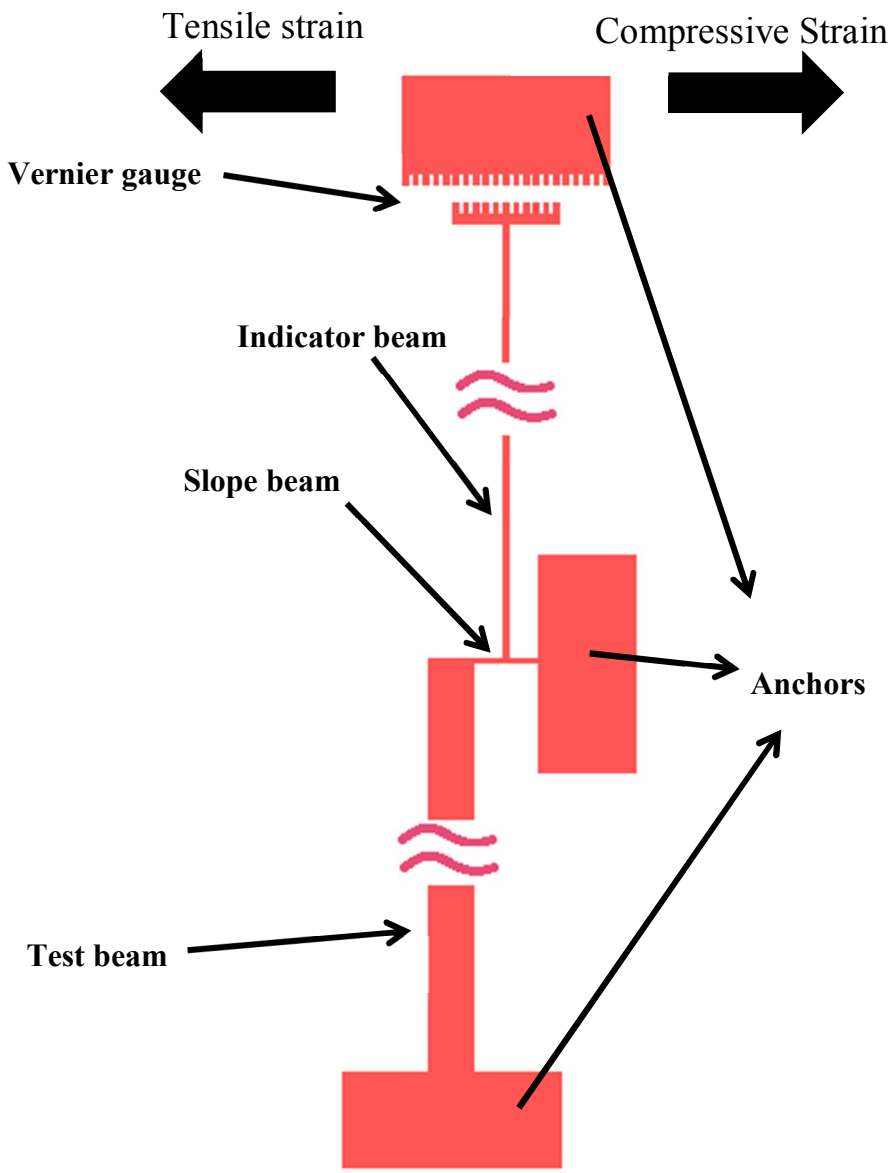

Figure 2.9: The pre-stress indicator inspired for this work [32]

Chapter 3

MEMS MODELING

3.1 Overview

In this chapter, the parameters and criteria for the design of microtensile testing device will be explained. Analytical modeling effort and finite element analysis of the system will be given in detail. At the end, a comparison will be made between analytical design and simulation results. In addition to the testing device, pre-stress indicator modeling will be discussed at the end of the chapter.

3.2 Design Parameters and Mechanical Model

Main parameters for the design of the microtensile testing device are the geometric dimensions of the fingers of both the comb drive actuator and capacitive force sensor. These include the gaps between fingers (g_y, g_x, d_1, d_2), the overlapping distances (h, l_{FS}) and the widths of the fingers (w_A, w_{FS}), the lengths ($l_{kA1}, l_{kA2}, l_{kFS1}, l_{kFS2}$) and the widths ($w_{kA}, w_{kFS}$) of the structural beam springs and, the thickness (t_A, t_{FS}) of the device. The other parameters related to design of the device are the electrical parameters including the driving voltage of the actuator (V_A) and the driving voltage of the force sensor for capacitive readout (V_{FS}). These geometric parameters are shown in Figure 3.1 and tabulated in Table 3.1.

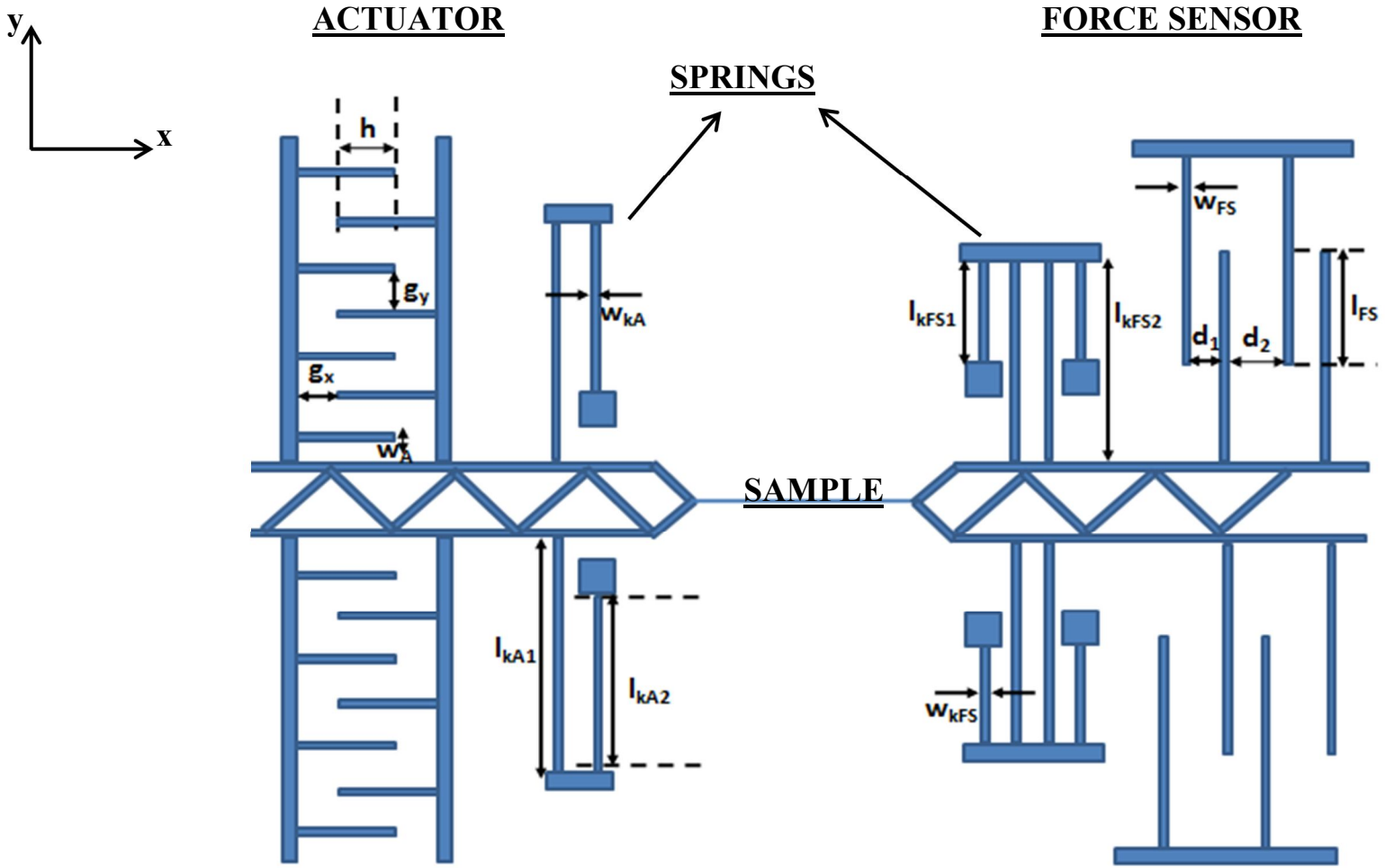

Figure 3.1: A schematic representation of all geometric parameters of the microtensile testing device

Design parameter	**Notation**	**Design parameter**	**Notation**
Width of the actuator finger	w_A	Width of the force sensor finger	w_{FS}
Gap between the two actuator fingers	g_y	Smaller gap between the two force sensor fingers	d_1
Gap between the two actuator finger sets	g_x	Larger gap between the two force sensor fingers	d_2
Overlap distance between the two actuator finger sets	h	Overlap distance between the two force sensor fingers	l_{FS}
Width of the actuator springs	w_{kA}	Width of the force sensor springs	w_{kFS}
Lenghts of the actuator springs	l_{kA1}, l_{kA2}	Lengths of the force sensor springs	l_{kFS1}, l_{kFS2}
Number of the actuator fingers	N_A	Number of the force sensor fingers	N_{FS}
Applied driving voltage to the actuator	V_A	Applied driving voltage to the force sensor	V_{FS}
Thickness of the actuator	t_A	Thickness of the force sensor	t_{FS}

Table 3.1: Design parameters with corresponding notation

The mechanical model of the testing system is given in Figure 3.2. The Si NW and the force sensor are in series and they are parallel to the actuator as they are modeled by individual springs, K_S, K_{FS}, K_A, respectively. With respect to this model, the electrostatic force generated by the actuator, F_e, is separated into two parts: the actuator and the Si NW. The elongation of the Si NW, ΔU_S can be calculated using the displacements of the actuator, x_A, and the force sensor, x_{FS}. Moreover, the force on Si NW, F_S, is the same as the force on the force sensor, F_{FS}.

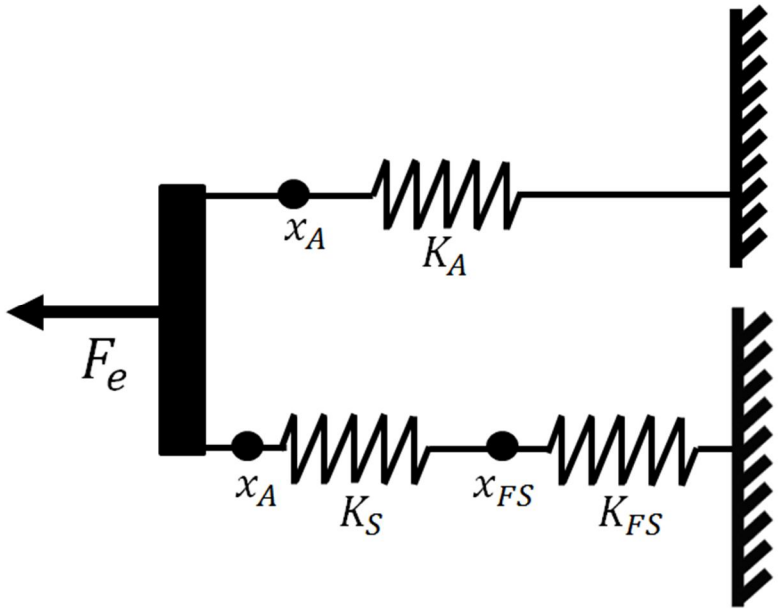

Figure 3.2: Mechanical model of tensile testing system

$\Delta U_S = x_A - x_{FS}$	$\Longrightarrow$	$\varepsilon_s = \Delta U_S / l_S$
$F_{FS} = F_S = x_{FS} K_{FS}$		where ε_S and l_S are the strain and the initial length of the NW, respectively.

Table 3.2: The equations related to mechanical model

3.3 Working Principle of Microtensile Device

The actuation of the microtensile device relies on the generated electrostatic force due to the applied voltage between the interdigitated fixed and movable finger sets. As the voltage increases, force generated increases and the actuator pulls the specimen. The force generated by the electrostatic actuator, F_e, is calculated as in equation 3.1. For the definition of related parameters please see Table 3.1.

$$F_e = N_A \varepsilon_0 V_A^2 \left(\frac{t_A}{g_y}\right) \quad 3.1$$

The force sensor, on the other hand, is based on the change in capacitance between fixed and movable finger sets. This change is caused by the movement of the fingers as the specimen elongates. The triplate geometry is used to increase the voltage output by the applied AC drive voltage with 180° phase difference. The change in total capacitance, ΔC, is calculated as in equation 3.2 with the assumption of $x_{FS} \ll d_1^2 \ll d_2^2$ [21], where A_{FS} is the overlapping area between force sensor fingers. For the definition of related parameters please see Table 3.1

$$\Delta C = 2N_{FS}\varepsilon_0 A_{FS}\left(\frac{1}{d_1^2 - x_{FS}^2} - \frac{1}{d_2^2 - x_{FS}^2}\right)x_{FS} \approx 2N_{FS}\varepsilon_0 \frac{A_{FS}}{d_1^2} x_{FS} \quad 3.2$$

The output voltage, V_{out}, due to this capacitance change, C_{total}, is calculated as in equation 3.3. Since the geometry of the force sensor is symmetric and hence it has differential capacitance nature, the total capacitance is not changed during the operation. ΔC_{max} is equal to ΔC where x_{FS} is maximum, *i.e.* at the end of experiment.

$$V_{out} = \frac{\Delta C_{max}}{C_{total}} V_{FS} \quad 3.3$$

3.4 Design Criteria

Parameters given in the previous part are chosen with respect to four major design criteria: stability, linearity, simplicity of the device and limitations related to microfabrication. The algorithm followed for the design of microtensile device is illustrated in Figure 3.3.

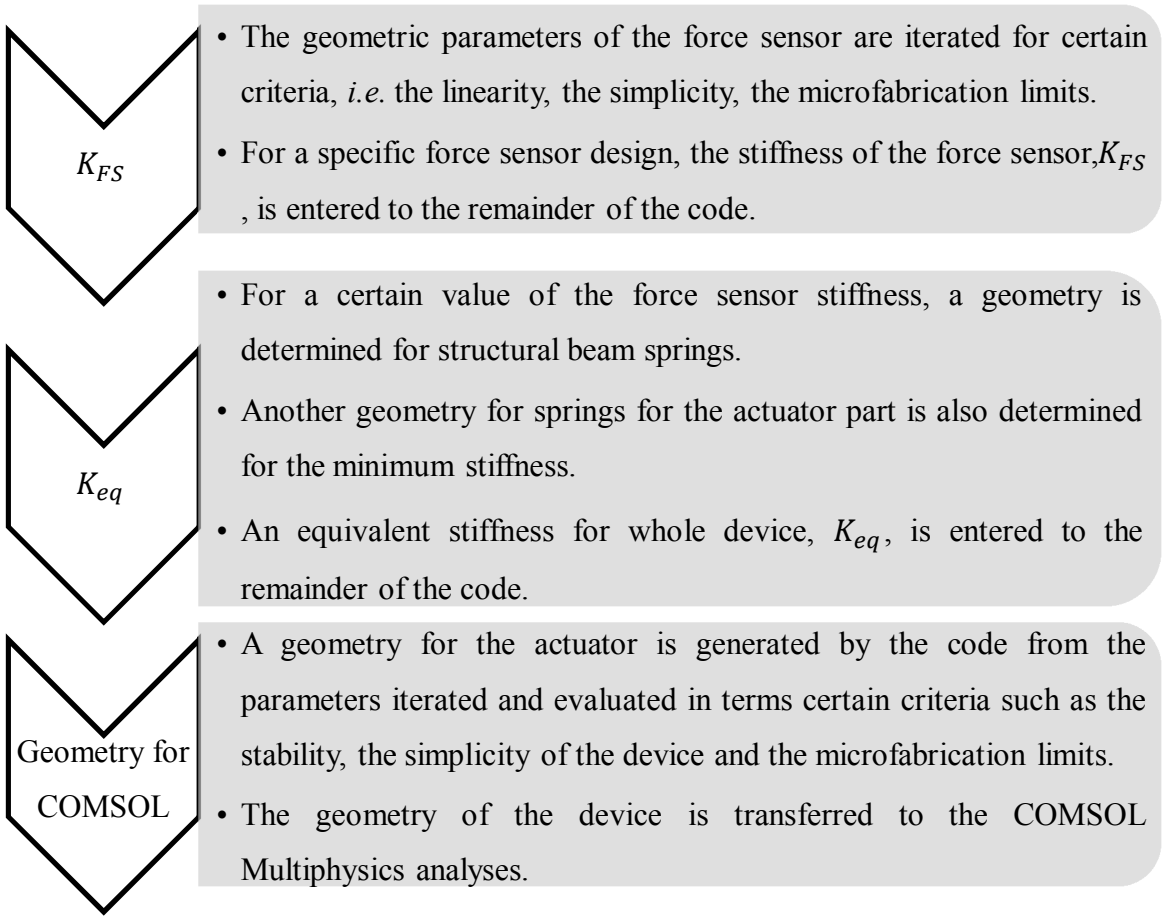

Figure 3.3: The algorithm of microtensile device design

3.4.1 Stability of the Device

The stability of the device is mostly related to the driving voltage that is applied to the actuator and the sensor. This driving voltage causes an electrostatic force which alters the displacement of the movable fingers. This force may affect the measurement sensitivity, and even the whole operation itself. This parasitic electrostatic force creates a parasitic capacitance that makes the real capacitance difference difficult to read. On the other hand, if this parasitic force becomes higher than the restoring force of the suspensions, the pull-in phenomenon occurs. For the actuator part, due to applied potential difference across the fixed and movable fingers, the movable fingers may stick to the fixed sets of fingers which terminates the operation. For the sensor part, larger driving voltages may also cause pull-in. Therefore, due to pull-in, there will be no capacitance that can be read from the sensor. The pull-in effect can be discussed further as the side pull-in and the front pull-in.

The *side pull-in* is one form of the pull-in effect which is the sticking of the side of the movable electrode to the fixed electrode. Since the movable electrode between two fixed electrodes is in an unstable position, a small displacement after some critical value on the y-direction for the actuator or on the x-direction for the force sensor may cause the sticking of the electrode. For the definition of coordinates please see Figure 3.1 For the actuator, there is not any motion along the y-direction. Hence, side pull-in effect cannot be seen unless there are instabilities coming from microfabrication processes. However, since the electrostatic force, which should be smaller than the restoring force of the actuator springs in order to avoid side pull-in, is getting larger as the movable fingers are moving into the fixed fingers, *i.e.* overlapping area increases, the side pull-in may occur easily. Thus, the side pull-in voltage, V_{PI}^{y}, is calculated as in equation 3.4 where ε_0 is the permittivity of free space. Please see Table 3.1 for related parameters.

$$V_{PI}^{y} = \left[\frac{K_A^y g_y^3}{2\varepsilon_0 N_A t_{kA}(x_A^{max} + h)}\right]^{1/2} \qquad 3.4$$

where, K_A^y is the stiffness of the actuator springs on y-direction and x_A^{max} is the maximum displacement of the actuator during the tensile test.

On the other hand, for the force sensor, the side pull-in effect is to be examined carefully since its motion is along x-direction. A critical spring constant in x-direction for the force sensor part where sticking occurs, k_{cr}, can be calculated as [35],

$$k_{cr} = \frac{\partial F_x}{\partial x}|_{x=0} = \frac{2N_{FS}\varepsilon_0 t_{FS} l_{FS} V_{FS}^2}{d_1^3} \qquad 3.5$$

where,

$$F_x = \frac{N_{FS}\varepsilon_0 t_{FS} l_{FS} V_{FS}^2}{2}\left[\frac{1}{(d_1 - x_{FS})^2} - \frac{1}{(d_1 + x_{FS})^2}\right] \qquad 3.6$$

and x_{FS} is the displacement of the force sensor along x-direction. The previous parametric study by Arkan [36] shows that the critical distance which the force sensor shuttle move safely is not larger than the half of the smaller gap, d_1. Therefore, whole sensor designs have been made for maximum shuttle movement of $d_1/2$.

As the name implies, in the *front pull-in* effect, front surface of the movable fingers of the actuator stick to the surface of the fixed electrodes. For the sensor part, the front pull-in effect can be neglected since the stiffness of the force sensor in y-direction is very high that it is unlikely to see front pull-in. However, for the actuator part, since the stiffness of the actuator is kept as low as possible and there is parallel-plate capacitor effects between the front surfaces of the actuator fingers and the fixed electrode fingers, the front pull-in effect should be analyzed in depth. The electrostatic force generated on N_A number of parallel-plate capacitors, F_p, can be calculated as in equation 3.7. [35].

$$F_p = \frac{N_A \varepsilon_0 t_A w_A V_A^2}{(g_x - x_A)^2} \tag{3.7}$$

where x_A is the displacement of the actuator along the x-direction. In order to avoid front pull-in, the restoring force of the springs, F_{res}, must compensate the electrostatic forces both due to actuation, F_e, and parallel-plate effect, F_p.

$$F_{res} = F_e + F_p \tag{3.8}$$

Hence, the relation below must be satisfied;

$$\frac{\partial F_{res}}{\partial x} \geq \frac{\partial F_p}{\partial x} \tag{3.9}$$

At the end, a critical distance for the stable operation of the comb drive actuator, x_{cr}, is calculated from the relation given.

Another concept that should be considered for the stability of the testing system is the *levitation* phenomenon [37]. The levitation of the device is the movement of the fingers perpendicular to the ground plane that is caused by the electric field between the device and handle layers of the silicon on insulator (SOI) wafer. This unwanted electric field is created due to applied voltage to the fixed fingers which may result in an out-of-plane motion of the shuttle. However, the previous models [38] show that this motion is negligible, as shown in Figure 3.4, when the travelling range and the gap are small. The gap here is equal to the thickness of buried oxide (BOX) layer of the SOI wafers, which

creates the gap between the fingers and the ground plane. Although this levitation is negligible, in order for further elimination of this unwanted motion of the shuttle, spring design is optimized such that they have symmetrical locations around the device that limits this out-of-plane motion. Moreover, the spring stiffnesses along z-direction are much higher than those along moving directions.

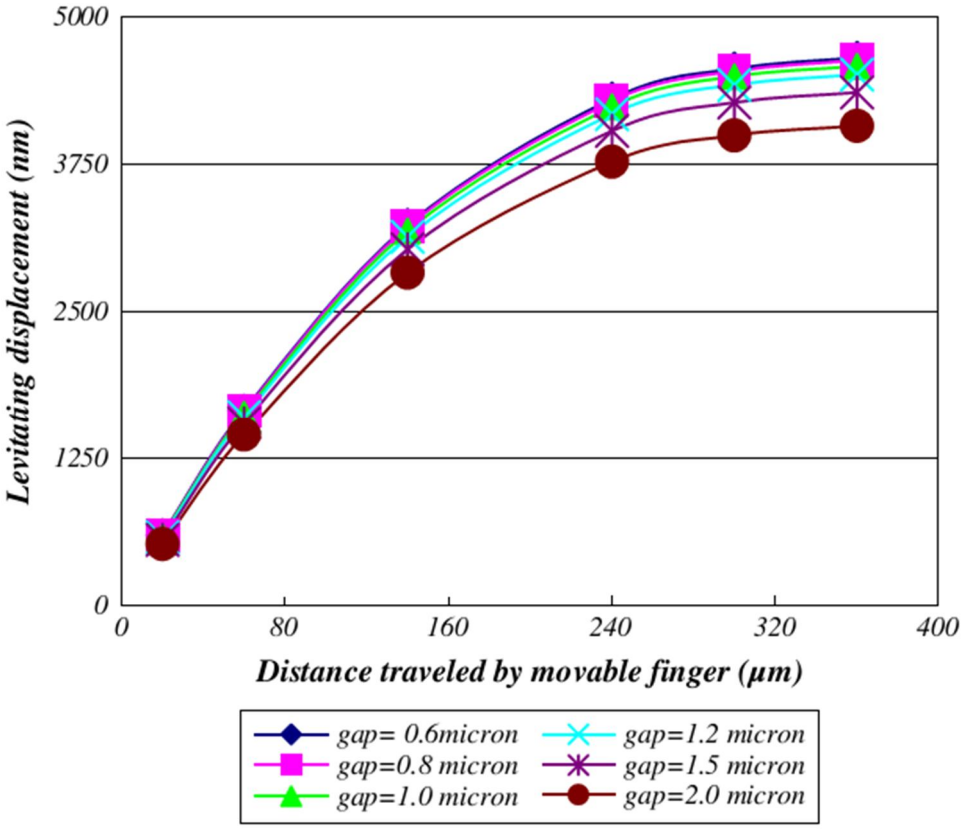

Figure 3.4: The distribution of levitating displacement for diverse distances traveled by movable finger and gaps between fingers and ground under applied voltage of 20 V [38]

3.4.2 Linearity of the Measurement

The displacement-capacitance characteristic of the force sensor is considered to be linear during modeling. However, there are non-linearities caused by the displacement and the actuation of the force sensor for readout. The non-linearity caused by the displacement, nl_d, is caused by the assumption of $x_{FS} \ll d_1^2 \ll d_2^2$ [21] as the change in total capacitance of the force sensor, ΔC, is calculated as,

$$\Delta C = 2N_{FS}\varepsilon_0 A_{FS}\left(\frac{1}{d_1^2 - x_{FS}^2} - \frac{1}{d_2^2 - x_{FS}^2}\right)x_{FS} \approx 2N_{FS}\varepsilon_0 \frac{A_{FS}}{d_1^2}x_{FS} \qquad 3.10$$

Thus, the term $[(1/d_1^2 - x_{FS}^2) - (1/d_2^2 - x_{FS}^2)]$ may cause a non-linearity on the displacement-capacitance behavior of the force sensor. Another source of non-linearity in the measurements could be the actuation voltage applied to the force sensor in order to read differential capacitance change which can be named as the non-linearity due to electrostatic force, nl_f. The electrostatic force caused by the actuation voltage, V_{FS}, can be calculated as [39],

$$F_{es} = 2N_{FS}\varepsilon_0 A_{FS}V_{FS}^2 x_{FS}\left\{\left[\frac{d_2}{(d_2^2 - x_{FS}^2)^2}\right] + \left[\frac{d_1}{(d_1^2 - x_{FS}^2)^2}\right]\right\} \qquad 3.11$$

Hence, the term $\{[d_2/(d_2^2 - x_{FS}^2)^2] + [d_1/(d_1^2 - x_{FS}^2)^2]\}$ may cause some non-linearity in the measurement of the capacitance.

Moreover, the spring softening effect may also decrease the effective stiffness of the springs of the force sensor, K_{FS}^{eff}, due to applied voltage as shown in equation 3.12 [36]. Therefore, it is important for linear measurements to keep the design limited in terms of the number of the fingers of the force sensor as well as the applied voltage for readout, and overlapping area of the two subsequent force sensor fingers.

$$K_{FS}^{eff} = K_{FS} - 2V_{FS}^2 N_{FS}\varepsilon_0 A_{FS}\left[\frac{d_1}{(d_1^2 - x_{FS}^2)^2} - \frac{d_2}{(d_2^2 - x_{FS}^2)^2}\right] \qquad 3.12$$

The total non-linearity of the measurement is kept under 5% for all designs which is the summation of the two non-linearities due to displacement and the force.

3.4.3 Simplicity of the Device

The last criterion for the device design is basically the simplicity of the actuator and the force sensor. This simplicity includes keeping the number of fingers for both parts as low as possible. Higher number of fingers, as discussed above, increase the risk of pull-in instabilities and increase the non-linearity of the measurements. Moreover, higher number of fingers, in microfabrication, means higher possibility of fabrication-related trouble.

3.4.4 Limitations Related to Microfabrication

These limits includes the minimum linewidth, *i.e.* ~2 µm, highest aspect ratios for the structures, *i.e.* ~200, and the largest depth can be etched for that highest aspect ratio. All the geometric parameters are iterated within these limits.

3.5 Finite Element Analysis of the Device

For the finite element analysis, COMSOL Multiphysics software was utilized with its Electrostatics, Deformed Mesh, AC/DC, and Plane Stress modules. The design parameters were selected using a MATLAB code given in Appendix A, considering afaromentioned design criteria. In order to simplify finite element analyses, first, 2D and 3D displacement-capacitance analyses of a single comb drive finger were compared with each other and with analytical values in the range of actuator motion during tensile testing.

The slope of the lines in Figure 3.5, $\partial C/\partial x$, is the indicator of the capacitance behavior due to displacement of each analyses type. Since the behavior of 2D analyses were not very different than the one of 3D analyses, especially for the movement range of the actuator as shown in Figure 3.5, 2D models were used for device simulations.

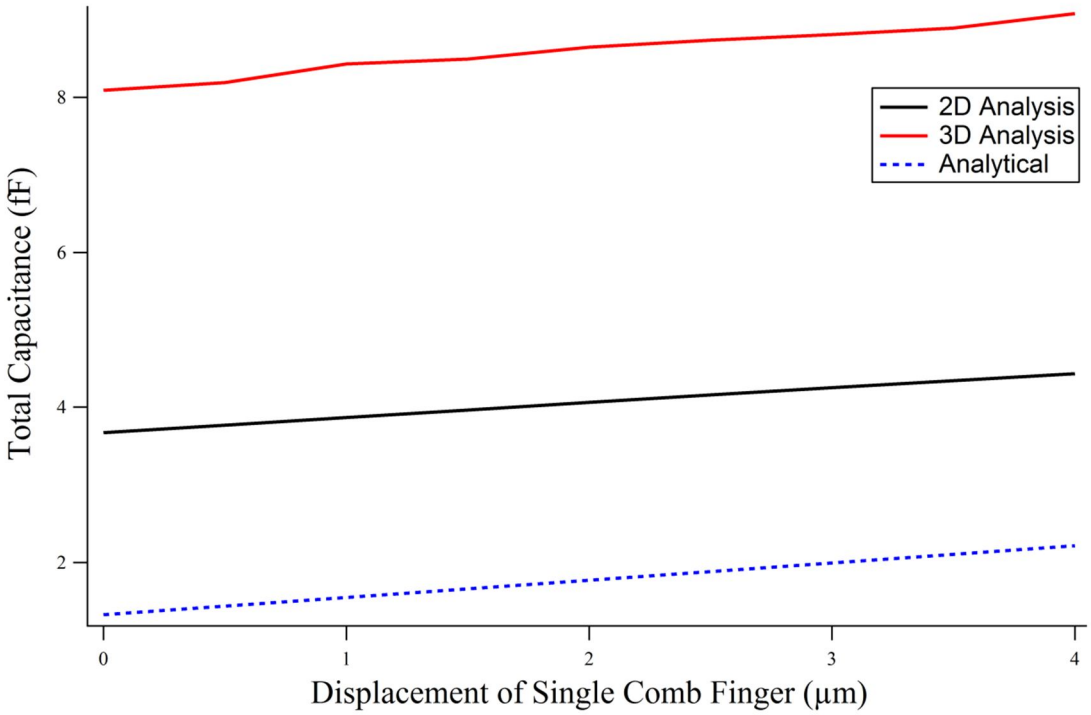

Figure 3.5: The Results Displacement-Capacitance Analyses

For the comparison of the analytical model and the finite element analyses, the sensitivity of the device, *i.e.* voltage readout from the force sensor for unit strain of the Si NW is used. Two different sets of design parameters are identified and put into COMSOL model. In order for further simplification of the finite element analyses, the microtensile device is separated into two parts. For the first part as given in Figure 3.6, voltage is applied to the actuator. The actuator is connected to Si NW at the end its shuttle and the force sensor springs were also connected to the other end of the Si NW to maintain equivalent stiffness of the whole device. By the applied voltage, electrostatic force is generated between comb drive actuator fingers and it pulls Si NW. Since Si NW is elastic, there is some amount of elongation instead of rigid body motion. This elongation transfers the movement of the actuator to the force sensor with an amount less than the movement of the actuator. This difference in motions of actuator and the force sensors is the elongation of Si NW itself. For the second part as given in Figure 3.7, the movement of the force sensor taken from the first part was prescribed to the force sensor shuttle which creates a capacitive difference resulting a voltage output.

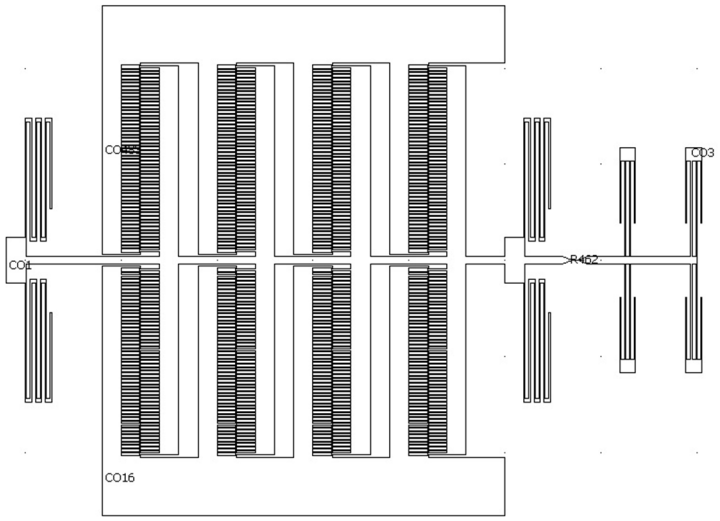

Figure 3.6: The geometry used for the first part of finite element simulations

At the end, voltage output data were plotted against the strain of Si NW. Two different designs of the actuator and the analytical model gave the same result for the sensitivity of the same force sensor design as given in Figure 3.8. This graph indicates that the analytical model generated with MATLAB code is reliable and gives concurrent data with finite element simulations.

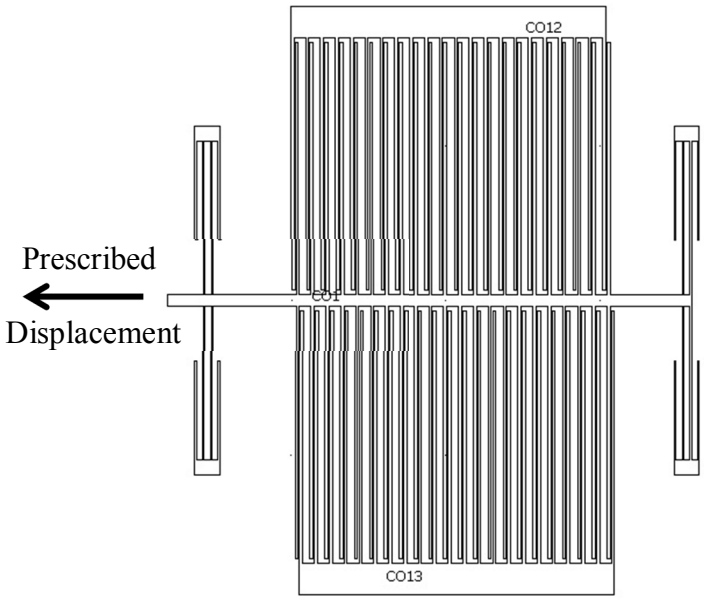

Figure 3.7: The geometry used for the second part of finite element simulations

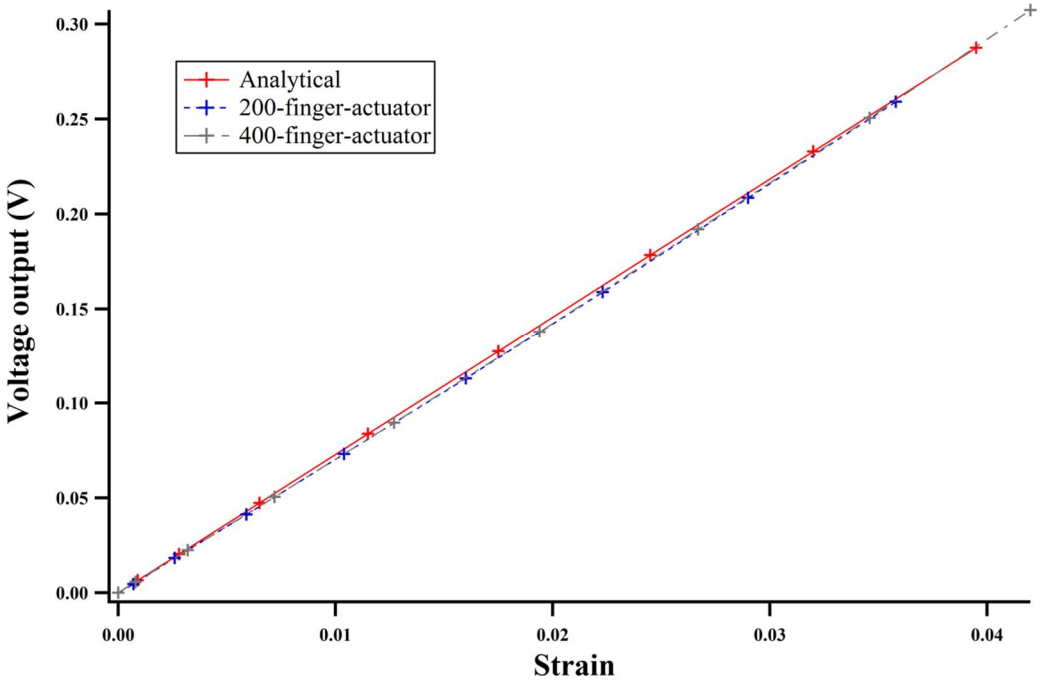

Figure 3.8: The sensitivity plot of two different designed tensile testing devices and the analytical sensitivity calculated by MATLAB code

At the end of modeling, device designs prepared for Si NWs with a diameter of 75 nm are selected for microfabrication. The specifications of these force sensors are 0.44 nm displacement and 24.28 nN force detection for every step provided that 2200 data points are taken throughout the tensile test. On the other hand, for the actuator, generated total electrostatic force is around 80 μN up to the fracture of Si NW.

3.6 Modeling of Pre-stress Indicator

For the modeling of pre-stress indicator, another MATLAB code given in Appendix A was generated. All the geometric parameters are shown in Figure 3.9 and tabulated in Table 3.3. These parameters are iterated within the code and selected with respect to four major criteria as the residual strain in the slope beam, the stiffness of the slope beam and, the buckling effects in the slope beam and in the test beam. A residual stress is assigned to the test beam and the movement of the indicator beam is calculated by the code. The analytical result given by the code is compared with COMSOL simulation results. Almost no difference is found between the code and the simulation. Then a geometry is selected for the pre-stress indicator. The resulting design is chosen to indicate 20 MPa pre-stress per around 2.5 μm of indicator beam deflection.

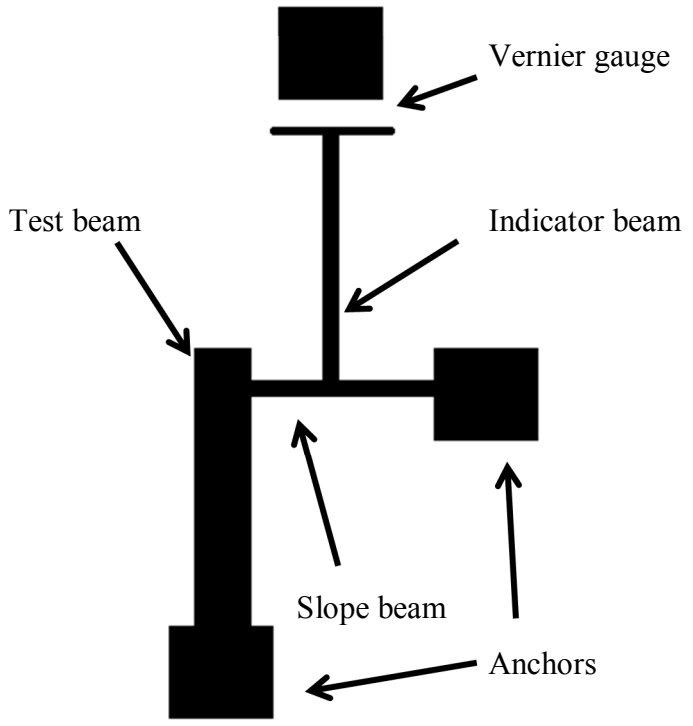

Figure 3.9: The pre-stress indicator design

w_{ib}	Width of indicator beam
l_{ib}	Length of indicator beam
w_{sb}	Width of slope beam
l_{sb}	Length of slope beam
w_{tb}	Width of test beam
l_{tb}	Length of test beam

Table 3.3: Table of indicator parameters

Chapter 4

FABRICATION

4.1 Overview

In this chapter the microfabrication procedures will be discussed. Fabrication was performed in the cleanroom facilities of Center of Micro and Nanotechnology (CMi) at Swiss Federal Institute of Technology Lausanne (EPFL). The fabrication period is composed of two parts: the test structures and the calibration devices. These two parts will be discussed individually. The results from the first part and the modifications made up for the second part will be given thoroughly. The first part of fabrication was carried out in November and December in 2011. The second part was carried out in January and February in 2012.

4.2 Microfabrication: Part I

As the first step of microfabrication, process flow was identified which may also affect the photolithography mask design. This first batch includes test structures for further definition of the design parameters. The process flow for first batch is given in Figure 4.1 for the cross-section of released fingers of the device.

For all designs, 4" SOI wafers with 50 µm of device layer thickness and 2 µm of BOX layer were used. These SOI wafers are Boron doped (p type) and have a resistivity range of 1-10 Ω-cm. The photolithography masks which are given in Appendix B were prepared on 5" Cr blanks with photosensitive resist (PR) on them using Heidelberg DWL200 Laser Lithography system. Once the laser lithography on Cr blank was done, Cr etching was executed and then PR was removed. The two different runcards are given in Appendix C which are followed for two SOI wafers.

The first step shown in Figure 4.1, (a), is the wafer preparation for photolithography. For this step, wafers were put into hexamethyldisilzane (HMDS) prime oven for about 20 minutes processing.

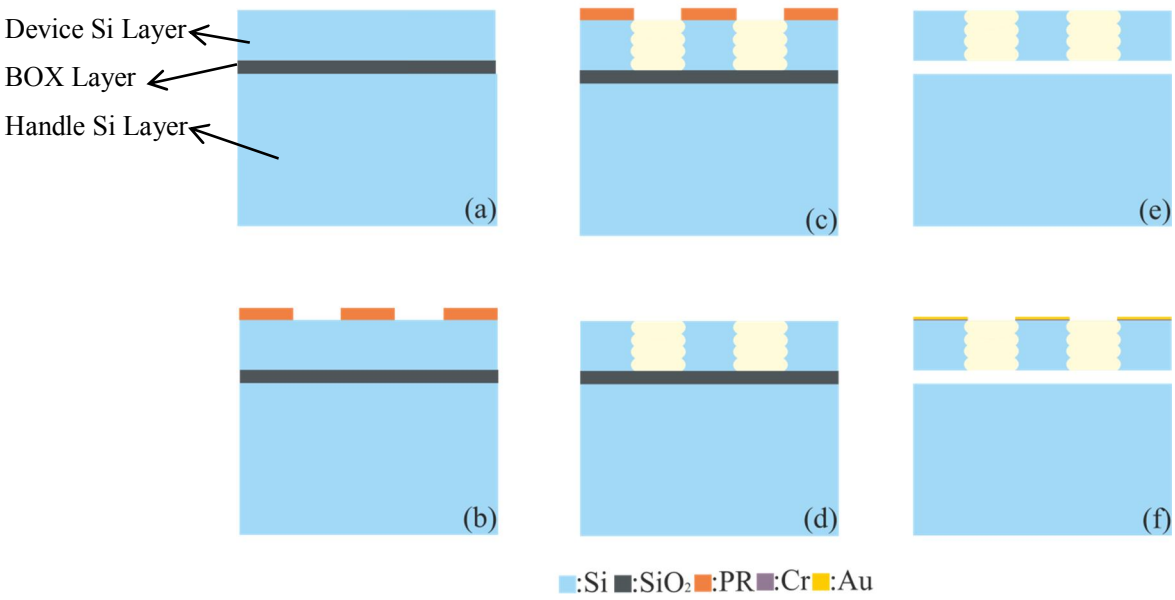

Figure 4.1: Process flow for the first batch (a) Wafer preparation, (b) Photolithography, (c) Bosch process, (d) Resist removal, (e) Dicing and HF vapor release, (f) e-beam evaporation

After preparation, in step (b), photolithography of the test structures and devices was carried out. This includes first the coating of 2 µm thick PR, AZ92XX series, using Ritetrack 88 Series Automatic Coater. Then, this PR was exposed using Süss MA150 Double Side Mask Aligner. The exposure time is a critical fabrication parameter for the correct definition of dimensions. Overexposure may result in bigger dimensions while underexposure may result in smaller dimensions than that of designed structures. After a set of experiments, 8.5 seconds of exposure was chosen as the best resulting dimensions with the designed structures with critical dimension of 2 µm. Then, unexposed PR was developed using Ritetrack 88 Series Automatic Developer. Sample SEM images are given through Figure 4.2 to 4.4. In Figure 4.2, the comb drive fingers of the actuator are shown and seem to be uniformly defined with photolithography. In Figure 4.3, the force sensor fingers and so-called Halo fingers designed to avoid microloading effect are shown. The basis of Halo fingers is to create sacrificial trenches on large areas to maintain certain etching rate all over the wafer. In Figure 4.4, the anchor and the Vernier gauge structures are shown. As it can be seen, the Vernier fingers with 4 µm x 2 µm dimensions were well-defined.

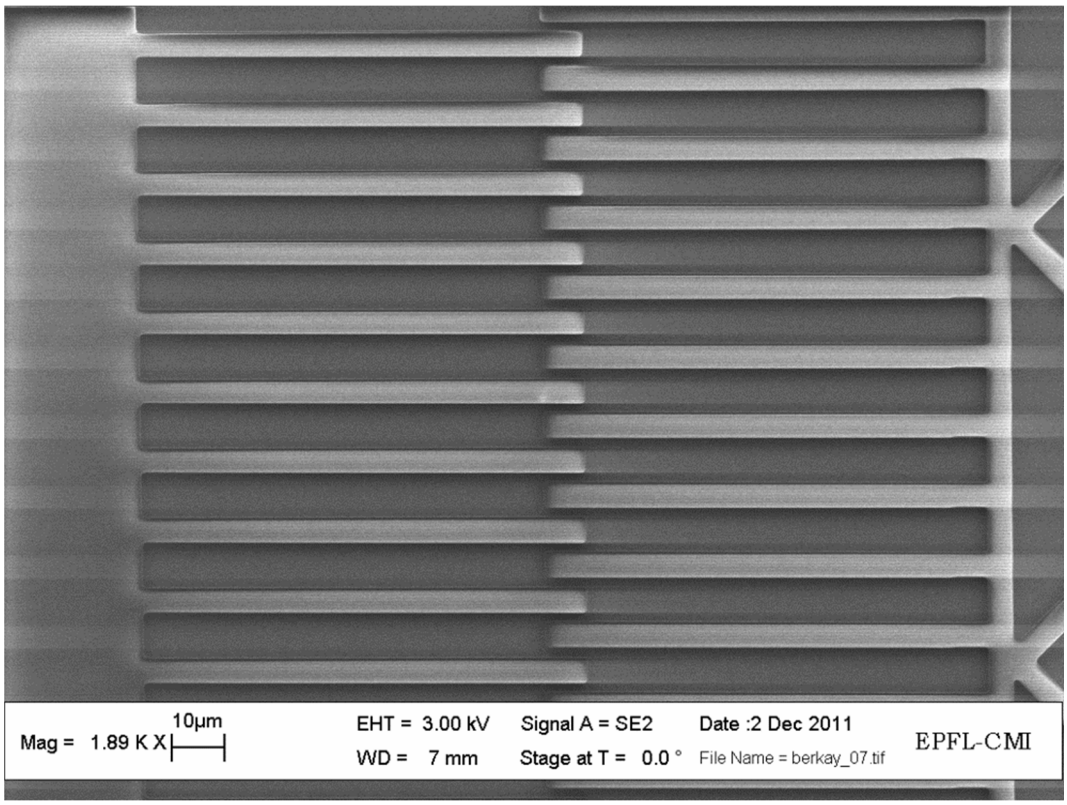

Figure 4.2: SEM image of comb drive actuator fingers after photolithography

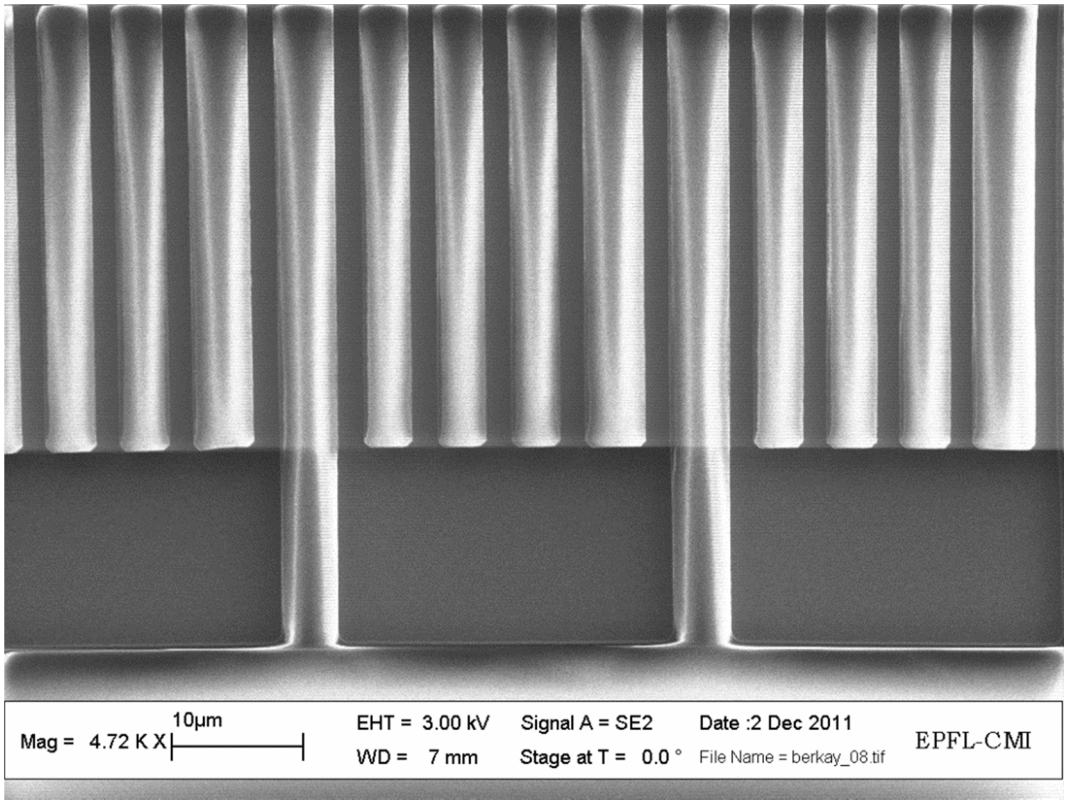

Figure 4.3: SEM image of the force sensor fingers and sacrificial fingers

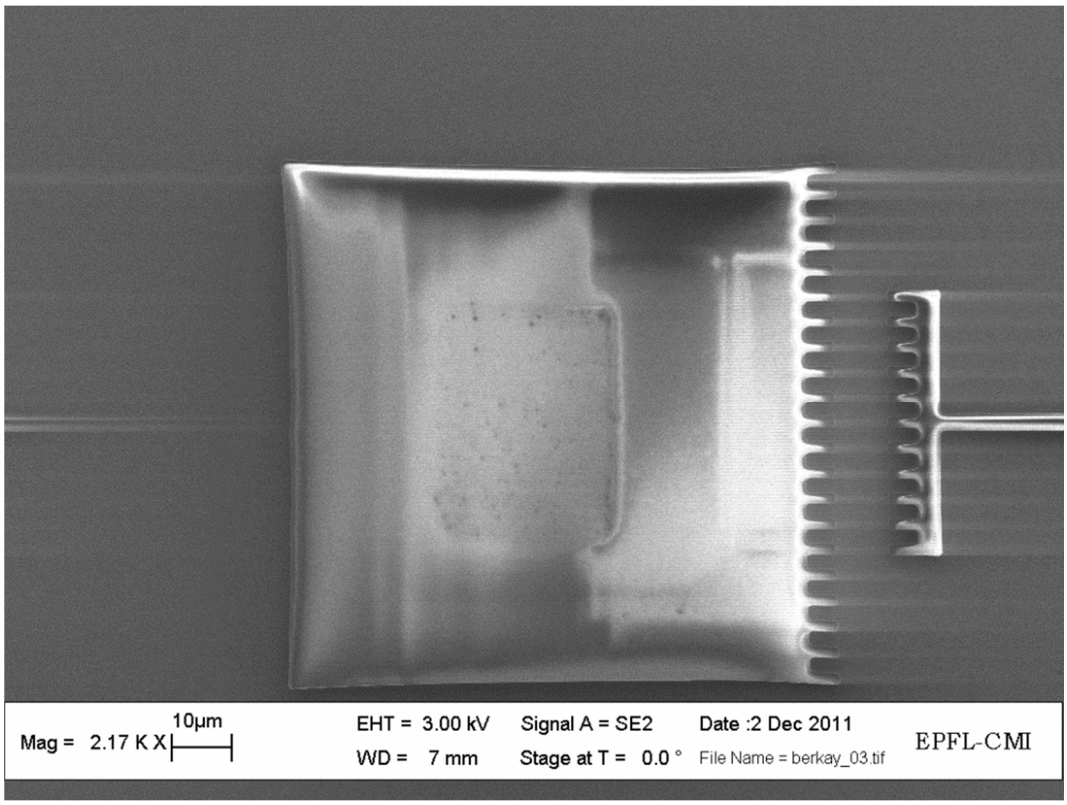

Figure 4.4: SEM image showing Vernier gauge of pre-stress indicator

In step (c), Bosch process was applied using 2 µm-thick PR as the etching hard mask. Dry etching of Si was carried out using Alcatel AMS 200 DSE with the recipe called SOI_accu++++ that is considered to prevent notching effect. The recipe details are given in Appendix D. The Bosch process is the series of subsequent steps of physical etching and deposition of a chemically inert passivation layer in order to keep etching mostly vertical [40]. In this step, the most critical parameter is the etching time for the selected recipe. There are narrow trenches within devices besides the larger areas between devices. Therefore, etching time should be well-defined in order not only to achieve BOX layer all around the wafer but also prevent overetching of structures which may cause notching as shown in Figure 4.5.

After several trials, optimum etching time was determined as 25 minutes to have 50 µm deep etching of Si on whole wafer. Since the etching rate of PR with this recipe is around 75 nm/min, there is no need to use another hard mask for etching such as SiO_2 or Si_3N_4. Sample SEM images after dry etching are given through Figure 4.6 to 4.8. In Figure 4.6, 50 µm deep etching of the indicator beam of pre-stress indicator can be seen. The wall is seen undamaged which is an indication of correct etching time. In Figure 4.7, Halo fingers can be seen with identical trenches in between. The etching depth is the same for all

trenches. The quality of etching in Figure 4.6, *i.e.* no notching effect was observed, shows that the sacrificial fingers are unnecessary in case of well-defined etching time. In Figure 4.8, tiny scallops of Bosch process can be seen those caused by subsequent etching and passivation steps.

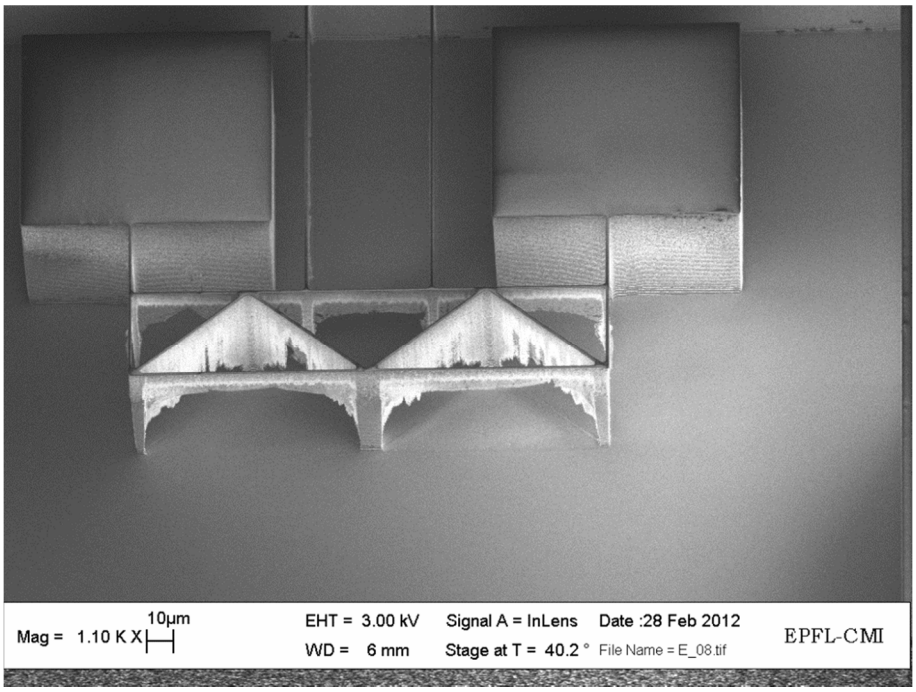

Figure 4.5: SEM image showing the effect of overetching on structures

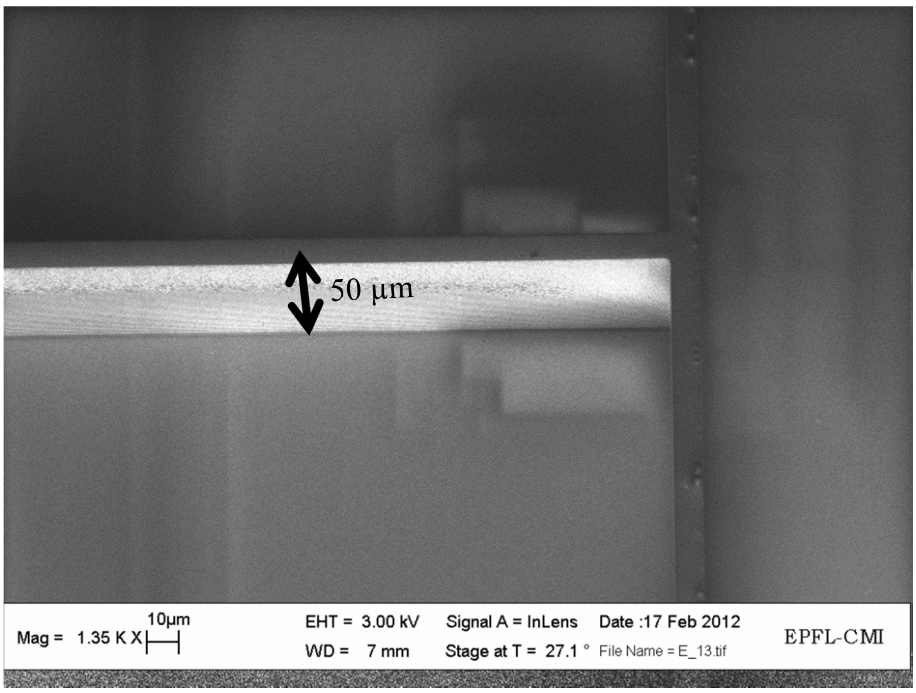

Figure 4.6: 50 µm deep etching of Si with Bosch process

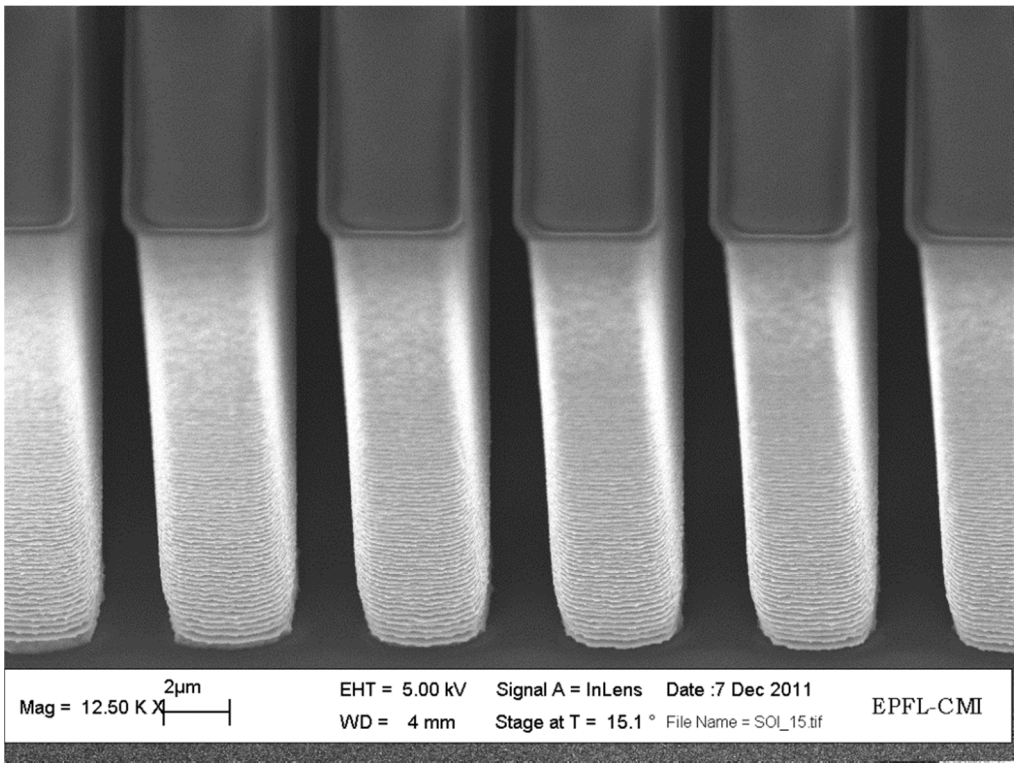

Figure 4.7: Test structures after 25 min Si etching

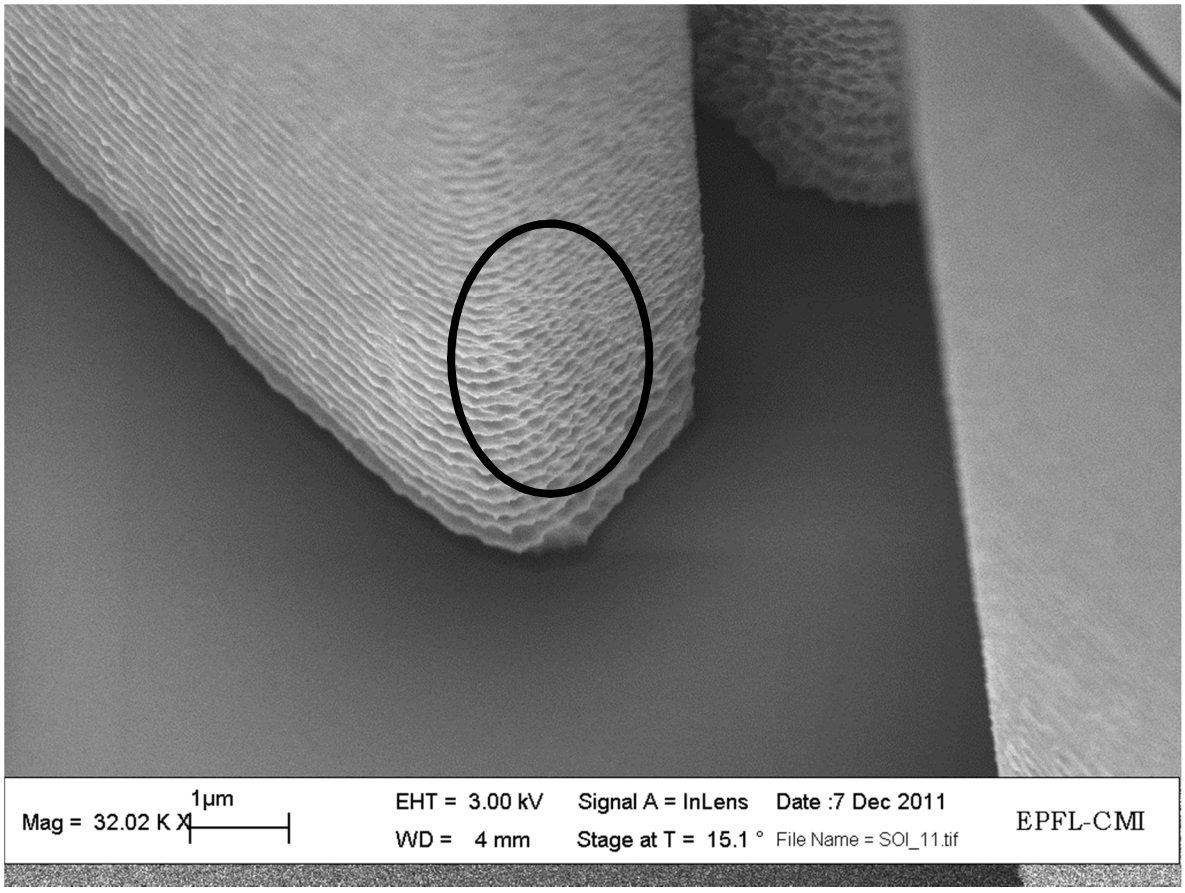

Figure 4.8: SEM image of the tiny scallops of Bosch process

In step (d), remaining PR after etching was removed with repeating steps of both wet remover using UFT Resist wet bench and oxygen plasma stripping using Tepla GiGAbatch asher. After all steps, optical inspection on the wafer was carried out in order to be sure about resist removal.The removal of PR is the last step prior to dicing which was carried out to separate wafer into chips using Disco DAD321 automatic dicing saw. Before dicing process, the wafer was coated with a thick PR to cover the structures. In addition, there is water spraying during dicing to cool the wafer. All these extra processes may cause damages as shown in Figure 4.9. In this figure, the tip of the shuttle is shown which broke during dicing.

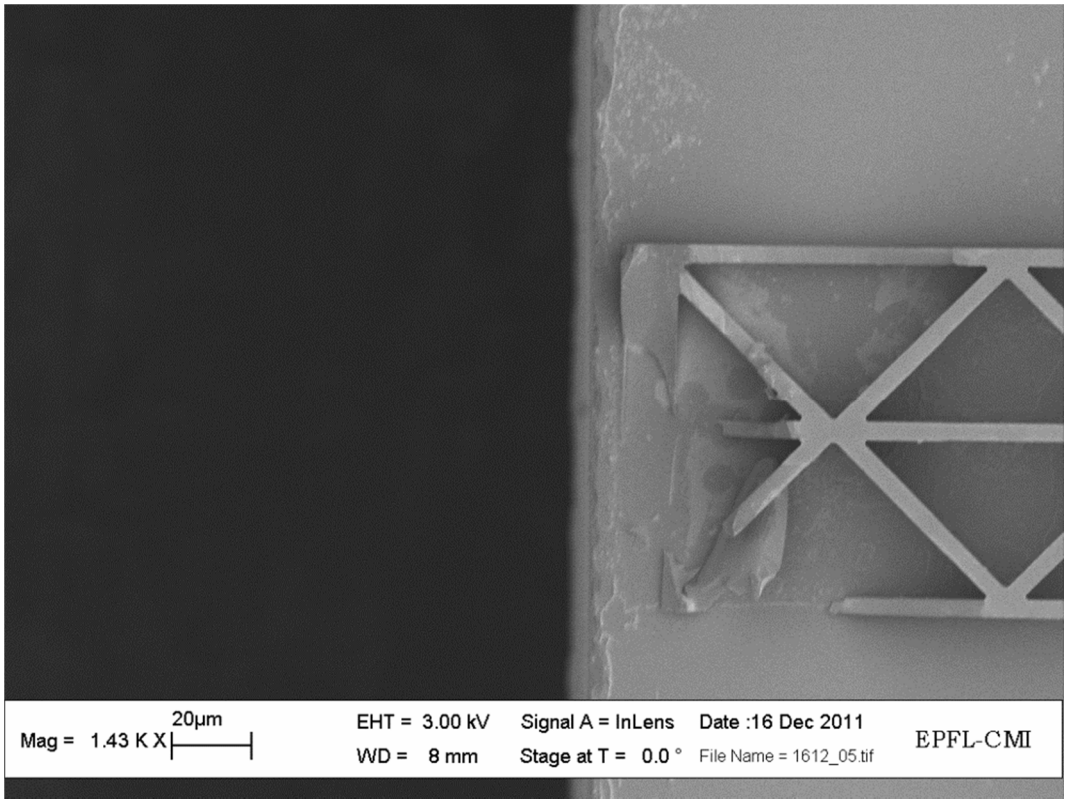

Figure 4.9: The damage of the dicing process on structures

Then, the devices on diced chips were released using IDONUS HF-VPE100 by HF vapor. HF vapor release is chosen in order to prevent stiction of released structures. The etching rate of SiO_2, *i.e.* BOX layer, is around 4-6 µm/hr, thus the release time was chosen as 2 hrs for the release of the most wide structures with the width of 12 µm. Sample SEM images after HF vapor release are given in Figure 4.10 and 4.11. In Figure 4.10, the shadow on the handle layer indicates the full-release of the structure. In Figure 4.11, indicator beam of the pre-stress indicator is the most wide beam on the wafer and it was tried to be moved by the probe of a surface profilometer to assure full-release. Since the

device is 50 µm thick, the profilometer could not step over it during surface roughness test. Instead, it moved the indicator beam a little which exhibits the beam was released.

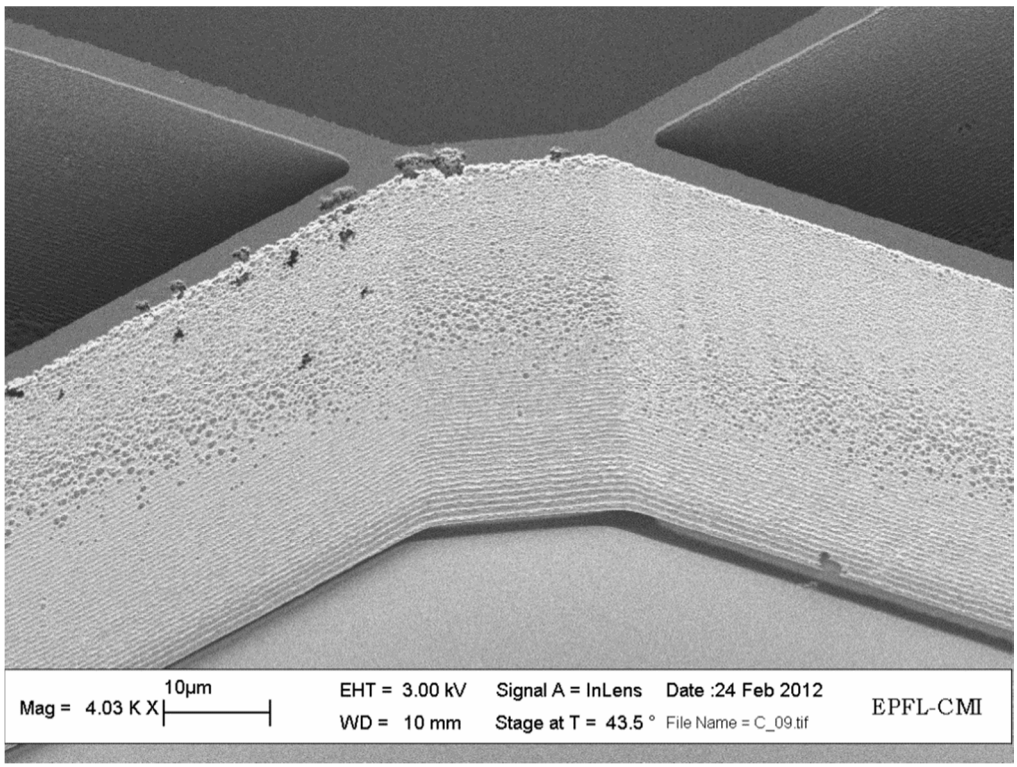

Figure 4.10: SEM image after HF vapor release

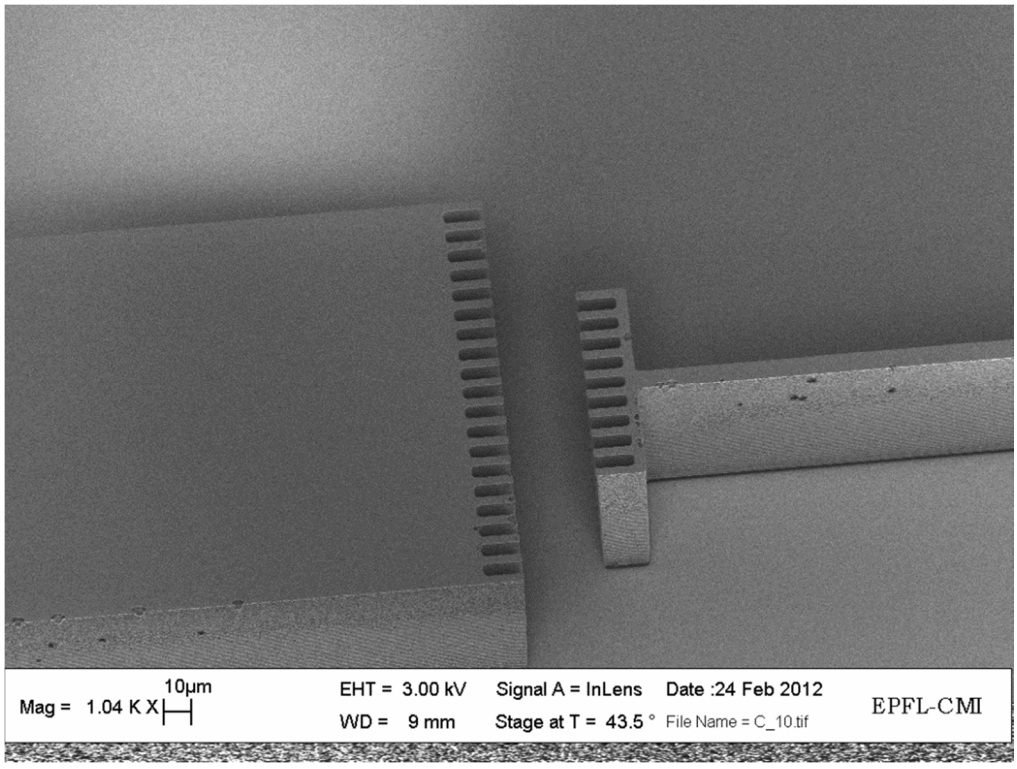

Figure 4.11: SEM image after release of the indicator beam and Vernier gauge fingers of the pre-stress indicator

The last step of the microfabrication, step (f), is the e-beam evaporation of Cr and Au on devices in order to enhance electrical conductivity during characterization. For this purpose, Leybold Optics LAB600H was used, and 10 nm Cr and 300 nm Au films were coated on the devices. This thicknesses were chosen with regard to the needs of the wedge wirebonding that may be utilized for characterization. Sample SEM images after e-beam evaporation are given through Figure 4.12 to 4.14. The coating is on horizontal surfaces as can be seen from these three figures since there is no connection between fingers or between the device layer and the handle layer. In Figure 4.13 and 4.14, fingers of the force sensor and the actuator are shown, respectively. There is not any connection between these fingers through Cr-Au coating.

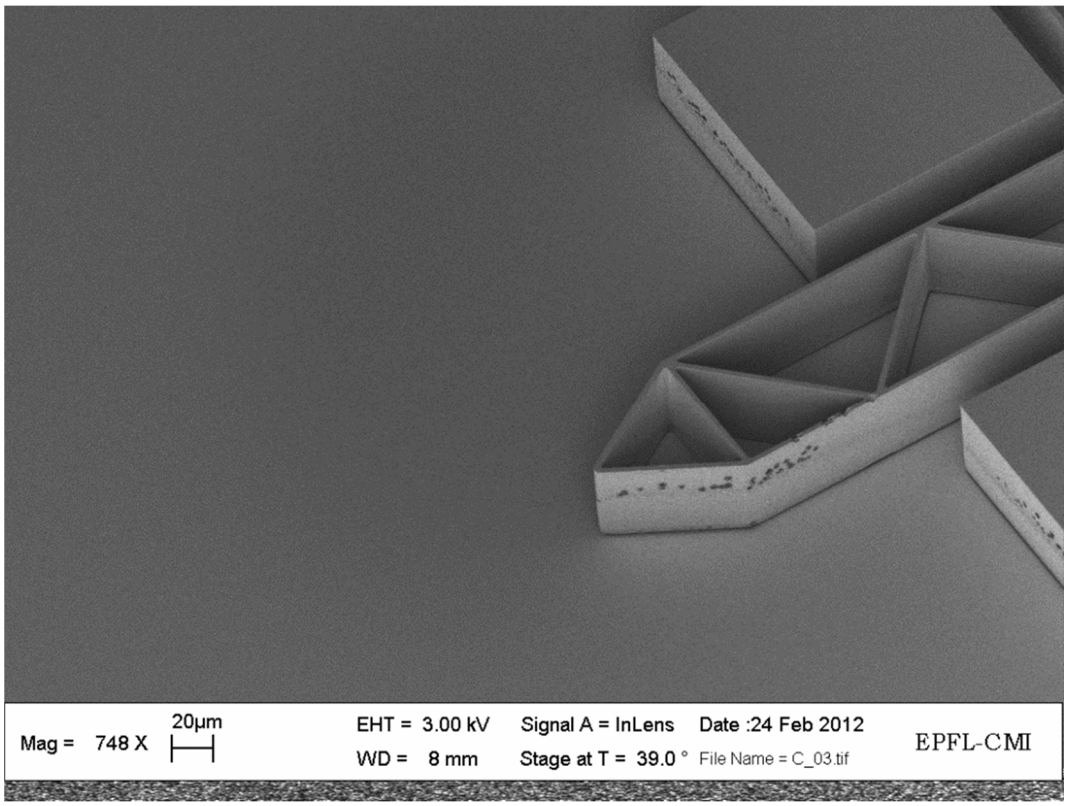

Figure 4.12: SEM image of the shuttle tip of the force sensor

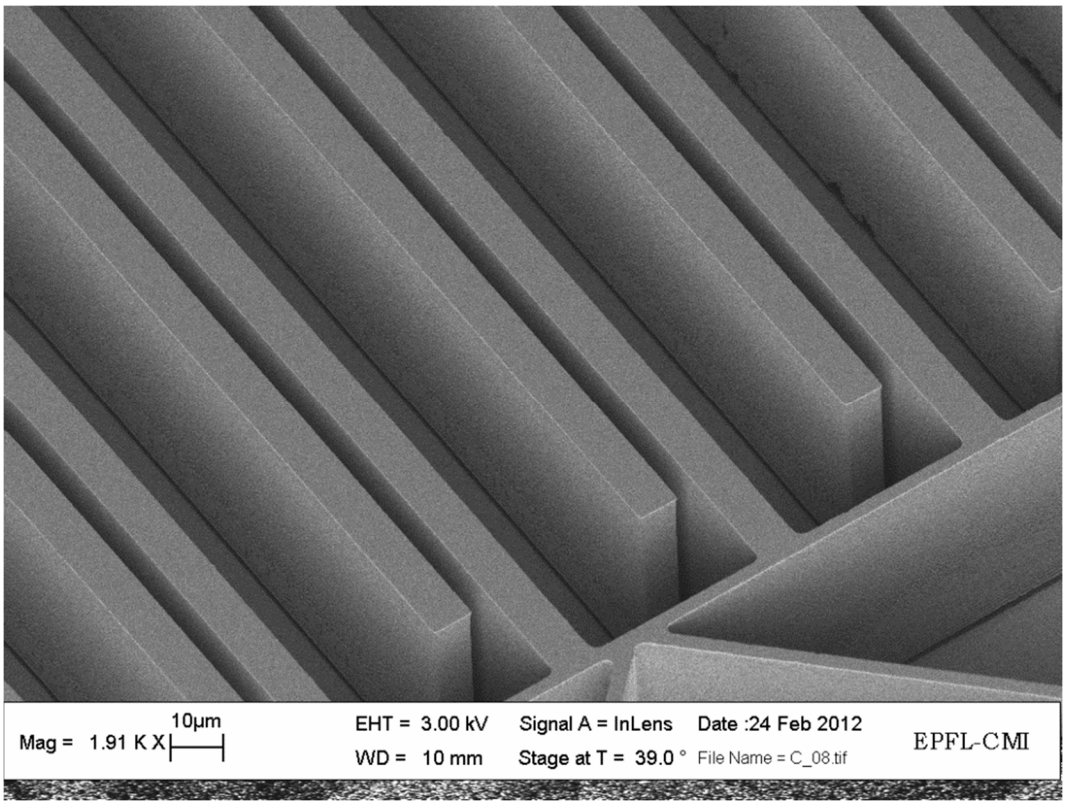

Figure 4.13: SEM image of the force sensor fingers

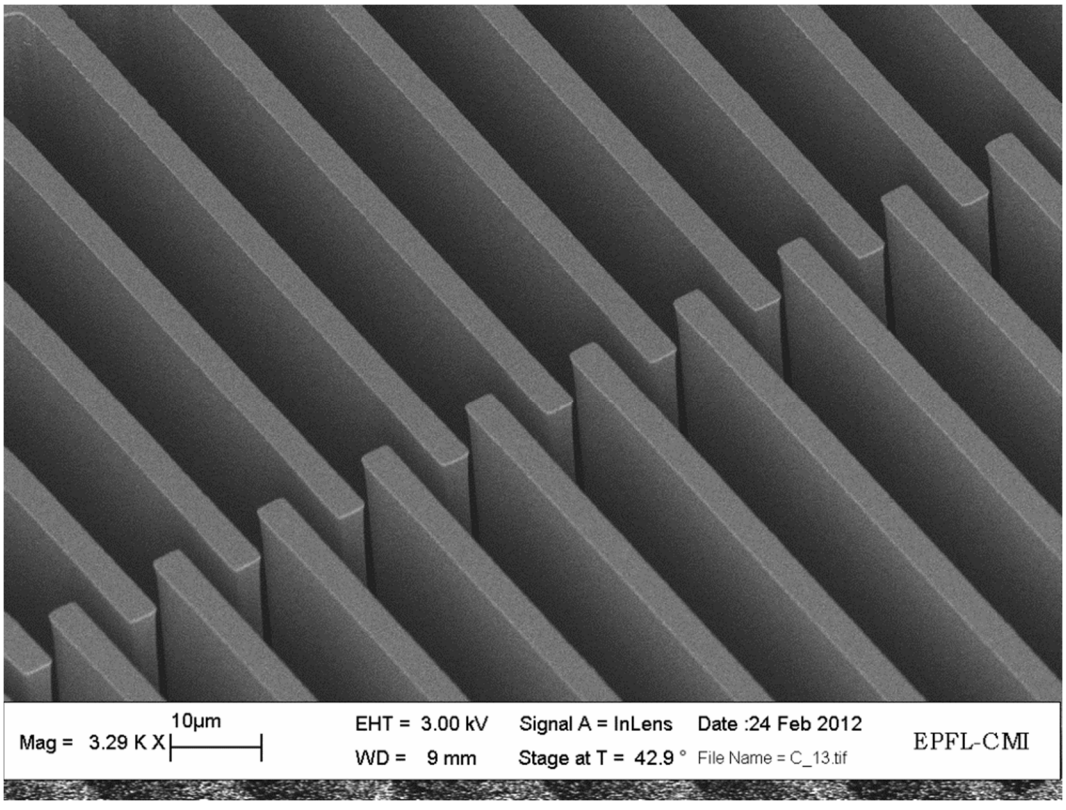

Figure 4.14: SEM image showing the actuator fingers

4.3 Microfabrication: Part II

This part of microfabrication includes the devices that are designed for stiffness calibration which are basically individual comb drive actuators and triplate capacitive force sensors without any specimen attached to them. Some modifications on the design and the process flow were made based on the results of the first part of microfabrication. These can be listed as:

(1) Maintain critical dimension as 4 μm for structures and 3 μm for trenches.

(2) Avoid dicing. Use scribing instead.

(3) No need for Halo fingers.

The first and the third modifications were made on the design part while the second one was modified through process flow. According to this modification, the only change made in the process flow is utilizing scribing instead of dicing in Figure 4.1. The scribing was carried out manually with RV125 Diamond Scriber at EPFL. Scribing the wafer eliminates the effect of additional PR coating and water spray damage. On the other hand, MEMS design was changed according to critical dimension needs.

At the end of the second period of microfabrication, chips including individual actuators and force sensors designed for stiffness calibration were packed and brought for characterization as will be discussed in the coming chapter. The new device designs are shown in Figure 4.15 and 4.16. These devices includes large pads, *i.e.* 500 μm to 500 μm, for probing which are kept far to decrease the noise. The inventory brought to Istanbul is given in Table 4.1. The "new design" indicates the design for the second batch. The reason that there is no working "old design" force sensor is that the damage during etching as illustrated in Figure 4.5. There is notching on structural beam springs of the "old design" force sensor due to overetching since the linewidth of these beams is 2 μm. This shows the first modification is appropriate.

These devices then investigated to compare designed and fabricated dimensions. The results are shown in Figure 4.17 to 4.20. In Figure 4.17, a set of actuator fingers are shown and the width of a finger is measured by SEM. The designed value for that width is 5 μm whereas the fabricated dimension is around 4 μm. In Figure 4.18, the width of the structural beams of the actuator is shown and the measured values are around 3.5 μm. The actual designed width of these beams is 4 μm. In Figure 4.19, force sensor fingers are shown. The designed value for these fingers is 10 μm, while the fabricated dimension is a

little different. In Figure 4.20, the beam springs of the force sensor is shown. The widths of these beams were fabricated as around 4.5 µm instead of the designed value of 5 µm. Further analyses were also done statistically by taking at least five different measurements of the widths of the fingers and beam springs and also the gaps between fingers of both the actuator and the force sensor. These analyses were carried out on different devices placed on different chips. The average results of these analyses are tabulated with the actual designed values in Table 4.2.

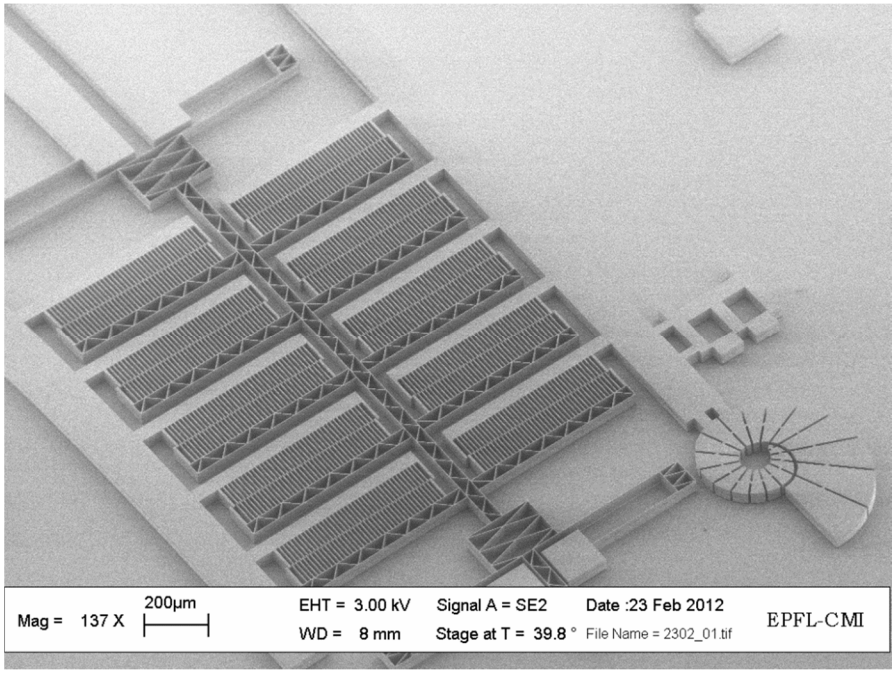

Figure 4.15: The actuator designed for stiffness calibration

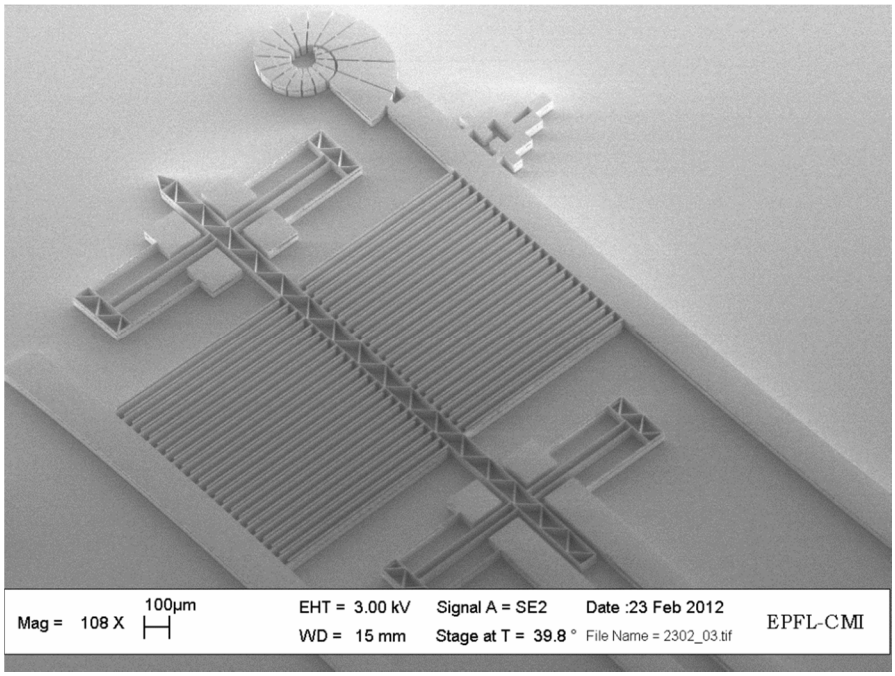

Figure 4.16: The force sensor designed for stiffness calibration

Type of the device	Number of working devices
Old design force sensor/actuator	0/6
New design force sensor/actuator	9/9

Table 4.1: The device inventory after both microfabrication periods

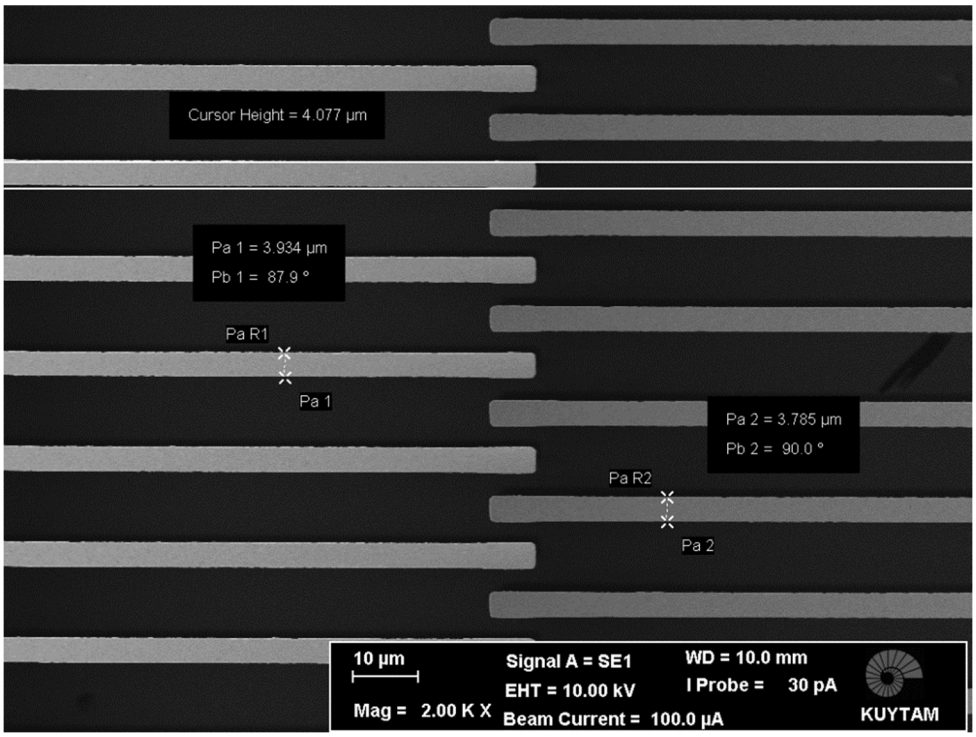

Figure 4.17: The width of the comb fingers

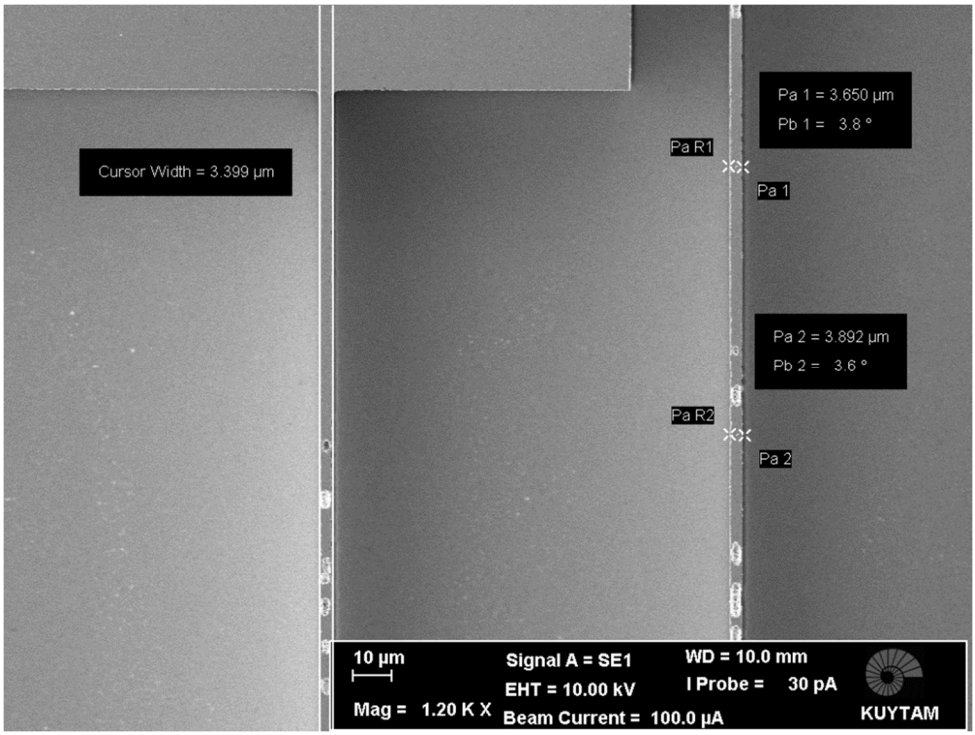

Figure 4.18: The actuator spring beams

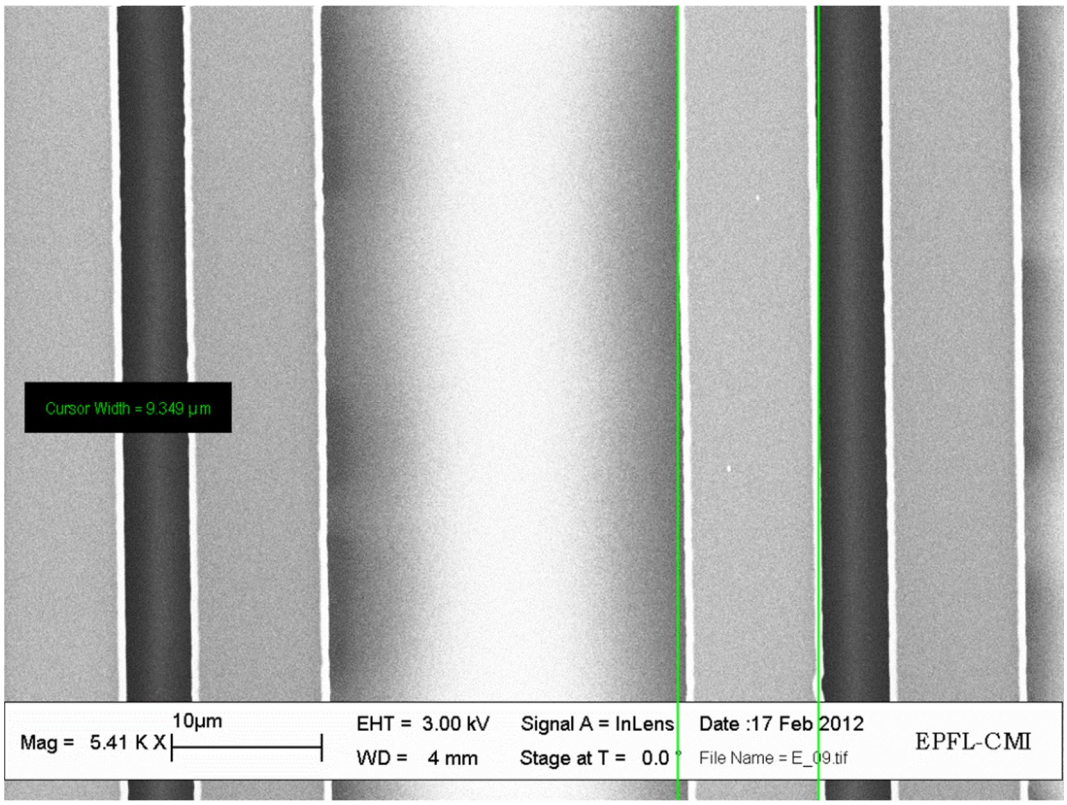

Figure 4.19: The width of the sensor finger

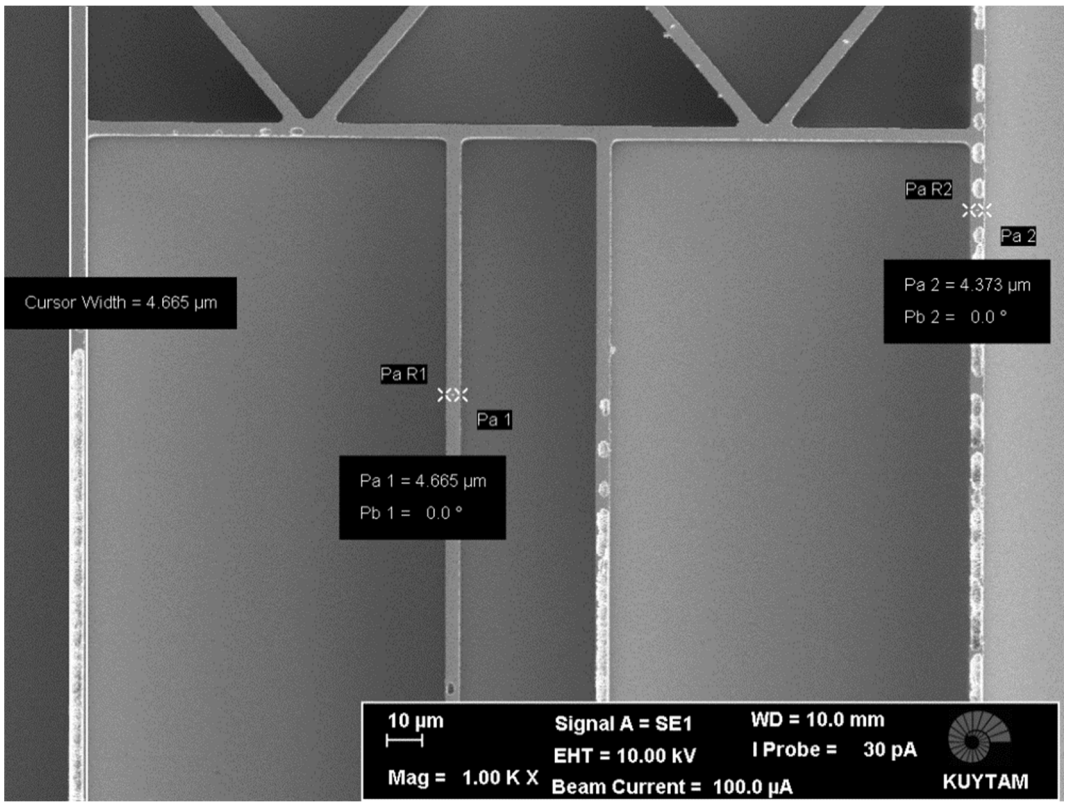

Figure 4.20: The structural beam springs of the force sensor

Geometric Parameters (µm)	Actuator		Force Sensor	
	Designed	Fabricated	Designed	Fabricated
Width of the finger	5	4.28	10	10.04
Gap between fingers	g_y=2	g_y=3.14	d_1=4 d_2=24	d_1=5.91 d_2=26.35
Width of the beam springs	4	3.64	5	4.40

Table 4.2: The comparison of designed and fabricated dimensions

4.4 Proposed Process Flow for NW Fabrication

The microfabrication of the MEMS part of the device is the first step of the microfabrication of the whole device. The second step is the fabrication of a single Si NW with the etch depth of 50 µm. Then, the last will be the integration of these two processes to achieve single-chip MEMS-NW integrated microtensile testing device. For the second step, a process flow is proposed utilizing atomic layer deposition (ALD) of alumina as given in Figure 4.15.

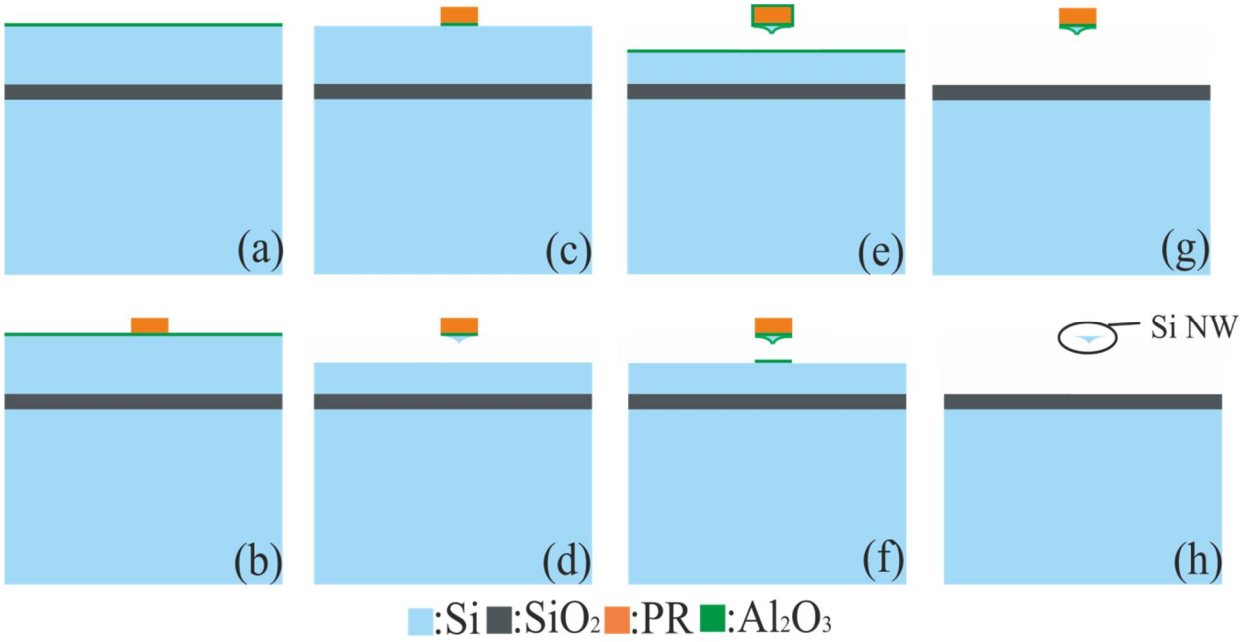

Figure 4.21: Proposed process for single Si NW fabrication (a) ALD Al_2O_3 deposition, (b) e-beam lithography, (c) Al_2O_3 etching, (d) Si etching (Bosch process), (e) ALD Al_2O_3 deposition (f) Al_2O_3 etching, (g) Si etching, (h) Resist removal and Al_2O_3 etching

The basic idea of this process is to protect Si NW using ALD Al_2O_3 as an envelope around it throughout the whole flow. Due to high amount of undercut during the Bosch process it is very unlikely to maintain passivation of all layers including around the Si NW at the top. Therefore, while etching Si down to BOX layer, *i.e.* 50 μm, it is difficult to prevent Si NW from etching until the end of etching cycles. Hence, a process flow was constructed and a few trials were made. In step (a), Al_2O_3 is deposited with ALD method. The thickness of the Al_2O_3 is critical since it should be thick enough to serve as the mask for Si etching in case e-beam resist is stripped during etching. Then, in step (b), e-beam lithography is carried out to define NW region. The thickness of the e-beam resist should be determined precisely. There is an upper limit for this thickness coming from the e-beam lithography itself. There is a ratio of the thickness of the resist to the width of the structure that is to be defined. As the width of lithography is decreased, *i.e.* smaller diameters for Si NW, maximum allowable thickness value is decreased as well. However, there is a lower limit for the resist thickness as it will be serving as the mask for Al_2O_3 etching. Moreover, the e-beam resist is also etched during Al_2O_3 etching steps, therefore, the etching rates of e-beam resist during Si and Al_2O_3 etching should be determined. In third step, (c), Al_2O_3 is etched down to Si device layer. After that, in step (d), single Si NW is formed by Bosch process with a depth around 1 μm. The etching process is a two-step procedure with two different recipies called Z_SOI_accu and SOI_accu+++. The first step is 7 seconds and the second step is 20 seconds. The recipe details are given in Appendix D. Then, in step (e), a thin layer of Al_2O_3 is deposited again with ALD in order to form the envelope-like structure around Si NW. In step (f), anisotropic Al_2O_3 etching is carried out to reach Si and in step (g) remaining Si is etched down to BOX layer. At the end, in step (h), Al_2O_3 is etched anisotropically in order to have Si NW released.

In the first trials of this flow the main problem was the durability of the e-beam resist as the mask for Al_2O_3 etching at step (c). There is an upper limit for the resist thickness to define the narrow NW width. Since the NW diameter was designed to be 75 nm, this upper limit was determined as around 300 nm. This thin layer of e-beam resist could not endure Al_2O_3 etching with Ar ion milling process using Alcatel AMS 200 DSE. In order to prevent this issue, other processes should be tried for Al_2O_3 etching or the initial thickness of the Al_2O_3 should be optimized and kept as small as possible. A possible process can be the one called Saphir using STS Multiplex ICP dry etcher.

Chapter 5

CHARACTERIZATION

5.1 Overview

For the characterization of fabricated devices, *i.e.* comb drive actuators and capacitive sensors, the voltage-capacitance characteristics were investigated. Electrical characterization experiments were conducted in Micro and Nanocharacterization Laboratory (MNL) at Boğaziçi University, Istanbul. In this chapter, the procedures will be given and the results will be discussed.

5.2 Characterization of the Actuator

For the comb drive actuator, Keithley 4200 SCS semiconductor parameter analyzer with CV unit was used as shown in Figure 5.1. The probing was carried out using Cascade M-150 Probe Station. DC voltage is applied to the fixed combs of the device up to 5 V and shuttle was grounded, *i.e.* connected to low current-potential channel of the analyzer.

The handle layer was grounded by grounding the sample chuck of the probe station and directly using another probe. However, native oxide on handle layer or metal coating creates a capacitance source since it prevents handle layer from grounding. This extra capacitance source should be considered as it may affect the results.

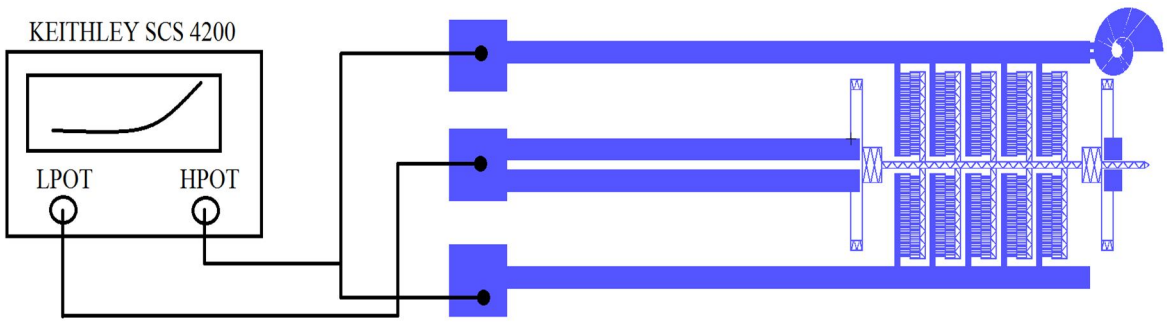

Figure 5.1: Actuator charactetization setup

Total capacitance measurements were taken from different devices as given through Figure 5.2 to 5.5. The first three devices are on the same chip from the first SOI wafer on which 25 minutes of Si etching was done. For the second SOI wafer, on the other hand, etching time was 20 minutes. The letters A, B, and C designate the three same-designed

devices on one chip. The results of the 10 subsequent measurements have very small standard deviation for a certain device, however, there are some differences in total capacitance values between devices. These 10 measurements were taken in series under same conditions on the same day. This small standard deviation may be caused mainly by the measurement environment and equipments.

Although the total capacitance value levels are different for four different devices, the change in total capacitance of the actuator, *i.e.* $C_{total}\ (at\ V = 5V) - C_{total}\ (at\ V = 0)$, does not vary too much. Moreover, the change in capacitance simulated through COMSOL coincides with the experimental results with a very small deviation as given in Figure 5.6. This simulations were done using the fabricated dimensions tabulated in Table 4.2.

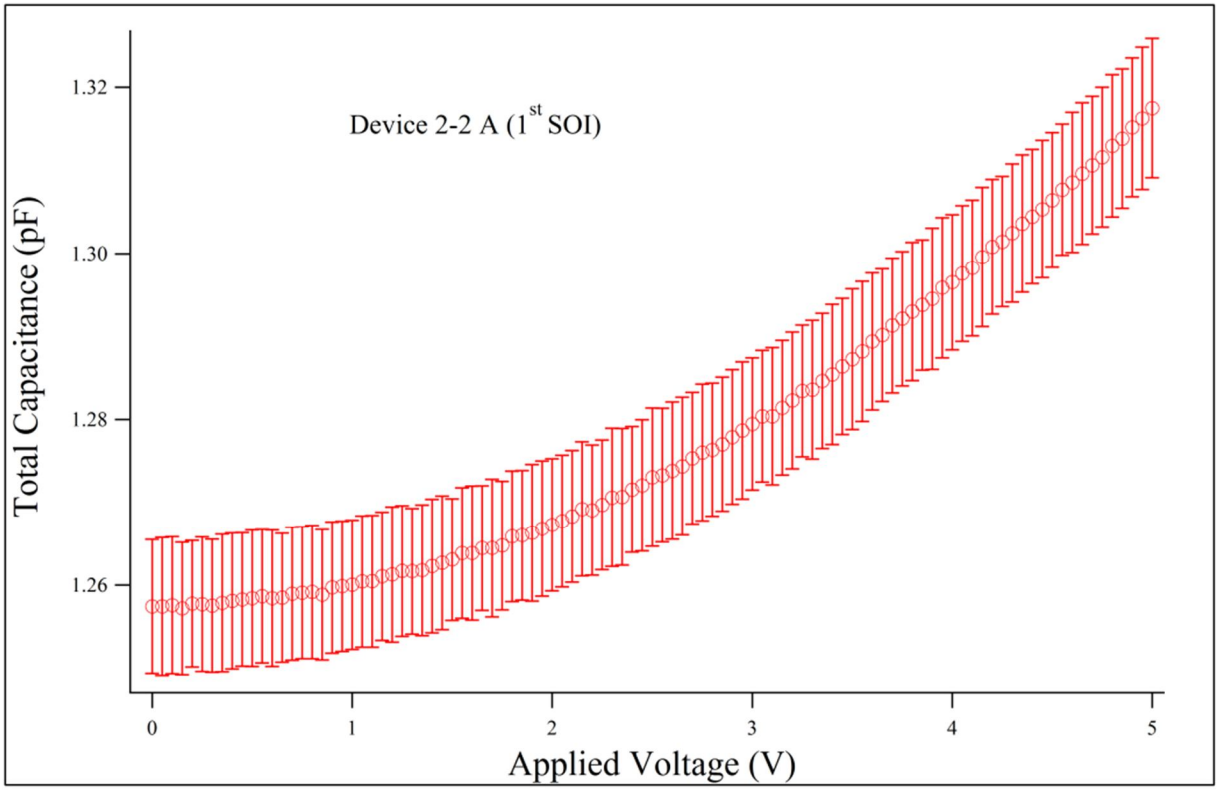

Figure 5.2: C-V characteristic of device 2-2 A from 1st SOI

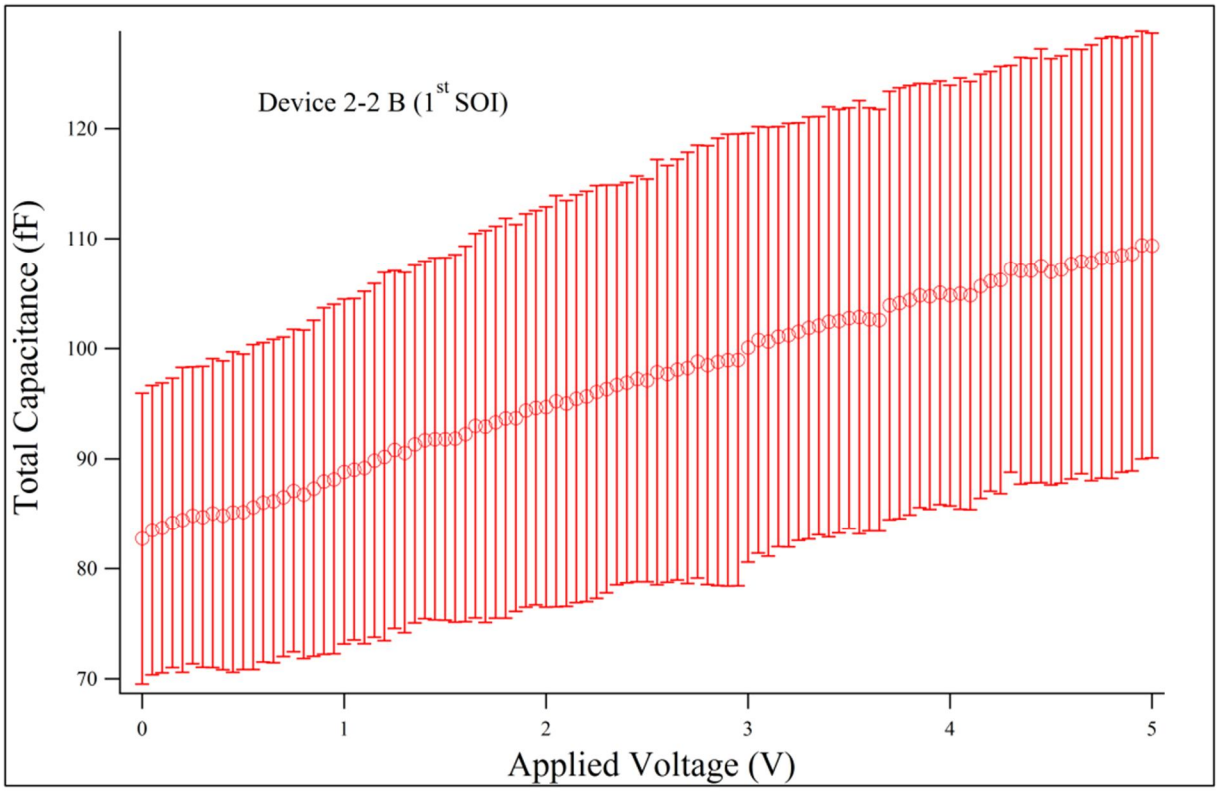

Figure 5.3: C-V characteristic of device 2-2 B from 1st SOI

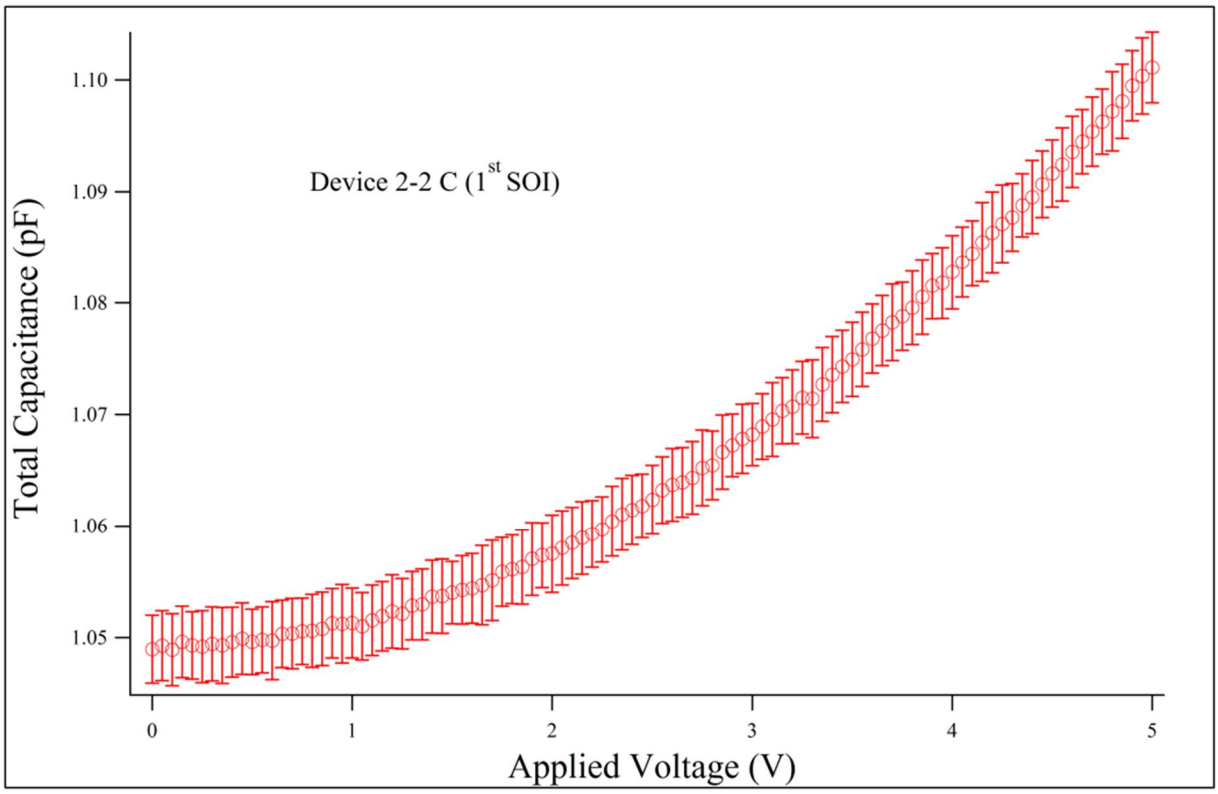

Figure 5.4: C-V characteristic of device 2-2 C from 1st SOI

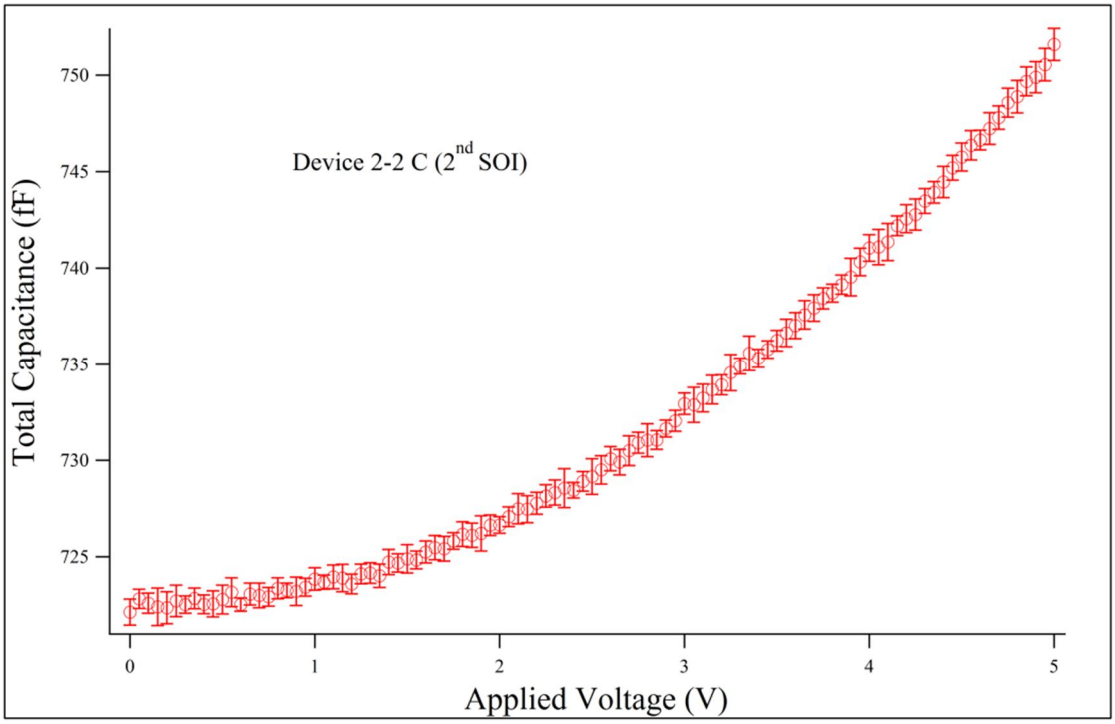

Figure 5.5: C-V characteristic of device 2-2 C from 2nd SOI

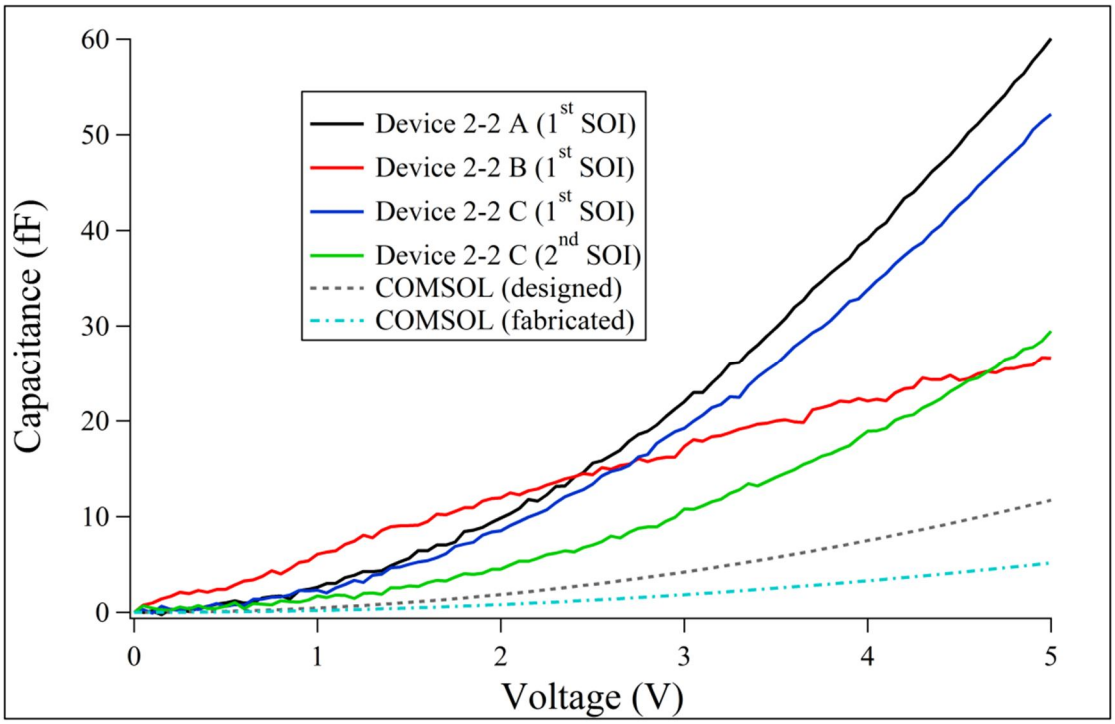

Figure 5.6: The change in capacitance of measured actuators compared with simulation results

This deviation is mainly caused by the extra capacitance sources such as the probes and the specimen chuck of the probe station. The less capacitance change in the simulation of fabricated device than the one of designed device is caused by the increased gaps between

fingers, on the other hand. Although the spring widths are decreased, *i.e.* larger displacement of the actuator, the change in capacitance is decreased, since the gaps are increased.

5.3 Characterization of the Force Sensor

The same experiments were executed on the force sensors to observe the CV characteristics of the devices as illustrated in Figure 5.7. The grounding problem for handle layer explained in previous section was remained in force sensor characterization. The effect of the extra capacitance sources will be considered during discussion of the results. Moreover, dynamic characterization of the force sensor was carried out which is explained in Appendix E. However, there are no results from these experiments due to high noise levels during the characterization.

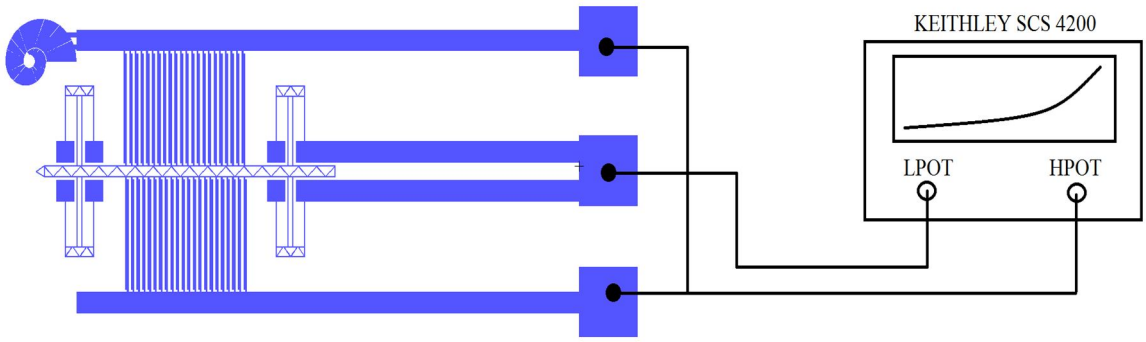

Figure 5.7: The force sensor characterization setup

The graphs in Figure 5.8 and 5.9 show the total capacitance values for two different force sensors. Each of the devices was again tested 10 times. These tests were carried out on the same day and in the same environment. Both of the devices are on the same chip from the first SOI that was etched for 25 minutes.

Similar to the actuator part, the change in total capacitance values can be examined by taking an offset approach as given in Figure 5.10. The graph shows very close results of the change in capacitance for the experiments and simulation. This very small deviation in values from the simulations are basically caused by the extra capacitance sources as exemplified in the previous section.

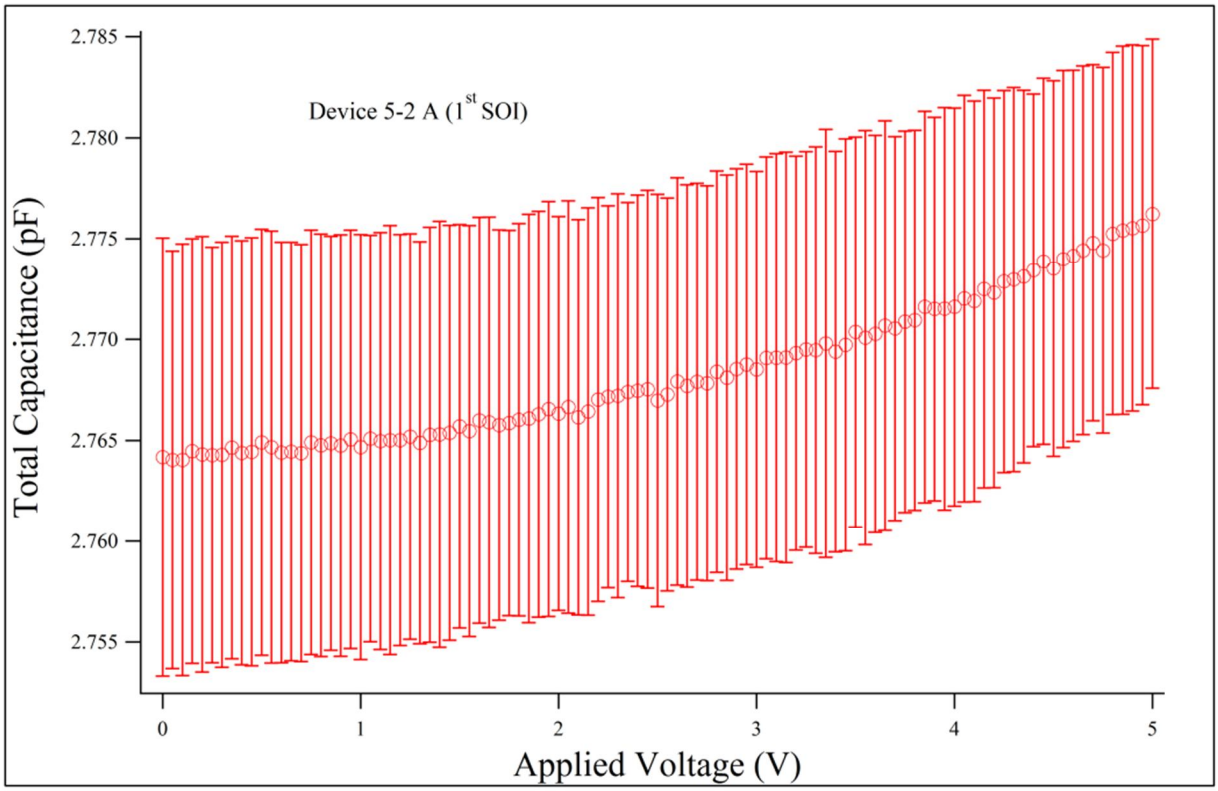

Figure 5.8: C-V characteristic of device 5-2 A from 1st SOI

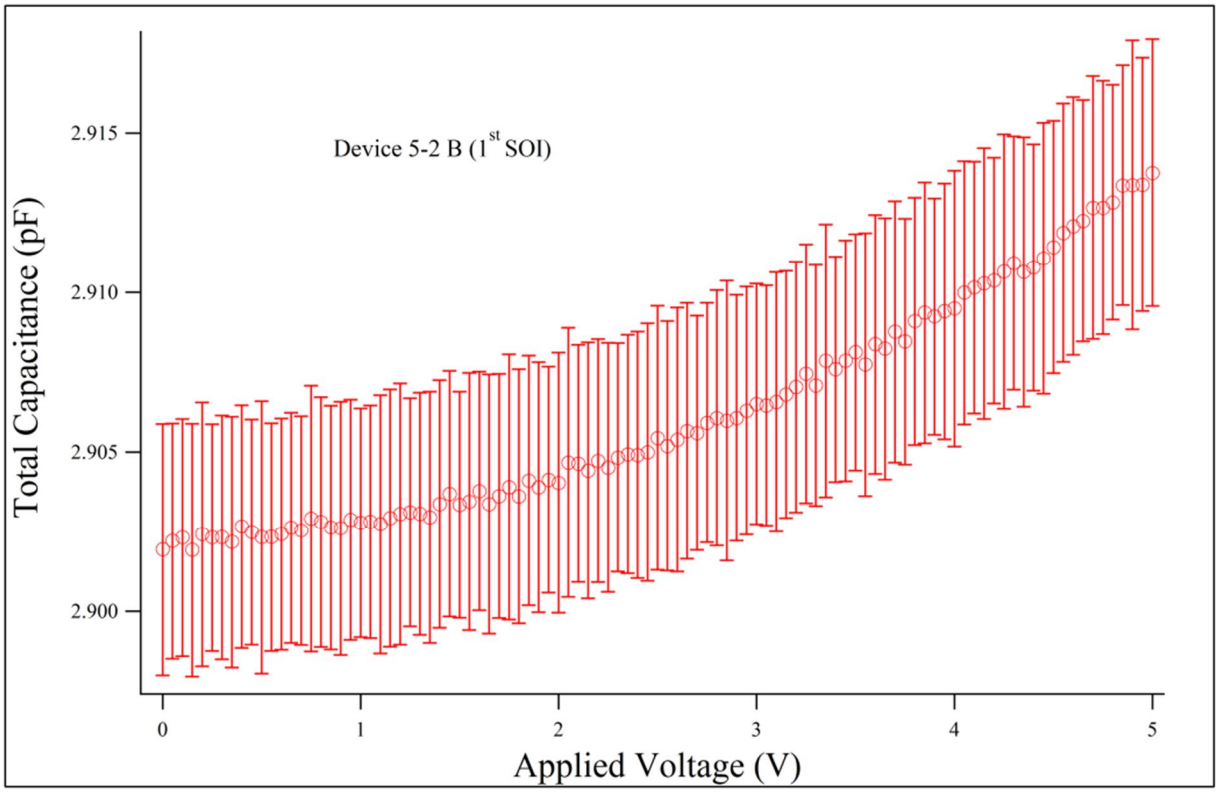

Figure 5.9: C-V characteristic of device 5-2 B from 1st SOI

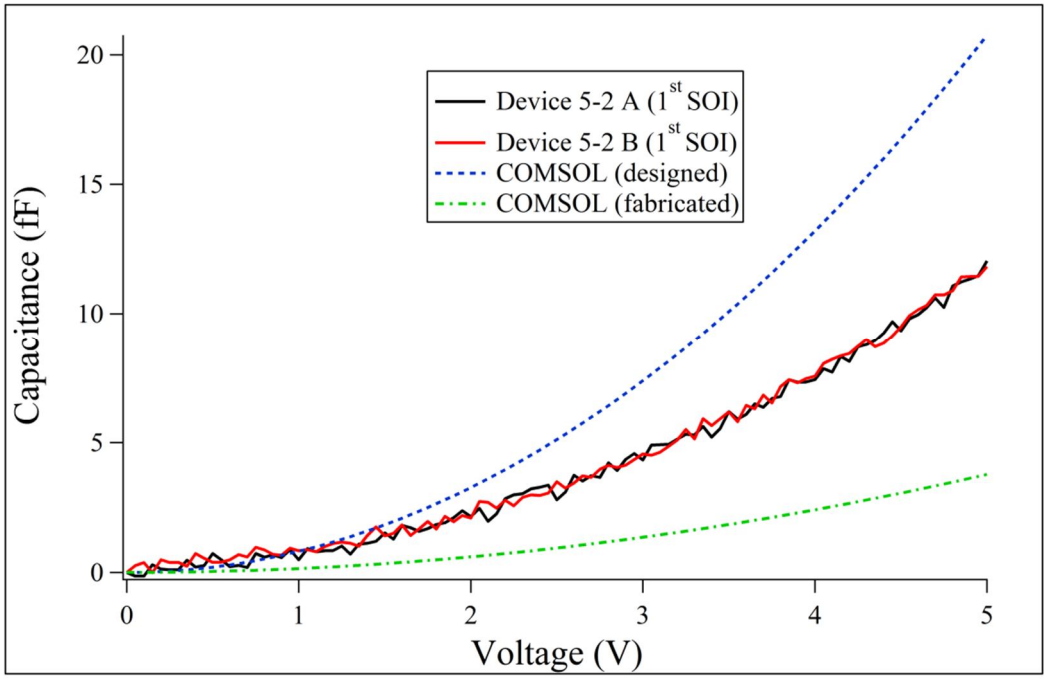

Figure 5.10: Change in capacitance of the force sensor (experimental and simulation)

5.4 Pre-stress Characterization

The designed stress indicator was imaged with SEM to determine the pre-stress after microfabrication. Figure 5.15 shows the deflection of indicator beam. Since the deflection is too small, *i.e.* around 1 µm, pre-stress is assumed to be less than 10 MPa and neglected. The indicator beam was proved to be released as explained in Chapter 4 using a surface profilometer. The beam was successfully moved by the tip of the profilometer.

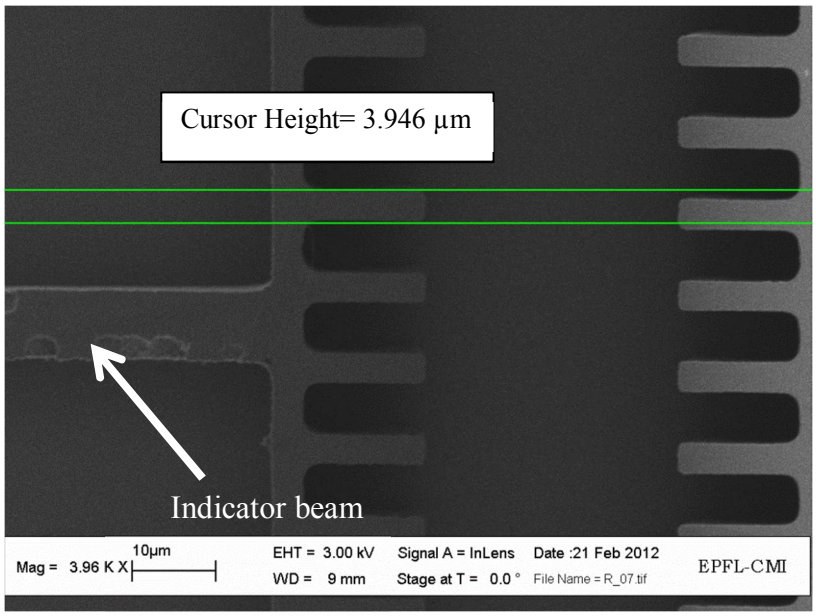

Figure 5.11: Pre-stress indicator after release

Chapter 6

FUTURE WORK AND CONCLUSION

6.1 Overview

Based on the guidance given by this thesis, second generation microfabrication procedures are planned in order to both characterize MEMS part directly by mechanical means and integrate Si NW to the MEMS tensile device. In this chapter, the process flow will be given for the MEMS fabrication. The Si NW-MEMS integration will be the ultimate goal of this work and it requires another process flow for the whole device.

6.2 Process Flow for MEMS Fabrication

The electrical characterization of the designed comb drive actuators and capacitive force/displacement sensors was already carried out as a part of this work. However, the mechanical characterization of them is still required to determine how much force the actuator generates when the voltage is applied and whether the force sensor gives the exact voltage output when a known force is applied. These calibration experiments can be realized by using commercial micro force sensors. These force sensors are also based on capacitance changes which are induced by the movement of fingers attached to a shuttle with a long tip as the probe. The idea of mechanical characterization of MEMS part is to detect directly the force generated by the actuator using these force sensors. On the other hand, for the sensor part, a known force using commercial sensors is applied and the voltage output will be compared with applied force.

A different process flow is needed to have the tip of the shuttle as a protrusion from the base of the chip for both the actuator and the force sensor as shown in Figure 6.1 and 6.2. A possible way for this is backside photolithography and etching of handle Si layer to remove the layer below the tip. A process flow is proposed as given in Figure 6.3 for the cross section AA' shown in Figure 6.1 and 6.2 which includes both the tip of the shuttle and released fingers. Based on this flow, the etched device layer is protected with parylene coating, in step (e), using Comelec-C30-S. The handle layer can be protected, *i.e.* by blue tape, from coating by parylene. Then, backside lithography and etching is done in steps (f)

and (g), respectively. After etching, both the resist mask and parylene is removed, in step (h), by O_2 plasma. The only critical issue here is that backside Si etching must be done using Alcatel 601E, since He backside cooling is needed in Alcatel AMS 200 DSE. The parylene coating on device layer will prevent backside cooling.

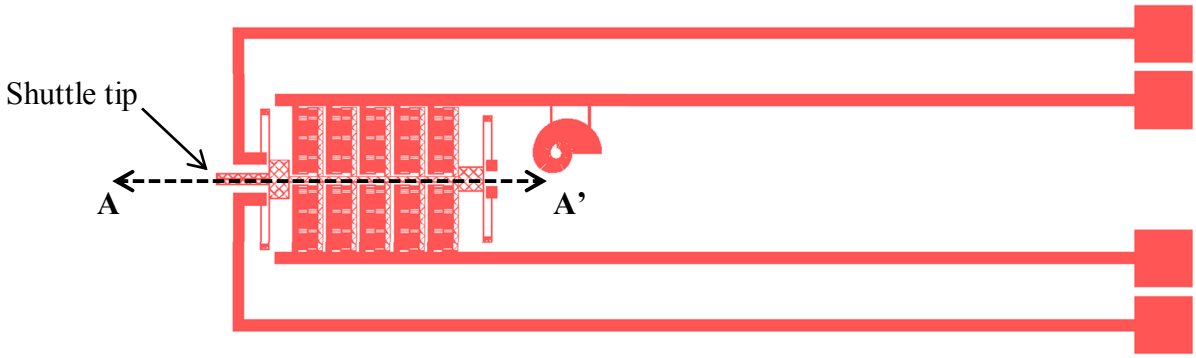

Figure 6.1: The actuator design for mechanical characterization

Figure 6.2: The force sensor design for mechanical characterization

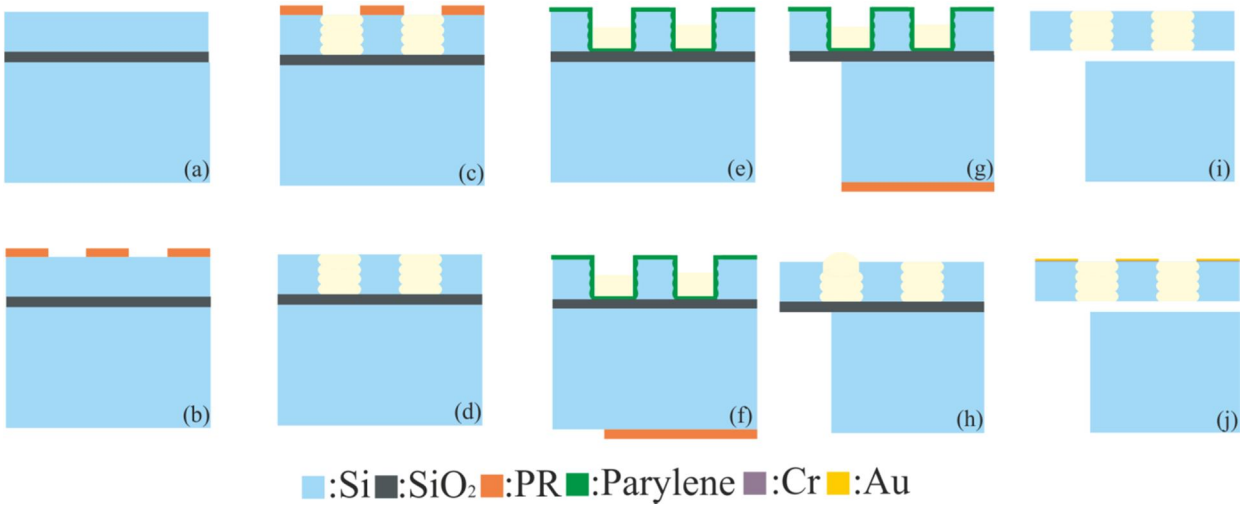

Figure 6.3: Process flow for MEMS devices designed for mechanical characterization (a) Wafer preparation, (b) Photolithography, (c) Bosch process, (d) Resist removal, (e) Parylene coating, (f) Backside photolithography, (g) Backside etching, (h) Parylene and resist removal, (i) HF vapor release, (j) e-beam evaporation

6.3 Evaluation and Contribution

This thesis is the first step to a unique MEMS device. Within this work the design of the microtensile device was completed and realized in a leading microfabrication facility. The electrical characterization of the devices were carried out and compared with the design itself. The comparison showed that the design is reliable and can be used for further integration of the MEMS device to the Si NW. The fabrication process details were characterized and defined properly.On the other hand, the first Si NWs were fabricated without any envelope around it as shown in Figure 6.4.

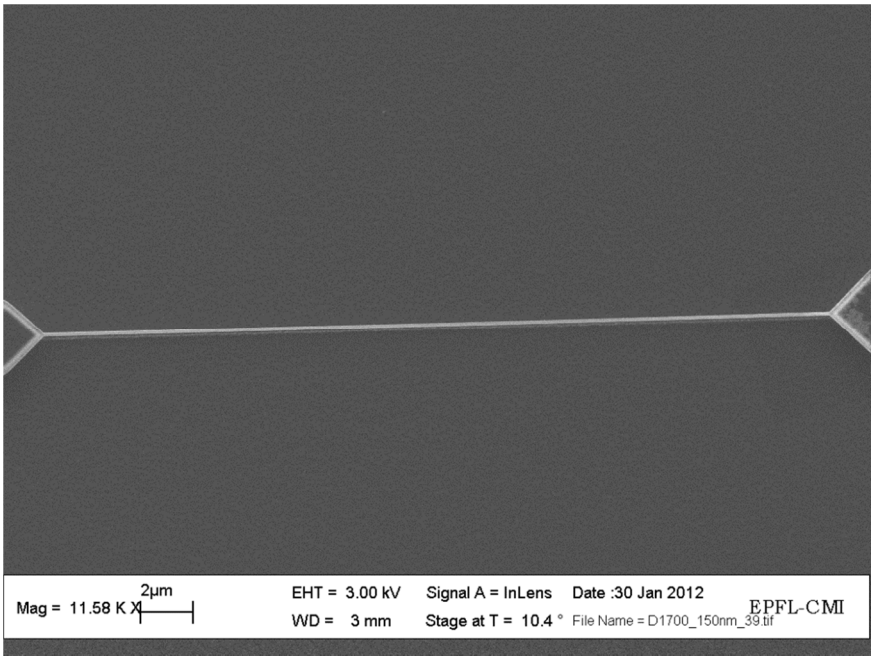

Figure 6.4: Si NW with diameter around 100 nm

The next step of this project will be the micro, *i.e.* MEMS device, and nano, *i.e.* Si NW, integration and to conduct microtensile test on samples with different volumes. This integration can be developed by modifiying the process flow for NW fabrication in such a way the metallization of the MEMS device can be carried out simultaneously. The only critical point is to protect NW from metallization in order to prevent any deviation on mechanical behavior due to metal coating.

Appendix A

MATLAB Code of the Design

```
clc
close all
clear all
%% SYSTEM DESIGN FOR MICROTENSILE TESTING OF Si NANOWIRES

%% VARIABLES RELATED TO THE SAMPLE
%% d: NW diameter (m)
%% sigma_f: fracture stress (Pa)
%% asp_rat: aspect ratio
%% A_s: cross-section area of NW (m^2)
%% E: elastic modulus of Si (Pa)
%% K_s: stiffness of the NW (N/m)
%% F_s: force on NW (N)
%% F_smax: max force on NW (N)
%% deltaU_s: elongation of NW (m)
%% epsi_s: strain of NW
%% l_s: initial length of NW (m)

d=75*1e-9;
asp_rat=400;
sigma_f=12*1e9;
A_s=pi*(d^2)/4;
E=170*1e9;
K_s=A_s*E/(asp_rat*d);
F_smax=sigma_f*A_s;
epsi_s=0.05;
deltaU_s=F_smax/K_s;
l_s=d*asp_rat;

%% VARIABLES RELATED TO THE FORCE SENSOR
%% epsi_0: permittivity of air
%% t_fs: thickness of a sensor finger (m)
%% w_fs: width of a sensor finger (m)
%% l_fs: length of a sensor finger (m)
%% N_data: number of data points
%% x_fsstep: travel distance of force sensor at one step (m)
%% x_fsmax: max travel distance of force sensor (m)
%% d1: small gap between two fingers (m)
%% d2: large gap between two fingers (m)
%% b=d2/d1 ratio
%% N_fs: number of sensor elements (# of sensor fingers/3=fix-mov-fix)
%% deltaC: generated capacitance difference (F)
%% deltaC_min: minimum capacitance difference (F)
%% C_total: total capacitance (F)
%% A_fs: overlapping area of a sensor finger (m^2)
%% K_fs: stiffness of the force sensor (N/m)
%% F_fs: force on force sensor (N)
%% F_fsmax: max force on force sensor (N)
%% V_fs: voltage applied to force sensor (V)
%% V_out: voltage read from force sensor (V)
%% V_outmin: min voltage can be read from analyzer (V)
%% delta: e.s.force/rest.force ratio (parameter for stability)
%% x_fs: travel distance of movable sensor finger (m)
```

```
%% xtilda: x/d1 ratio
%% xtilda_max: x_fsmax/d1
%% nl_d: non-linearity due to displacement(deltaC) (percent)
%% nl_f: non-linearity due to force(V_fs) (percent)
%% nl_dmax: max non-lin. due to disp. (percent)
%% nl_fmax: max non-lin. due to force (percent)
%% S: sensitivity (V_out/epsi_s)

epsi_0=8.854*1e-12;
t_fs=50*1e-6;
w_fs=10*1e-6;
l_fs=780*1e-6;
N_data=2200;
F_fsmax=F_smax;  % Since the force on the NW and the force sensor is the
same.
d1= 4*1e-6;
b=6;
K_fs=55.17;
x_fsmax=F_fsmax/K_fs;
S=0;
V_fs=2;  %Voltage applied to the force sensor to read the differential
capacitance.
V_outmin=1*1e-6; % for KEITHLEY 4200 SCS Semiconductor parameter analyzer
it=1;
N_fs=[0];
A_fs=[0];
nl_dmax=[0];
nl_fmax=[0];

d1val=[0];
d2val=[0];
t_fsval=[0];
w_fsval=[0];
l_fsval=[0];
N_dataval=[0];
K_fsval=[0];
V_fsval=[0];
V_out=[0];
Sval=[0];

for t_fs=45*1e-6:50*1e-6:145*1e-6
    for w_fs=5*1e-6:1e-6:10*1e-6
        for l_fs=200*1e-6:50*1e-6:800*1e-6
            for N_data=2000:100:3000
                for d1=2*1e-6:1*1e-6:10*1e-6
                    for b=5:1:10
                        for K_fs=50:10:200
                            for V_fs=2:1:5

                                d2=b*d1;
                                xtilda_max=x_fsmax/d1;
                                x_fsstep=x_fsmax/N_data;
                                deltaC_min=1*1e-15; %1fF
                                a=2*epsi_0*(t_fs*l_fs)*x_fsstep;    %to
simplify formulas

                                N_fs(it)=ceil(deltaC_min/(1/(d1^2-
x_fsstep^2)-1/(d2^2-x_fsstep^2))/a);    %ceil operator rounds N_fs to the
next larger integer.
                                A_fs(it)=N_fs(it)*(d1+d2+3*w_fs)*l_fs;
```

```
                                x_fs=0:x_fsstep:x_fsmax;
                                deltaC=ceil(deltaC_min./(1./(d1.^2-
x_fsstep^2)-1./(d2.^2-
x_fsstep^2))/a)*2*epsi_0*(t_fs*l_fs)*x_fs.*(1./(d1.^2-x_fs.^2)-1./(d2.^2-
x_fs.^2));

                                %% Force sensor ARDE analysis

                                asp_rat_fs=45;
                                if t_fs/d1>asp_rat_fs
                                    break
                                end

                                %% Force sensor fringing field analysis

                                if xtilda_max>0.5
                                    break
                                end
                                %% Force sensor simplicity analysis

                                if N_fs(it)>55
                                    break
                                end

                                %% Force sensor stability analysis


delta=2*N_fs(it)*epsi_0*(t_fs*l_fs)*V_fs^2/(K_fs*d1^3);

                                xtilda=0:1e-2:1;
                                ind=length(xtilda);
                                f=xtilda.*(1-delta*(1./(b^3*(1-
xtilda.^2/b^2).^2)+(1./(1-xtilda.^2).^2)));

                                peak=max(f);
                                for i=1:ind
                                    if f(i)==peak
                                        peakx=i;
                                    end
                                end

                                if peakx/100<xtilda_max
                                    break
                                end

                                %% Force sensor linearity analysis

                                xtilda=0:1e-2:xtilda_max;

                                nl_d=(xtilda/xtilda_max).*((1./(1-
xtilda.^2)-1./(b^2-xtilda.^2))/(1/(1-xtilda_max^2)-1/(b^2-xtilda_max^2))-
1);
                                nl_f=(xtilda/xtilda_max).*((1./(1-
xtilda.^2)-1./(b^2-xtilda.^2))/(1/(1-xtilda_max^2)-1/(b^2-xtilda_max^2))-
(1-delta*(b./(b^2-xtilda.^2).^2+1./(1^2-xtilda.^2).^2))*1./(1-
delta*((b./b^2-xtilda_max.^2).^2+1./(1^2-xtilda_max.^2)^2)));
```

```
                                    nl_dmax(it)=max(abs(nl_d));
                                    nl_fmax(it)=max(abs(nl_f));

                                    if nl_fmax(it)>0.05
                                        break
                                    end

                                    %% Force sensor finger stability analysis

                                    safety=3;
fingerdisp=safety*3*l_fs^5*epsi_0*V_fs^2*(d2/(d2^2-x_fsmax^2)^2+d1/(d1^2-
x_fsmax^2)^2)*x_fsmax/(E*w_fs*t_fs^2);

                                    if fingerdisp>(d1-x_fsmax)
                                        break
                                    end
                                    %% Output voltage(V_out) analysis

                                    C_total(it)=ceil(deltaC_min./(1./(d1.^2-
x_fsstep^2)-1./(d2.^2-x_fsstep^2))/a)*epsi_0*l_fs*t_fs*(1/d1+1/d2)*2;

                                    V_out(it)=max(deltaC)/C_total(it)*V_fs;

                                    if V_out(it)<V_outmin*N_data
                                        break
                                    end
                                    %% Sensitivity analysis

                                    S=V_out(it)./((x_fsmax*K_fs/K_s)/l_s);

                                    d1val(it)=d1;
                                    d2val(it)=d2;
                                    t_fsval(it)=t_fs;
                                    w_fsval(it)=w_fs;
                                    l_fsval(it)=l_fs;
                                    N_dataval(it)=N_data;
                                    K_fsval(it)=K_fs;
                                    V_fsval(it)=V_fs;
                                    Sval(it)=S;

                                    it=it+1;
                                end
                            end
                        end
                    end
                end
            end
        end
    end
end
FST(d,t_fsval,w_fsval,l_fsval,N_dataval,d1val,d2val,K_fsval,V_fsval,N_fs,
A_fs,nl_fmax,Sval); % The function that tabulates the results
%% VARIABLES RELATED TO THE FORCE SENSOR SPRINGS
%% K_fs: force sensor stiffness (N/m)
%% t_kfs: thickness of sensor spring finger (m)
%% w_kfs: width of sensor spring finger (m)
%% l_kfs: length of sensor finger (m)
%% N_kfs: number of sensor springs
%% K_kfs: sensor spring stiffness (N/m)
```

```
K_fs=55.17;
K_kfsval=[0];
K_kfs=K_fs;
t_kfs=50*1e-6;
w_kfsval=[0];
l_kfs1val=[0];
l_kfs2val=[0];
asprat1fsval=[0];
asprat2fsval=[0];
i=1;
for w_kfs=5*1e-6:1e-6:15*1e-6
    for l_kfs1=10*1e-6:5*1e-6:500*1e-6
        for l_kfs2=20*1e-6:5*1e-6:500*1e-6
            K_kfs=8*E*t_kfs*w_kfs^3/(l_kfs1^3+l_kfs2^3);

            if l_kfs1-l_kfs2<100*1e-6
                break
            end
            if l_kfs1/w_kfs>100 || l_kfs2/w_kfs>100
                break
            end
            if K_kfs>100 || K_kfs<50
                break
            end
            l_kfs1val(i)=l_kfs1;
            l_kfs2val(i)=l_kfs2;
            w_kfsval(i)=w_kfs;
            K_kfsval(i)=K_kfs;
            asprat1fsval(i)=l_kfs1val(i)/w_kfsval(i);
            asprat2fsval(i)=l_kfs2val(i)/w_kfsval(i);
            i=i+1;
        end
    end
end

FSKT(t_kfs,w_kfsval,l_kfs1val,l_kfs2val,K_kfsval,asprat1fsval,asprat2fsva
l); % The function that tabulates the results

%% VARIABLES RELATED TO THE ACTUATOR SPRINGS
%% K_a: actuator stiffness (N/m)
%% t_ka: thickness of actuator spring finger (m)
%% w_ka: width of actuator spring finger (m)
%% l_ka: length of actuator spring finger (m)
%% N_ka: number of actuator springs
%% K_ka: actuator spring stiffness (N/m)
%% K_kay: actuator spring stiffness along y-direction (N/m)
%% K_kaz: actuator spring stiffness along z-direction (N/m)

t_ka=50*1e-6;
w_ka=6*1e-6;
l_ka1=600*1e-6;
l_ka2=600*1e-6;
l_ka3=600*1e-6;
l_ka4=600*1e-6;
l_ka5=600*1e-6;
l_ka6=450*1e-6;
w_kaval=[0];
l_ka1val=[0];
l_ka2val=[0];
l_ka3val=[0];
```

```
l_ka4val=[0];
l_ka5val=[0];
l_ka6val=[0];
K_kaval=[0];
asprat1val=[0];
asprat2val=[0];
i=1;


for w_ka=5*1e-6:1e-6:15*1e-6
    for l_ka1=200*1e-6:50*1e-6:700*1e-6
        for l_ka2=200*1e-6:50*1e-6:700*1e-6
            for l_ka3=200*1e-6:50*1e-6:700*1e-6
                for l_ka4=200*1e-6:50*1e-6:700*1e-6
                    for l_ka5=200*1e-6:50*1e-6:700*1e-6
                        for l_ka6=200*1e-6:50*1e-6:700*1e-6

K_ka=4*E*t_ka*w_ka^3/(l_ka1^3+l_ka2^3+l_ka3^3+l_ka4^3+l_ka5^3+l_ka6^3);

                            if l_ka1-l_ka3<30*1e-6 || l_ka2-l_ka3<30*1e-6
                                break
                            end

                            if l_ka1/w_ka>100 || l_ka2/w_ka>100 ||
l_ka3/w_ka>100 || l_ka4/w_ka>100 || l_ka5/w_ka>100 || l_ka6/w_ka>100
                                break
                            end

                            if K_ka>10
                                break
                            end
                            l_ka1val(i)=l_ka1;
                            l_ka2val(i)=l_ka2;
                            l_ka3val(i)=l_ka3;
                            l_ka4val(i)=l_ka4;
                            l_ka5val(i)=l_ka5;
                            l_ka6val(i)=l_ka6;
                            w_kaval(i)=w_ka;
                            K_kaval(i)=K_ka;
                            asprat1val(i)=l_ka1val(i)/w_kaval(i);
                            asprat2val(i)=l_ka2val(i)/w_kaval(i);
                            asprat3val(i)=l_ka3val(i)/w_kaval(i);
                            asprat4val(i)=l_ka4val(i)/w_kaval(i);
                            asprat5val(i)=l_ka5val(i)/w_kaval(i);
                            asprat6val(i)=l_ka6val(i)/w_kaval(i);
                            i=i+1;
                        end
                    end
                end
            end
        end
    end
end


K_kaz=4*E*w_ka*t_ka^3/(l_ka1^3+l_ka2^3+l_ka3^3+l_ka4^3+l_ka5^3+l_ka6^3);
K_ay=4*E*w_ka*t_ka/(l_ka1+l_ka2+l_ka3+l_ka4+l_ka5+l_ka6);
AST(t_ka,w_kaval,l_ka1val,l_ka2val,l_ka3val,l_ka4val,l_ka5val,l_ka6val,K_
kaval); % The function that tabulates the results
K_a=6.27;
```

```
%% VARIABLES RELATED TO THE ACTUATOR
%% epsi_0: air permittivity
%% t_a: thickness of actuator finger (m)
%% w_a: width of actuator finger (m)
%% h: zero voltage overlap of actuator finger (m)
%% gx: gap between actuator fingers in x-direction (tip of finger) (m)
%% gy: gap between actuator fingers in y-direction (actuation gap) (m)
%% gz: gap between testing device and handle layer (m)
%% V_a: applied voltage (V)
%% V_amax: max applied voltage (V)
%% x_a: displacement of actuator finger (m)
%% x_amax: max displacement of actuator finger (m)
%% F_e: generated electrostatic force (N)
%% F_emax: max generated electrostatic force (N)
%% F_a: force at the tip of the actuator (transferred to actuator
springs) (N)
%% N_a: number of actuator fingers
%% A_a: area of the actuator
%% K_a: actuator stiffness (N/m)
%% V_pix: pull-in voltage for front pull-in (V)
%% V_piy: pull-in voltage for side pull-in (V)
%% V_piz: levitation pull-in voltage (V)
%% K_eq: equivalent stiffness of whole system (N/m)
%% x_pi: pull-in distance (m)

t_a=50*1e-6;
w_a=5*1e-6;
h=6*1e-6;
gx=96*1e-6;
gy=4*1e-6;
gz=2*1e-6;
V_amax=40;
N_a=[0];
A_a=[0];
fin_sol=[0];
ir=1;
t_aval=[0];
w_aval=[0];
gxval=[0];
gyval=[0];
hval=[0];
V_pix=[0];

for t_a=45*1e-6:50*1e-6:145*1e-6
    for w_a=5*1e-6:1e-6:15*1e-6
        for gx=76*1e-6:2*1e-6:100*1e-6
            for gy=4*1e-6:1*1e-6:20*1e-6
                for h=6*1e-6:1e-6:20*1e-6

                    x_amax=deltaU_s+x_fsmax;

                    if h+x_amax>gx
                        break
                    end
                    while gx<x_amax
                        gx=gx+1e-6;
                    end

                    K_eq=(K_fs*K_s+K_a*K_fs+K_a*K_fs)/(K_fs+K_s);
```

```
                    F_emax=F_smax/((K_s*K_fs)/(K_s+K_fs))*K_eq;
                    N_a(ir)=ceil(F_emax/(epsi_0*t_a*(w_a/(gx-
x_amax)^2+1/gy)*V_amax^2));
                    A_a(ir)=(2*gx-h)*(gy+2*w_a)*N_a(ir);


                    %% Actuator ARDE analysis

                    asp_rat_a=45;

                    if asp_rat_a<t_a/gy
                        break
                    end

                    %% Actuator simplicity analysis

                    if N_a(ir)>1000
                        break
                    end

                    %% Actuator stability analysis----Front pull-in

                    x_pi1=
1/3*(27*w_a*gy+3*(3*w_a^3*gy^3+81*w_a^2*gy^2)^(1/2))^(1/3)-
w_a*gy/(27*w_a*gy+3*(3*w_a^3*gy^3+81*w_a^2*gy^2)^(1/2))^(1/3)+gx;
                    x_pi2=  -
1/6*(27*w_a*gy+3*(3*w_a^3*gy^3+81*w_a^2*gy^2)^(1/2))^(1/3)+1/2*w_a*gy/(27
*w_a*gy+3*(3*w_a^3*gy^3+81*w_a^2*gy^2)^(1/2))^(1/3)+gx+1/2*i*3^(1/2)*(1/3
*(27*w_a*gy+3*(3*w_a^3*gy^3+81*w_a^2*gy^2)^(1/2))^(1/3)+w_a*gy/(27*w_a*gy
+3*(3*w_a^3*gy^3+81*w_a^2*gy^2)^(1/2))^(1/3));
                    x_pi3=  -
1/6*(27*w_a*gy+3*(3*w_a^3*gy^3+81*w_a^2*gy^2)^(1/2))^(1/3)+1/2*w_a*gy/(27
*w_a*gy+3*(3*w_a^3*gy^3+81*w_a^2*gy^2)^(1/2))^(1/3)+gx-
1/2*i*3^(1/2)*(1/3*(27*w_a*gy+3*(3*w_a^3*gy^3+81*w_a^2*gy^2)^(1/2))^(1/3)
+w_a*gy/(27*w_a*gy+3*(3*w_a^3*gy^3+81*w_a^2*gy^2)^(1/2))^(1/3));

                    % solutions are for x_pi (pull-in distance)

                    Soln=[x_pi1,x_pi2,x_pi3];
                    Soln=sort(Soln);
                    if min(Soln)>=0
                        fin_sol(ir)=min(Soln);
                    end

                    if min(Soln)<0
                        if Soln(1)<0
                            fin_sol(ir)=Soln(2);
                        elseif Soln(2)<0
                            fin_sol(ir)=Soln(3);
                        end
                    end

                    V_pix(ir)=(fin_sol(ir)*K_eq/(epsi_0*t_a*(w_a/(gx-
fin_sol(ir))^2+1/gy)*N_a(ir))).^0.5;

                    if V_pix(ir)-V_amax<1
                        break
                    end
```

```
                    if x_amax>fin_sol(ir)
                        frontpullin=fin_sol(ir);
                        break
                    end

                    %% Actuator stability analysis----Side pull-in

                    safety=4;

V_piy=safety*(K_ay*gy^3/(2*epsi_0*t_ka*(x_amax+h)))^.5;

                    if V_amax>V_piy
                        sidepullin=V_piy;
                        break
                    end

                    %% Actuator linearity analysis

                    if (h+x_amax)/gy*(gx-x_amax)/w_a<40
                        break
                    end

                    %% Actuator levitation (out-of-plane motion) analysis

                    V_piz=(8*K_kaz*gz^3/(27*epsi_0*A_a(ir)/2));   %Can be
written on the table.
                    gxval(ir)=gx;
                    gyval(ir)=gy;
                    hval(ir)=h;
                    w_aval(ir)=w_a;
                    t_aval(ir)=t_a;

                    ir=ir+1;
                end
            end
        end
    end
end

ACT(d,t_aval,w_aval,hval,gxval,gyval,K_a,V_amax,N_a,A_a); % The function
that tabulates the results

%% END OF THE CODE %%
```

MATLAB Code of Pre-Stress Indicator Design

```
close all
clear all
clc

%%% Ltb    Length of test beam
%%% wtb    width of test beam
%%% Lsb    Length of slope beam
%%% wsb    width of slope beam
%%% Lib    Length of indicator beam
%%% wib    width of indicator beam
%%% del_tb deflection of test beam
%%% E      Modulus of elasticity
%%% str    Residual stress in test beam
%%% AR     Aspect Ratio

%%% Limitations:
%%% - Residual Strain in the Slope Beam
%%% - Stiffness of the Slope Beam
%%% - Buckling Effect in the Test Beam
%%% - Buckling Effect in the Slope Beam

%%% if (wsb<h)
%%%    eps_max_com_L4=4*pi^2*h^2*wsb*Ltb^2/(3*Lsb^2*wtb^3);
%%% else
%%%    eps_max_com_L4=4*pi^2*wsb^3*Ltb^2/(3*Lsb^2*wtb^3);
%%% end

%%% eps_max_com_L3=pi^2*t^2*wtb*Lsb^3/(3*wsb^3*Ltb^3);
t=50e-6;

AR=100;
E=170e9;
str=20e6;
i=1;

format long

for Ltb=100e-6:100e-6:3500e-6
    for wtb=5e-6:5e-6:100e-6
        for Lsb=t*10:10e-6:1000e-6
            for wsb=1e-6:1e-6:10e-6
                for Lib=100e-6:100e-6:2000e-6
                    for wib=1e-6:1e-6:10e-6
                        d=wib/Lsb;
                        ratio=Lib/wib;
                        if
(Ltb/wtb<=100)&&(Lib/wib<=300)&&(Lsb/wsb<=100)&&(d<0.1)
                            I=(wtb^3*t)/12;
                            M_ratio= eps*wtb^3*Lsb^3/(4*Ltb^3*wsb^3);
                            k_ratio= Ltb*wsb^3/(Lsb^3*wtb);

                            eps_comp_L3=pi^2*I/(0.5^2*Ltb^2*t*wtb);
                            I_3=(wsb^3*t)/12;
                            eps_comp_L4=pi^2*I_3/(0.699^2*Lsb^2*t*wsb);
                            def_tb=str*Ltb/E;
```

```
                                d=wib/Lsb;
                                C=(1-d^2)/(1-d^3);

eps_max_com_L3=pi^2*t^2*wtb*Lsb^3/(3*wsb^3*Ltb^3);

eps_max_com_L4=4*pi^2*t^2*wsb*Ltb^2/(3*Lsb^2*wtb^3);

                                theta(i)=3*def_tb*C/(2*Lsb);
                                uzama(i)=Lib*sin(theta(i));
                                if
(M_ratio<0.05)&&(k_ratio<0.05)&&(eps_comp_L3<eps_max_com_L3)&&(eps_comp_L
4<eps_max_com_L4)
                                    if(uzama(i)>2.4e-6)&&(uzama(i)<2.6e-6)
                                        LTB(i)=Ltb;
                                        WTB(i)=wtb;
                                        LSB(i)=Lsb;
                                        WSB(i)=wsb;
                                        LIB(i)=Lib;
                                        WIB(i)=wib;
                                        a(i)=d;
                                        RATIO(i)=Lib/wib;

                                        i=i+1;
                                    end
                                end
                            end
                        end
                    end
                end
            end
        end
    end
end
para=[LTB',WTB',LSB',WSB',LIB',WIB',uzama(1:end-1)',a',RATIO']


plot(1:1:length(uzama),uzama,'*')
```

Appendix B

Photololithography Masks

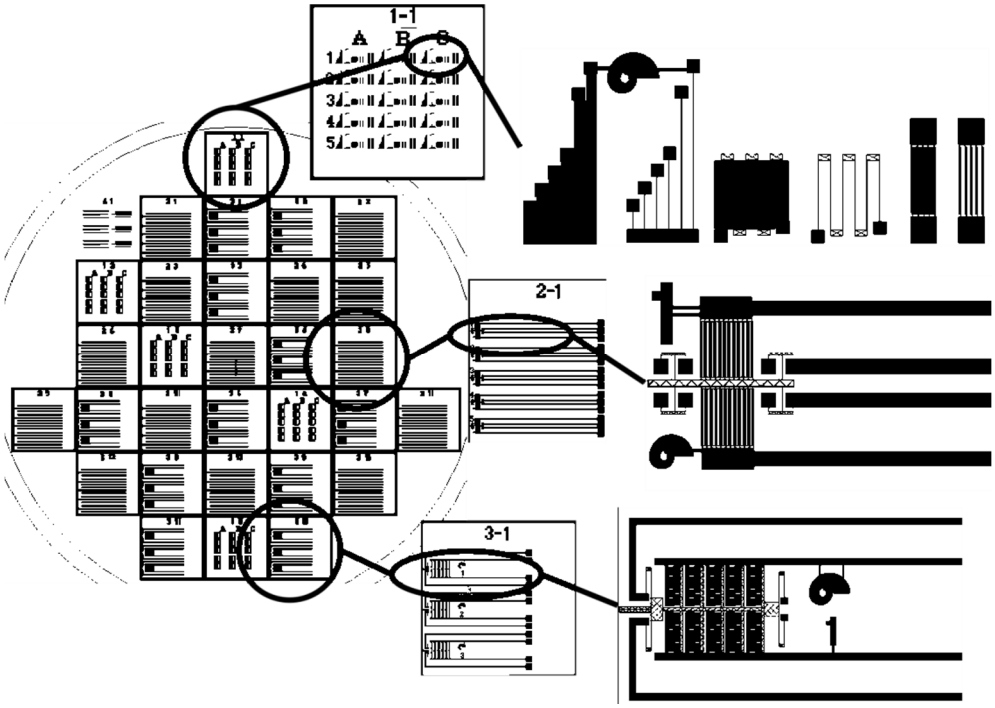

Figure B.1: Photolithography mask used for determination of microfabrication limits (Chips and building blocks of chips are shown.)

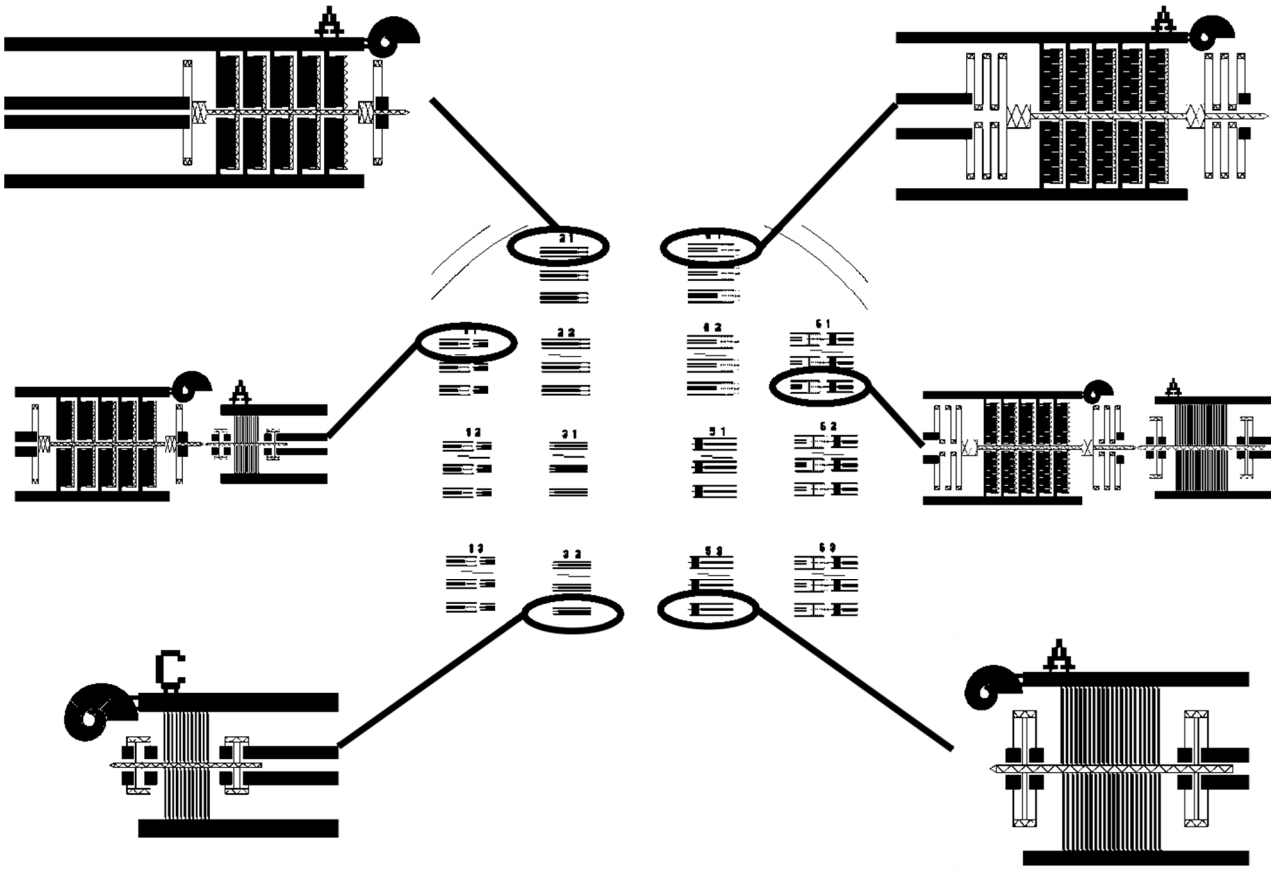

Figure B.2: Photolithography mask designed for calibration devices

Appendix C

Runcards for Microfabrication

Step N°	Description	Equipment	Program / Parameters	Target	Actual	Remarks
0	**WAFER PREPARATION**					
0,01	Stock out					
0,02	Check					
1	**PHOTOLITHOGRAPHY**					
1,01	HMDS	Z1/YES3	Prog. 0			
1,02	AZ 92xx coating	Z1/Rite Track	C_AZ92xx_2um	2 µm		
1,03	PR bake	Z1/Rite Track	C_AZ92xx_2um	2 µm		
1,04	PR expose	Z1/MA150	Manual Align, HC, 10.0 mW/cm^2			
1,05	PR develope	Z1/Rite Track	Dev_AZ_92xx_2um			
1,06	PR postbake	Z1/Rite Track	Temperature	114C		
1,07	Inspection	Z6/uScope	Resolution and alignment			
1,08	Descum	Z5/Tepla	Descum O_2, 5min			
2	**SCALLOPED TRENCH FORMATION**					
2,01	Chamber Priming	Z2/AMS200	SOI_accurate++++	5'		
2,02	Scalloped Trench Formation	Z2/AMS200	SOI_accurate++++	25', 50 µm		
2,03	İnspection	Z2/uScope				
3	**CLEANING**					
3,01	Remover 1165	Z2/WB_PR_Strip	Bath 1 : main remover	5min, 70°C		
3,02	Remover 1165	Z2/WB_PR_Strip	Bain 2 : clean remover	5min, 70°C		
3,03	Fast fill rinse	Z2/WB_PR_Strip	DI Rinse			
3,04	Trickle tank	Z2/WB_PR_Strip	DI Rinse	5min, 70°C		
3,05	Spin Rinser Dryer	Z2/Semitool SRD	prog 1			
3,06	Plasma O2 clean	Z2/Oxford	O_2 , 20 min			
3,07	Spin Rinser Dryer	Z2/Semitool SRD	prog 1			
3,08	Inspection	Z6/uScope				
4	**WAFER SCRIBING**					
5	**HF VAPOR RELEASE**					
5,01	HF vapor etch	Z5/Idonus HF VPE 100	SiO2	2h, 6 µm		
6	**e-BEAM EVAPORATION**					
6,01	Cr evaporation	Z4/LAB600H	Cr-Au	10 nm		
6,02	Au evaporation	Z4/LAB600H	Cr-Au	300 nm		

Table C.1: Runcard for process executed on 1st SOI wafer

Step N°	Description	Equipment	Program / Parameters	Target	Actual	Remarks
0	**WAFER PREPARATION**					
0,01	Stock out					
0,02	Check					
1	**PHOTOLITHOGRAPHY**					
1,01	HMDS	Z1/YES3	Prog. 0			
1,02	AZ 92xx coating	Z1/Rite Track	C_AZ92xx_2um	2 µm		
1,03	PR bake	Z1/Rite Track	C_AZ92xx_2um	2 µm		
1,04	PR expose	Z1/MA150	Manual Align, HC, 10.0 mW/cm^2			
1,05	PR develope	Z1/Rite Track	Dev_AZ_92xx_2um			
1,06	PR postbake	Z1/Rite Track	Temperature	114C		
1,07	Inspection	Z6/uScope	Resolution and alignment			
1,08	Descum	Z5/Tepla	Descum O_2, 5min			
2	**SCALLOPED TRENCH FORMATION**					
2,01	Chamber Priming	Z2/AMS200	SOI_accurate++++	5'		
2,02	Scalloped Trench Formation	Z2/AMS200	SOI_accurate++++	20', 50 µm		
2,03	inspection	Z2/uScope				
3	**CLEANING**					
3,01	Remover 1165	Z2/WB_PR_Strip	Bath 1 : main remover	5min, 70°C		
3,02	Remover 1165	Z2/WB_PR_Strip	Bain 2 : clean remover	5min, 70°C		
3,03	Fast fill rinse	Z2/WB_PR_Strip	DI Rinse			
3,04	Trickle tank	Z2/WB_PR_Strip	DI Rinse	5min, 70°C		
3,05	Spin Rinser Dryer	Z2/Semitool SRD	prog 1			
3,06	Plasma O2 clean	Z2/Oxford	O_2 , 20 min			
3,07	Spin Rinser Dryer	Z2/Semitool SRD	prog 1			
3,08	Inspection	Z6/uScope				
4	**WAFER SCRIBING**					
5	**HF VAPOR RELEASE**					
5,01	HF vapor etch	Z5/Idonus HF VPE 100	SiO2	2h, 6 µm		
6	**e-BEAM EVAPORATION**					
6,01	Cr evaporation	Z4/LAB600H	Cr-Au	10 nm		
6,02	Au evaporation	Z4/LAB600H	Cr-Au	300 nm		

Table C.2: Runcard for process executed on 2nd SOI wafer

Appendix D

Recipe Details

SOI_accu++++:

SF_6 Flow	300 sccm
C_4F_8 Flow	150 sccm
SF_6 Time	8 sec
C_4F_8 Time	2 sec

Z_SOI_accu:

SF_6 Flow	200 sccm
C_4F_8 Flow	150 sccm
SF_6 Time	2.5 sec
C_4F_8 Time	1 sec

Appendix E

AC Characterization of the Force Sensor

For the dynamic characterization of the force sensor, HP 4195A network analyzer was used. The connection scheme is shown in Figure E.1. Since there were no results by connecting the devices directly to the analyzer, an amplifier circuit [41] was constructed as shown in Figure E.2. However, it was not enough to increase the AC signal coming from the force sensor, hence the analyses comed to end without any reliable data.

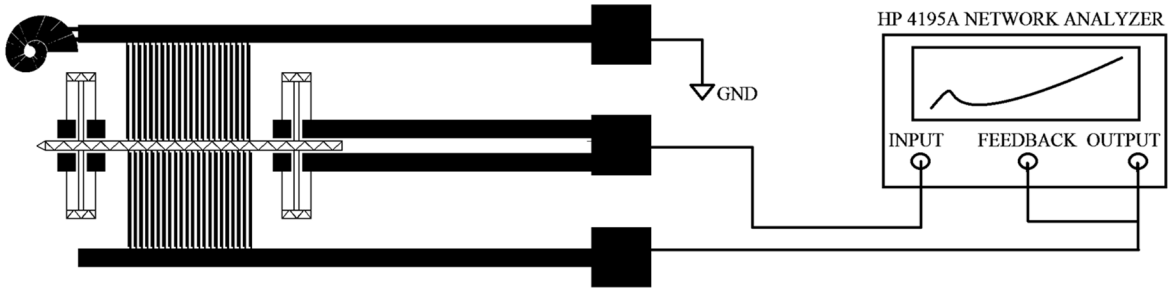

Figure E.1: Dynamic characterization scheme of the force sensor

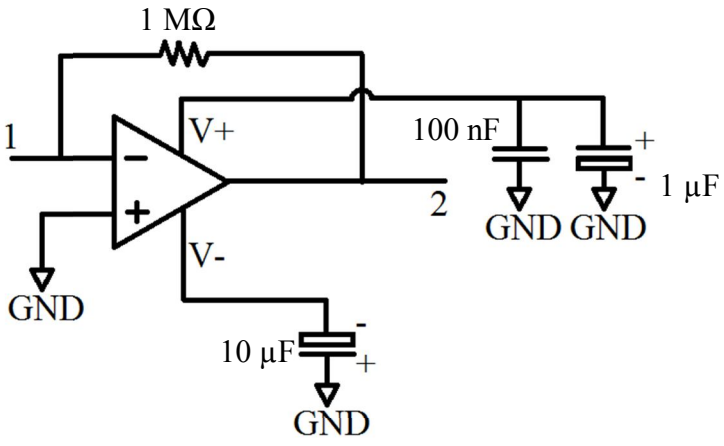

Figure E.2: Signal amplifier circuit

BIBLIOGRAPHY

[1] Y. Zhu, F. Xu, Q.Q. Qin, W.Y. Fung, W. Lu, Nano Lett., 9 (2009) 3934-3939.

[2] T. Namazu, Y. Isono, T. Tanaka, Microelectromechanical Systems, Journal of, 9 (2000) 450-459.

[3] J.d. Boor, D.S. Kim, X. Ao, D. Hagen, A. Cojocaru, H. Föll, V. Schmidt, EPL (Europhysics Letters), 96 (2011) 16001.

[4] J. Jie, W. Zhang, K. Peng, G. Yuan, C.S. Lee, S.-T. Lee, Adv. Funct. Mater., 18 (2008) 3251-3257.

[5] R. He, P. Yang, Nat Nano, 1 (2006) 42-46.

[6] J.S. Milne, A.C.H. Rowe, S. Arscott, C. Renner, Phys. Rev. Lett., 105 (2010) 4.

[7] Y.J. Kim, K. Son, I.C. Choi, I.S. Choi, W.I. Park, J.I. Jang, Adv. Funct. Mater., 21 (2011) 279-286.

[8] S. Hoffmann, I. Utke, B. Moser, J. Michler, S.H. Christiansen, V. Schmidt, S. Senz, P. Werner, U. Gosele, C. Ballif, Nano Letters, 6 (2006) 622-625.

[9] H. Ni, X.D. Li, H.S. Gao, Applied Physics Letters, 88 (2006) 3.

[10] J. Song, X. Wang, E. Riedo, Z.L. Wang, Nano Lett., 5 (2005) 1954-1958.

[11] H. Ni, X.D. Li, Nanotechnology, 17 (2006) 3591-3597.

[12] S. Hoffmann, F. Ostlund, J. Michler, H.J. Fan, M. Zacharias, S.H. Christiansen, C. Ballif, Nanotechnology, 18 (2007) 5.

[13] M.P. Manoharan, A.V. Desai, G. Neely, M.A. Haque, J. Nanomaterials, 2008 (2008) 1-7.

[14] Q. Xiong, N. Duarte, S. Tadigadapa, P.C. Eklund, Nano Lett., 6 (2006) 1904-1909.

[15] H. Ni, X.D. Li, G.S. Cheng, R. Klie, J. Mater. Res., 21 (2006) 2882-2887.

[16] C.X. Zou, G.Y. Jing, D.P. Yu, Y.H. Xue, H.L. Duan, Phys. Lett. A, 373 (2009) 2065-2070.

[17] E. Celik, I. Guven, E. Madenci, Nanotechnology, 22 (2011) 9.

[18] G.C. Johnson, P.T. Jones, R.T. Howe, in: Conference on Micromachining and Microfabrication Process Technology V, Spie-Int Soc Optical Engineering, Santa Clara, Ca, 1999, pp. 94-101.

[19] D. Zhang, in, Ecole Polytechnique Federale De Lausanne, 2010.

[20] D.J. Bell, T.J. Lu, N.A. Fleck, S.M. Spearing, J. Micromech. Microeng., 15 (2005) S153-S164.

[21] D.F. Zhang, J.M. Breguet, R. Clavel, V. Sivakov, S. Christiansen, J. Michler, J. Microelectromech. Syst., 19 (2010) 663-674.

[22] Q.H. Jin, Y.L. Wang, T. Li, X.X. Li, F.F. Xu, Sci. China Ser. E-Technol. Sci., 51 (2008) 1491-1496.

[23] Q.H. Jin, T. Li, Y.L. Wang, X.X. Li, P. Zhou, F.F. Xu, in: IEEE Sensors, 2008.

[24] Y. Zhu, A. Corigliano, H.D. Espinosa, J. Micromech. Microeng., 16 (2006) 242-253.

[25] H.D. Espinosa, Y. Zhu, N. Moldovan, J. Microelectromech. Syst., 16 (2007) 1219-1231.

[26] D.F. Zhang, J.M. Breguet, R. Clavel, L. Philippe, I. Utke, J. Michler, Nanotechnology, 20 (2009) 7.

[27] M. Naraghi, T. Ozkan, I. Chasiotis, S.S. Hazra, M.P. de Boer, J. Micromech. Microeng., 20 (2010) 9.

[28] M. Kiuchi, S. Matsui, Y. Isono, J. Microelectromech. Syst., 16 (2007) 191-201.

[29] B. Pant, B.L. Allen, T. Zhu, K. Gall, O.N. Pierron, Applied Physics Letters, 98 (2011) 3.

[30] J.J. Brown, A.I. Baca, K.A. Bertness, D.A. Dikin, R.S. Ruoff, V.M. Bright, Sens. Actuator A-Phys., 166 (2011) 177-186.

[31] Y. Sun, S.N. Fry, D.P. Potasek, D.J. Bell, B.J. Nelson, J. Microelectromech. Syst., 14 (2005) 4-11.

[32] F. Ericson, S. Greek, J. Soderkvist, J.A. Schweitz, J. Micromech. Microeng., 7 (1997) 30-36.

[33] C.J. Li, Sens. Actuator A-Phys., 155 (2009) 181-187.

[34] C.W. Baek, Y.K. Kim, Y. Ahn, Y.H. Kim, Sens. Actuator A-Phys., 117 (2005) 17-27.

[35] L.C. Jaecklin V. P., Rooij N. F., Moret J. M., J. Micromech. Microeng., 2 (1992) 250-255.

[36] E.F. Arkan, in, Koç University, 2011.

[37] W.C. Tang, M.G. Lim, R.T. Howe, Microelectromechanical Systems, Journal of, 1 (1992) 170-178.

[38] S.W. Chyuan, J. Electrost., 66 (2008) 361-365.

[39] D.F. Zhang, W. Drissen, J.M. Breguet, R. Clavel, J. Michler, J. Micromech. Microeng., 19 (2009) 10.

[40] F. Laermer, A. Schilp, in, Robert Bosch GmbH, US Patent 6,531,068, 2003.

[41] C. Yamahata, D. Collard, B. Legrand, T. Takekawa, M. Kunternura, G. Hashiguchi, H. Fujita, J. Microelectromech. Syst., 17 (2008) 623-631.

VITA

BERKAY GUMUS was born in Ankara, Turkey on May 4, 1987. He received his B.Sc. degree in Metallurgical and Materials Engineering from Middle East Technical University, Ankara in 2010. Since then, he has enrolled in the M.Sc program in Mechanical Engineering at Koc University, Istanbul with full scholarship, as both a teaching and research assistant. His most recent thesis, “A MEMS-based Microtensile Testing Method for Si Nanowires” acts as a complement to his works on MEMS design and fabrication. Upon completion of his Masters Degree, Berkay plans to study further, with a view to achieving a PhD.